

# **Silver nanowire transparent electrodes for device applications**

**by**

**Hadi Hosseinzadeh Khaligh**

**A thesis**

**presented to the University of Waterloo**

**in fulfillment of the**

**thesis requirement for the degree of**

**Doctor of Philosophy**

**in**

**Electrical and Computer Engineering- Nanotechnology**

**Waterloo, Ontario, Canada, 2016**

**© Hadi Hosseinzadeh Khaligh 2016**

I hereby declare that I am the sole author of this thesis. This is a true copy of the thesis, including any required final revisions, as accepted by my examiners. I understand that my thesis may be made electronically available to the public.

## **Abstract**

Random networks of silver nanowires are a promising option to replace conventional transparent conductive oxides, such as indium tin oxide (ITO), which are expensive, brittle, and require high temperatures and vacuum during deposition. In this work, silver nanowire transparent electrodes are fabricated with similar optoelectronic properties as ITO, while having a more convenient deposition process and being both cheaper and more mechanically flexible. Alongside these benefits, however, are some technical challenges that need to be addressed before nanowire electrodes can be widely used in commercial electronic devices. Firstly, the high surface roughness of the nanowire electrodes can cause issues such shorting when they are integrated into thin-film devices. A simple hot-rolling method was studied to embed the nanowires into the surface of plastic substrates, which reduces both the surface roughness and nanowire adhesion. A second issue with nanowire electrodes is the Joule heating that occurs when they conduct current for long periods of time, as is the case when used in solar cells and light emitting diodes. It is shown that the current density in the nanowires is both much higher and non-uniform than in a continuous film such as ITO. This leads to localized temperatures of 250 °C or more when conducting current levels encountered in organic solar cells and OLEDs. These temperatures accelerate electrode breakdown. A passivation layer of reduced graphene oxide is deposited on the nanowire films to slow their degradation. However, Joule heating still occurs and the electrodes fail due to melting of the plastic substrate. Recommendations for managing these adverse effects are proposed.

To expand the application of silver nanowire transparent electrodes, they are integrated into polymer dispersed liquid crystal (PDLC) smart windows for the first time. Not only are the materials and fabrication costs of the nanowire electrodes less than ITO, but the resulting smart

windows exhibit superior electro-optical characteristics. In another application, silver nanowires in conjunction with Al-doped ZnO (AZO) are developed as a conformal and transparent electrode to improve the efficiency of 3D solar cells.

Lastly, a simple method of growing AgCl nanocubes directly on silver nanowires is introduced, which can have applications in surface enhanced Raman spectroscopy (SERS) and photocatalytic reactions.

## **Acknowledgements**

First and foremost, I would like to thank my adviser, Prof. Irene Goldthorpe for her guidance, excellent scientific advices and support throughout my PhD study. I would like to thank Profs Michael Pope, William Wong, Mona Tréguer-Delapierre, and Laurent Servant and their research groups for all of their contribution to this thesis.

I am thankful to all of my colleagues, Jianjin Dong, Nupur Maheshwari, Jonathan Atkinson, Alexandra Madeir, Geoffrey Deignan, Mojtaba Moodi, and Min Zhang for their help, valuable thoughts, and discussions.

I specially thank all of my family members, particularly my wife, Golnaz Bohlouli-Zanjani, for their continuous support and patience.

## **Dedication**

This thesis is dedicated to my parents and my wife Golnaz Bohlouli-Zanjani.

# Table of Contents

|                                                    |            |
|----------------------------------------------------|------------|
| <b>Author's Declaration .....</b>                  | <b>ii</b>  |
| <b>Abstract.....</b>                               | <b>iii</b> |
| <b>Acknowledgements.....</b>                       | <b>v</b>   |
| <b>Dedication.....</b>                             | <b>vi</b>  |
| <b>Table of Contents .....</b>                     | <b>vii</b> |
| <b>List of Figures.....</b>                        | <b>xi</b>  |
| <b>Chapter 1 Introduction.....</b>                 | <b>1</b>   |
| 1.1 Transparent conductive electrodes .....        | 1          |
| 1.2 Alternative materials .....                    | 3          |
| 1.2.1 Carbon nanotubes.....                        | 3          |
| 1.2.2 Graphene .....                               | 4          |
| 1.2.3 Conductive polymers .....                    | 4          |
| 1.2.4 Metal nanowire electrodes .....              | 5          |
| 1.3 Synthesis of silver nanowires.....             | 7          |
| 1.4 Characteristics of transparent electrodes..... | 8          |
| 1.4.1 Transmittance.....                           | 8          |
| 1.4.2 Sheet resistance .....                       | 10         |
| 1.4.3 Roughness parameters .....                   | 13         |
| 1.5 Silver nanowire electrode applications .....   | 14         |

|                                                                               |           |
|-------------------------------------------------------------------------------|-----------|
| 1.6 Silver nanowire electrode challenges .....                                | 16        |
| 1.6.1 Surface roughness and weak adhesion.....                                | 16        |
| 1.6.2 Instability of silver nanowire electrodes .....                         | 17        |
| 1.7 Outline of this thesis.....                                               | 19        |
| <b>Chapter 2 Fabrication of nanowire electrodes.....</b>                      | <b>20</b> |
| 2.1 Silver nanowire electrode fabrication .....                               | 20        |
| 2.2 Characterizing electrodes .....                                           | 22        |
| 2.2.1 Sheet resistance and transmittance in the visible range .....           | 22        |
| 2.2.2 Transmittance in the infrared range .....                               | 23        |
| 2.3 Cost of nanowire electrodes .....                                         | 24        |
| 2.4 Data comparison.....                                                      | 26        |
| <b>Chapter 3 Minimizing surface roughness of the electrodes .....</b>         | <b>29</b> |
| 3.1 Introduction .....                                                        | 29        |
| 3.2 Experimental .....                                                        | 32        |
| 3.3 Minimizing surface roughness .....                                        | 33        |
| 3.3.1 Rolling process.....                                                    | 33        |
| 3.3.2 Rolling temperature .....                                               | 35        |
| 3.3.3 Hot rolling vs annealing results .....                                  | 36        |
| 3.4 Conclusion.....                                                           | 41        |
| <b>Chapter 4 The Joule heating problem in silver nanowire electrodes.....</b> | <b>42</b> |

|                                                                               |           |
|-------------------------------------------------------------------------------|-----------|
| 4.1 Introduction .....                                                        | 43        |
| 4.2 Experimental .....                                                        | 46        |
| 4.2.1 Nanowire electrode fabrication.....                                     | 46        |
| 4.2.2 Determining current flow value .....                                    | 46        |
| 4.2.3 Reduced graphene oxide passivation layer fabrication.....               | 48        |
| 4.2.4 Characterization .....                                                  | 50        |
| 4.2.5 Modelling.....                                                          | 51        |
| 4.3 Results and Discussion.....                                               | 53        |
| 4.3.1 Characterization of electrodes.....                                     | 53        |
| 4.3.2 Annealing study .....                                                   | 55        |
| 4.3.3 Surface temperature distribution under current flow .....               | 56        |
| 4.3.4 Electrode failure under current flow .....                              | 58        |
| 4.3.5 Modeling of current in a nanowire network .....                         | 61        |
| 4.3.6 Joule heating modelling of nanowire electrodes.....                     | 63        |
| 4.3.7 Managing Joule heating .....                                            | 66        |
| 4.4 Conclusion.....                                                           | 68        |
| <b>Chapter 5 Integration of silver nanowire electrodes into devices .....</b> | <b>70</b> |
| 5.1 Integration of silver nanowire electrode into smart windows .....         | 71        |
| 5.1.1 Introduction.....                                                       | 71        |
| 5.1.2 Device fabrication .....                                                | 72        |

|                                                                                                                          |           |
|--------------------------------------------------------------------------------------------------------------------------|-----------|
| 5.1.3 Performance of the fabricated smart windows.....                                                                   | 73        |
| 5.1.4 Conclusions.....                                                                                                   | 78        |
| 5.2 Conformal and Transparent AZO/Ag Nanowire Composite Electrodes for Flexible 3-Dimensional Nanowire Solar Cells ..... | 79        |
| <b>Chapter 6 Growth of nanocubes on silver nanowires .....</b>                                                           | <b>81</b> |
| 6.1 Introduction .....                                                                                                   | 81        |
| 6.2 Experiment setup.....                                                                                                | 83        |
| 6.3 Results and discussion.....                                                                                          | 84        |
| 6.4 Conclusions .....                                                                                                    | 89        |
| <b>Chapter 7 Summary and Future work .....</b>                                                                           | <b>90</b> |
| 7.1 Summary .....                                                                                                        | 90        |
| 7.2 Future work .....                                                                                                    | 92        |
| 7.2.1 Extend the stability of silver nanowires under current flow .....                                                  | 92        |
| 7.2.2 Integrating smooth silver nanowire electrodes into OLEDs .....                                                     | 92        |
| 7.2.3 Applications of nanocube/nanowire structures .....                                                                 | 93        |
| <b>References.....</b>                                                                                                   | <b>94</b> |

# List of Figures

|                                                                                                                                                                                                                              |    |
|------------------------------------------------------------------------------------------------------------------------------------------------------------------------------------------------------------------------------|----|
| Figure 1.1 Schematic of a typical organic solar cell.....                                                                                                                                                                    | 1  |
| Figure 1.2 Optical spectra of typical ITO films including reflection (R) and transmittance (T) <sup>[1]</sup> .....                                                                                                          | 2  |
| Figure 1.3 Transmittance as a function of sheet resistance for four alternative materials: graphene,<br>single wall carbon nanotubes (SWNT), copper nanowires (CuNWs), and silver nanowires<br>(AgNWs) <sup>[19]</sup> ..... | 7  |
| Figure 1.4 Schematic illustration of silver nanowires grown in solution by the polyol method <sup>[23]</sup> .<br>.....                                                                                                      | 8  |
| Figure 1.5 Schematic set-up of a spectrophotometer for measuring specular transmittance.....                                                                                                                                 | 9  |
| Figure 1.6 Set-up of using an integrating sphere to measure both diffusive and specular<br>transmittance <sup>[24]</sup> .....                                                                                               | 9  |
| Figure 1.7 Two resistors with the same sheet resistance and total resistance.....                                                                                                                                            | 11 |
| Figure 1.8 schematic of 4-point probe measurement set up. ....                                                                                                                                                               | 12 |
| Figure 1.9 Example of an AFM line scan of a silver nanowire electrode. ....                                                                                                                                                  | 13 |
| Figure 2.1 Schematic of silver nanowire deposition using the Mayor rod method. ....                                                                                                                                          | 21 |
| Figure 2.2 (a) Fabricated silver nanowire transparent electrode with a sheet resistance of 12 Ω/sq.<br>(b) SEM image of a film consisting of 90 nm diameter silver nanowires on a glass substrate. ....                      | 21 |
| Figure 2.3 Transparency vs. wavelength of two silver nanowire transparent electrodes including<br>the glass substrates (transmittance of the plain glass is 91% at 550 nm). ....                                             | 23 |
| Figure 2.4. Transmittance of the silver nanowire film in the infrared (excluding the substrate). .                                                                                                                           | 24 |
| Figure 2.5 (a) SEM image of a silver nanowire network. (b) Binary black and white image made<br>using ImageJ to calculate nanowire surface coverage and therefore cost. ....                                                 | 26 |

|                                                                                                                                                                                                                                                                                                                                                                                          |    |
|------------------------------------------------------------------------------------------------------------------------------------------------------------------------------------------------------------------------------------------------------------------------------------------------------------------------------------------------------------------------------------------|----|
| Figure 2.6 Transparency (at 550 nm) versus sheet resistance for several transparent electrode materials. The data for the silver nanowire electrodes are from my own experiments and the remainder of the data in the plot is from [ <sup>63-65</sup> ] .....                                                                                                                            | 27 |
| Figure 3.1 (a) Rolling machine (b) schematic of the hot-rolling process .....                                                                                                                                                                                                                                                                                                            | 33 |
| Figure 3.2 AFM image of the silver nanowire electrode (a) annealed and then rolled at room temperature (S2) (b) rolled only at room temperature (S4) (c) hot rolling at 80 °C (S4).....                                                                                                                                                                                                  | 35 |
| Figure 3.3 SEM images of tilted (45 <sup>0</sup> ) silver nanowire films on PET after (a) annealing and (b) hot-rolling. (c) SEM image of a tilted (85 <sup>0</sup> ) hot-rolled electrode, which shows that the nanowires are embedded in the substrate surface. ....                                                                                                                   | 38 |
| Figure 3.4 AFM images of silver nanowire electrodes on PET after (a) annealing (S1) and (b) hot-rolling (S5). (c),(d) Line scan data corresponding to the black dashed lines in (a) and (b), respectively. ....                                                                                                                                                                          | 40 |
| Figure 4.1 (a) Schematic of a typical organic solar cell module. (b) Planar view of the transparent electrode.....                                                                                                                                                                                                                                                                       | 48 |
| Figure 4.2 Graphene oxide blocking layers. (a) Schematic illustrating GO monolayer deposition on AgNW/PET film. (b) Secondary electron SEM image showing contrast between GO film (light) and some pinholes exposing the hydrophobic (HOPG) substrate (dark). (c) Contact-mode AFM image of GO film on mica. (d) Histogram of sheet thickness estimated from AFM imaging as in (c). .... | 54 |
| Figure 4.3 Sheet resistance changes of the nanowire and nanowire-RGO electrodes at 70 °C in air. ....                                                                                                                                                                                                                                                                                    | 56 |
| Figure 4.4 Temperature profiles of electrodes, measured using a thermal imaging camera, when 20 mA/cm of current is flowed in the direction of top to bottom. (a,b) Surface temperature of ITO,                                                                                                                                                                                          |    |

|                                                                                                                                                                                                                                                                                                                                                                                         |    |
|-----------------------------------------------------------------------------------------------------------------------------------------------------------------------------------------------------------------------------------------------------------------------------------------------------------------------------------------------------------------------------------------|----|
| (c) 3D temperature profile of ITO after 60 s. (d,e) Surface temperature of the AgNW electrode, (f) 3D temperature profile of the AgNW electrode after 10s. (g,h) Surface temperature of the AgNW-RGO electrode, (i) 3D temperature profile of the AgNW-RGO electrode after 60 s.....                                                                                                    | 58 |
| Figure 4.5 (a) Temperature and sheet resistance of a AgNW electrode over time under a current density of 20 mA/cm. (b), (c) SEM images of nanowires after electrode failure.....                                                                                                                                                                                                        | 59 |
| Figure 4.6 (a) Temperature and sheet resistance vs. time of a AgNW-RGO electrode under a current density of 20 mA/cm. (b), (c) SEM images of the electrode after failure indicating melting of the plastic substrate.....                                                                                                                                                               | 61 |
| Figure 4.7 (a) Silver nanowire electrode model with a sheet resistance of 60 ohms/sq (red dots show nanowire junctions and endpoints) (b) The distribution of current densities in individual nanowire segments (i.e. between two red dots) of the nanowire electrode. ....                                                                                                             | 62 |
| Figure 4.8 Steady state thermal profile of a (a) AgNW and (b) RGO-passivated AgNW under a current density of $1.6 \times 10^5$ A/cm <sup>2</sup> . (c) Simulated thermal profile of ITO film on PET under the same current (d) Calculated steady state temperature of individual unpassivated and passivated silver nanowires on PET substrates under different current densities ..... | 64 |
| Figure 4.9 (a) Silver nanowire electrode model with a sheet resistance of 20 ohms/sq (red dots show nanowire junctions and endpoints). (b) The distribution of current densities in individual nanowire segments (i.e. between two red dots) of the 20 ohms/sq nanowire electrode. ....                                                                                                 | 66 |
| Figure 4.10 Steady state thermal profile of a (a) AgNW and (b) RGO-passivated AgNW under a current density of $0.7 \times 10^5$ A/cm <sup>2</sup> . (c) Calculated steady state temperature of individual unpassivated and passivated silver nanowires on PET substrates under different current densities .....                                                                        | 67 |
| Figure 5.1 Schematic of the cross-section of the PDLC smart window. ....                                                                                                                                                                                                                                                                                                                | 73 |

|                                                                                                                                                                                                                                                                                                                                                                     |    |
|---------------------------------------------------------------------------------------------------------------------------------------------------------------------------------------------------------------------------------------------------------------------------------------------------------------------------------------------------------------------|----|
| Figure 5.2 (a) Transparency spectra of silver nanowire and ITO films of the same sheet resistance.                                                                                                                                                                                                                                                                  |    |
| (b) SEM image of the silver nanowire electrode .....                                                                                                                                                                                                                                                                                                                | 74 |
| Figure 5.3 Example of a nanowire electrode-based PDLC smart window with (a) 85 V (on state) which corresponds to an electric field of 3.4 V/ $\mu$ m and (b) 0 V (off state) applied across the two electrodes. The effect of voltage on the (c) specular transmittance and (d) haze of the nanowire-based and ITO-based PDLC window at a wavelength of 550 nm..... | 75 |
| Figure 5.4 (a) Specular transmittance and (b) reflectance of the silver nanowire and ITO PDLC windows in the “on” and ‘off’ states.....                                                                                                                                                                                                                             | 76 |
| Figure 5.5. (a) schematic of nanowire solar cell structure (b) SEM images of Ag NWs coated on 3-D hybrid NWSCs using the same Ag NW coating density (2x) at anneal temperatures of 200°C. Unlabeled scale bars are 1 $\mu$ m.Credit to Minoli K. Pathirane. ....                                                                                                    | 80 |
| Figure 6.1 90 nm diameter silver nanowires before (a) and after annealing at 100 °C for 3 days (b) and 7 days (c). (d) 200 nm diameter nanowires after annealing at 100 °C for 7 days.....                                                                                                                                                                          | 85 |
| Figure 6.2 Energy-dispersed X-ray spectroscopy (EDS) spectrum from (a) a portion of a silver nanowire away from a nanocube and (b) a nanocube on a nanowire. ....                                                                                                                                                                                                   | 87 |
| Figure 6.3 Nanocubes with sharp edges lie flat on the surface of silver nanowires, with sidewalls parallel to the nanowire axis. These nanocubes were obtained by annealing 200 nm diameter nanowires at 100 °C for 3 days. ....                                                                                                                                    | 89 |

# Chapter 1

## Introduction

### 1.1 Transparent conductive electrodes

Transparent conductive electrodes (TCEs) or transparent electrodes (TEs) are films that are both electrically conductive and optically transparent. These electrodes are a crucial part of many electronic and optoelectronic devices such as touch panels, liquid crystal displays (LCDs), organic light emitting diodes (OLEDs), solar cells, and transparent heaters. For example, in organic solar cells a transparent electrode preforms as either the cathode or anode which lets light enter the device while at same time collecting the generated electric charges. Figure 1.1 shows a schematic of an organic solar cell having a transparent electrode as a cathode.

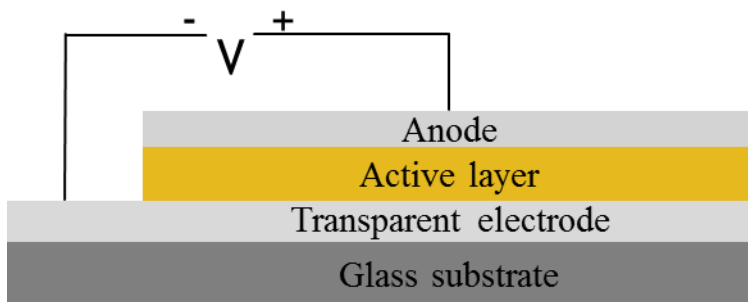


Figure 1.1 Schematic of a typical organic solar cell.

The most commonly materials used as transparent electrodes are transparent conductive oxides (TCOs) such as indium tin oxide (ITO) and aluminum doped zinc oxide (AZO). Films of transparent conductive oxides are transparent to visible light since their band gap energies are higher than the energy of photons in the visible range. Figure 1.2 shows the optical spectrum of

ITO. ITO has a band gap of 3.8 eV [1]. Due to this band gap, ITO absorbs a large portion of light with wavelengths below 300 nm. Transmittance also decreases exponentially for wavelengths above 1000 nm which is related to the collective oscillation of conduction band electrons, called plasma oscillations [1]. The transmittance and conductivity of transparent conductive oxide films can be controlled by varying the thickness of the deposited film. Thicker films result in a more conductive, but less transparent electrode. This is generally the case for transparent electrodes: there is a trade-off between high transmittance and high conductivity.

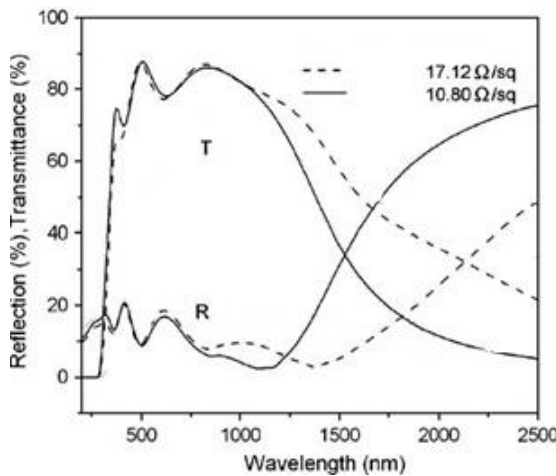


Figure 1.2 Optical spectra of typical ITO films including reflection (R) and transmittance (T) [1].

In the last decade, the market of electronic displays and touch screens has increased drastically. For example, 362 million touch panels were produced in 2010 with an increase of 20% each year up to 2014 [2]. In addition, new device technologies call for new features for transparent electrodes like mechanical flexibility, simple fabrication processes, low cost and light weight. ITO cannot meet all the expectations for the next generation of electronics. ITO has ceramic properties, so it is not flexible; a strain as low as 2-3 % can initiate cracks in ITO films on flexible substrates which reduces electrode conductivity and thus the performance of the device [3]. Secondly, indium is a rare element and the price of indium is volatile with an overall increasing trend [4]. Thirdly, the fabrication of ITO is costly since it requires high temperatures and high vacuum for control over

the thickness and doping concentration <sup>[4]</sup>. Also, it is deposited by sputtering which can damage underlying layers in the case of organic devices. Fourthly, ITO has a high index of refraction which is not suitable for display applications since it reflects light whereby decreasing the brightness of the screen. An additional coating needs to be applied to solve this problem, leading to additional cost.

Extensive research has been devoted to solving the problems associated with ITO transparent electrodes. For example, to make a mechanically flexible electrode, ITO has been laminated onto substrates like polyethylene terephthalate (PET), and ITO with various elemental ratios have been investigated to improve the mechanical properties of the film <sup>[4]</sup>. However, these approaches not only add additional manufacturing cost but also reduce the optical and electrical performance of such electrodes. Therefore, over the past decade many researchers have tried to find an alternative material to replace ITO and several potential candidates have emerged. Each candidate has advantages and disadvantages and more investigation is needed before any of them can be used commercially.

## **1.2 Alternative materials**

Current noteworthy materials for ITO substitution are carbon nanotubes (CNTs), graphene, transparent conductive polymers, metal grids, and random meshes of metal nanowires.

### **1.2.1 Carbon nanotubes**

Carbon nanotubes, which were first synthesized in 1990 <sup>[5]</sup>, have unique electrical and optical properties such as their electron mobility which can reach more than  $100\ 000\ \text{cm}^2/\text{V}\cdot\text{s}$  <sup>[6]</sup>. Random networks of carbon nanotubes were proposed as an attractive alternative to ITO. However, the conductivity of nanotube films are much lower than ITO because of high resistances at the junction of overlapping nanotubes in the network <sup>[6]</sup>. In addition, in the synthesis process of the nanotubes,

both semiconductor and metal nanotubes are formed and it is not easy to separate out only the metal nanotubes. The semiconducting tubes do not contribute much to the film conductivity, but their presence lowers transparency. Several methods including acid treatment of nanotubes have been proposed to reduce the sheet resistance of the nanotube films <sup>[7]</sup>. However, the sheet resistance and transparency of these electrodes are still lower than that of ITO and are thus not yet a promising replacement.

### **1.2.2 Graphene**

Graphene is another alternative for replacing ITO. Among the interesting properties of graphene is the capability of adding external dopants which results in high in-plane conductivity of graphene sheets. The thickness of the graphene sheets is on the order of a few nanometers and thus graphene sheets are relatively transparent to visible light.

The major concern of using graphene is the complexity of fabricating a single sheet of graphene of large area. More often, instead of a single sheet of graphene, networks of graphene flakes are synthesized. These network of flakes result in very high sheet resistance, in the range of several  $k\Omega$  <sup>[4]</sup>, because there is a high contact resistance between flakes <sup>[8]</sup>. Although researchers have introduced new methods of fabricating a single sheet of graphene, such as the high temperature CVD method, the cost of this method is relatively high <sup>[9]</sup> and the sheet resistances in these single sheets are still not low enough to be useful in most applications.

### **1.2.3 Conductive polymers**

Transparent conductive polymers have interesting properties like high flexibility, low cost and light weight. Several companies have been trying to use them in various devices such as touch panels and organic electronics <sup>[10]</sup>. The combination of Poly (3, 4-ethylenedioxythiophene) and

poly (styrene sulfonate), known as PEDOT:PSS, is the most common transparent conductive polymer being used in organic electronics.

One of the major problems of conducting polymers is their instability in air due to absorption of oxygen and moisture. For example, PEDOT:PSS degrades in air in a short time. To solve this problem, extensive research is being done to synthesize more stable conducting polymers. Fujitsu has used a type of polythiophene, which is more stable in air, for their organic touch panels [10]. Another major problem is that the conductivity and transparency of conductive polymers is low and can therefore not replace ITO in many applications. One possibility is to combine conducting polymers with other materials such as graphene or nanostructured metals to enhance conductivity [11,12].

#### **1.2.4 Metal nanowire electrodes**

Because of the low conductivity of carbon nanotube films, graphene, and transparent conducting polymers, metal nanostructures are an appealing alternative. However, because of the very low transparency of metals to visible light, fabrication of transparent metallic electrodes was not easy until the emergence of nanotechnology and nanostructured materials. Metal nano-grids, thin metal films (of less than 10 nm thickness) and random meshes of metal nanowires are three common structures used to make transparent electrodes [13–15]. Among these structures, random networks of nanowires became the most interesting due to nanowire films being easier to synthesize and having better optoelectronic properties; grids have to employ lithography or printing, and the transmittance of thin metal films are low.

Metal nanowires have diameters that are typically less than 100 nm and lengths of 1  $\mu\text{m}$  or more. Metal nanowires such as copper or silver can be synthesized in solution, and then deposited on

transparent substrates such as glass or plastic to create a random conductive mesh. These films are similar to carbon nanotube films, except in this case all wires are metallic. And because metal junctions can be sintered, the nanowire-nanowire junction resistance can be much lower than for carbon nanotubes. The mesh transparency can reach 90% for a sheet resistance below  $10 \Omega/\square$ , which makes the transparency and conductivity similar to that of ITO and thus suitable for transparent electrode applications [15]. Sheet resistance and transparency of the films can be controlled by varying the nanowire density: denser films are more conductive but less transparent [15].

Simple and cheap fabrication, high transparency, and low sheet resistance are advantages of metal nanowire structures. Moreover, the nanowire electrodes are mechanically flexible. They are also much more transparent in the infrared (IR) range than ITO which makes them more suitable for multi-junction solar cells and other applications where transparency in the IR is required. A solution of nanowires can be deposited in atmosphere using simple and inexpensive deposition methods like spin coating [16], spray coating [17], and Meyer rod coating [15]. Furthermore, silver nanowire films can be fabricated either at room temperature [18], or at low annealing temperatures [15], which make them compatible with plastic substrates in producing flexible electrodes. Silver is chosen because it has the highest conductivity amongst all metals. Although silver is an expensive element, so little of it is used in a nanowire film that material costs are lower than ITO. Figure 1.3 compares the transparency vs. sheet resistance of silver nanowire electrodes with other alternatives. So far, silver nanowire electrodes show superior performance compared to graphene and carbon nanotubes.

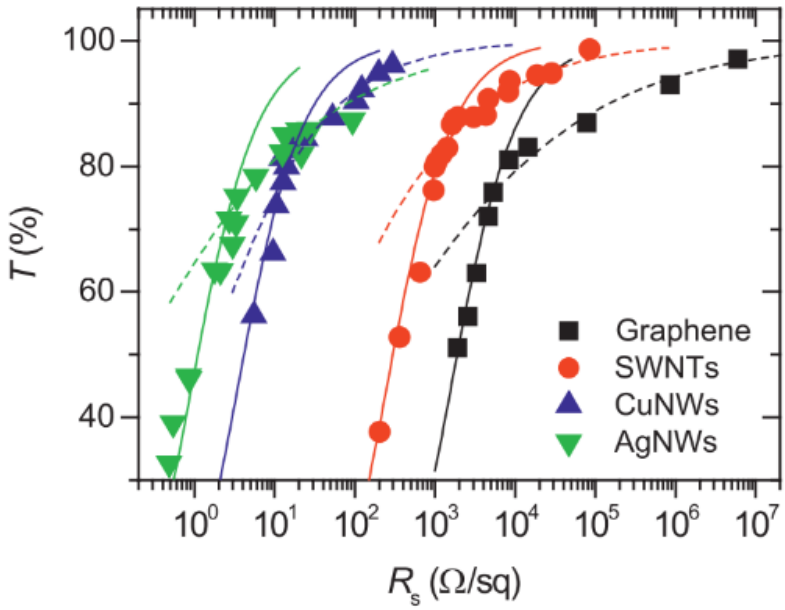


Figure 1.3 Transmittance as a function of sheet resistance for four alternative materials: graphene, single wall carbon nanotubes (SWNT), copper nanowires (CuNWs), and silver nanowires (AgNWs)<sup>[19]</sup>.

Films of copper nanowires are also being investigated as a transparent conductor since copper is cheaper than silver and its conductivity is nearly as high. Reported copper transparent electrodes show superior performance than carbon nanotube films, but not as good as silver nanowire films and ITO<sup>[20]</sup>. The main concern of using copper nanowires is their instability in air due to the fact that copper quickly reacts with atmospheric oxygen. Thus, during the annealing step of copper nanowire electrode fabrication, they have to be annealed in a neutral atmosphere like a hydrogen tube furnace or vacuum furnace, which increases the complexity of fabrication, and they also likely need to be well passivated to prevent oxidation during the use of the electrodes<sup>[21]</sup>.

### 1.3 Synthesis of silver nanowires

The polyol method is a cheap and simple method of synthesizing high quality silver nanowires in solution. In this method, a solution of ethylene glycol (EG), poly (vinyl pyrrolidone) (PVP) and NaCl is heated to 170 °C and a mixture of AgNO<sub>3</sub> and EG is gradually added. Adding AgNO<sub>3</sub> to

the solution leads to the creation of  $\text{Ag}^+$  ions which results in the formation of nanoparticles<sup>[22]</sup>. The PVP has a strong interaction with the {100} facets and passivates them; this slows down the addition of silver onto these surfaces of the nanoparticles. The interaction of PVP with {111} facets, however, is weaker. Thus, {111} facets grow faster<sup>[22]</sup> which results in a 1D wire structure. The polyol method results in crystalline silver nanowires with a pentagonal cross-section, with 5 twin-planes extending along the length of the nanowire as shown in Figure 1.4. The nanowires are oriented along the [100] direction, the sidewalls are {100} planes, and two ends of the nanowires are bounded by {111} facets<sup>[23]</sup>.

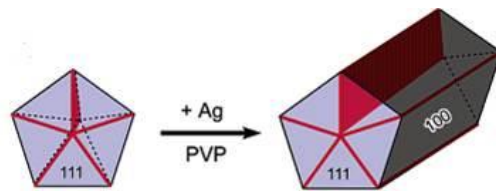


Figure 1.4 Schematic illustration of silver nanowires grown in solution by the polyol method<sup>[23]</sup>.

## 1.4 Characteristics of transparent electrodes

### 1.4.1 Transmittance

When light encounters an object, the incident light can be transmitted, absorbed or reflected. The ratio of transmitted light to incident light is defined as the transmittance of the object, typically stated in a percentage. The transmittance of an object can vary in response to the wavelength of the incident light. Thus, when transmittance of an object is reported the corresponding wavelength needs to be mentioned. All transmittances stated in this report are at 550 nm and in reference to the substrate (i.e. do not include the transmittance of the glass or plastic) unless otherwise stated.

The total transmittance consists of two parts: specular (or direct) and diffusive (forward scattered). Specular transmittance represents the transmitted light travelling in the same

direction as the incident light. This transmittance can be measured using the default setup of a spectrophotometer, where the detector is placed behind the object in-line with the source of the light. Figure 1.5 shows a schematic set up of a spectrophotometer for measuring specular transmittance. Diffusive transmittance represents transmitted light scattered by the object. To measure this portion, an integrating sphere is needed, which collects all transmitted light including diffusive and specular. A schematic of such an integrated sphere is illustrated in Figure 1.6.



Figure 1.5 Schematic set-up of a spectrophotometer for measuring specular transmittance.

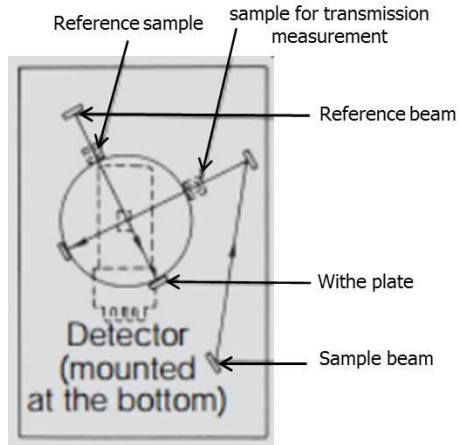


Figure 1.6 Set-up of using an integrating sphere to measure both diffusive and specular transmittance [24].

For samples such as plain glass and ITO electrodes, diffusive transmittance is not significant since they scatter very little light. However, silver nanowire electrodes do scatter a portion of the incident light. The haze factor is defined as the ratio of the diffusive transmittance to specular transmittance. High haze is not good for display applications since it can blur sharp lines. However, high haze, which means that there is more scattered light, can benefit solar cell applications by increasing the

path length of the incoming light in the absorbing layer of the device, thereby increasing absorption and power conversion efficiency. The haze factor of silver nanowire electrodes can be less than 2% and higher than 30% depending on the size and density of the nanowire [25]. Therefore, for any applications the haze factor can be managed by controlling the material properties.

#### **1.4.2 Sheet resistance**

Resistivity is one of the elementary parameters of a conducting material. The symbol  $\rho$  with the units  $\Omega \cdot \text{cm}$  represents the resistivity of a material. Resistance is related to resistivity through:

$$R = \rho \frac{L}{Wt},$$

where L is the length of the sample along which the current flows, and W and t are the width and thickness of the sample. Since the thicknesses of films are often difficult to measure, sheet resistance is defined to represent resistance per square area of a thin film with the units  $\Omega/\text{sq}$  (Ohms per square) and is given by

$$R_s = \frac{\rho}{t}$$

So,

$$R = R_s \frac{L}{W}$$

Thus, the total resistance of a film is proportional to the number of squares that can be drawn on the conducting surface area. Figure 1.7 shows a top view of two resistors with the same sheet resistance. Although their sizes are different, the numbers of drawn squares are equal. Thus, the total resistance for both resistors is the same.

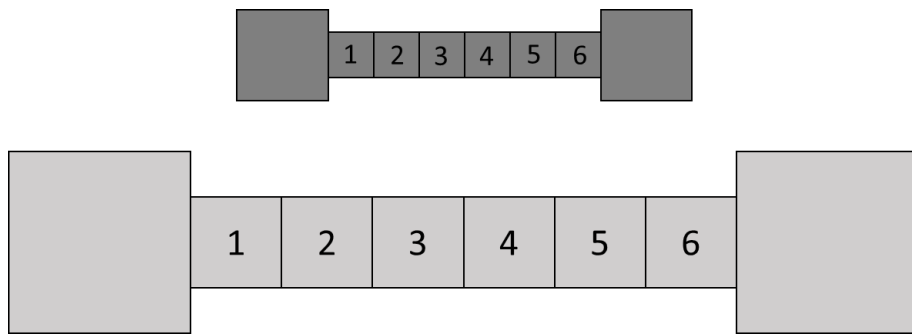


Figure 1.7 Two resistors with the same sheet resistance and total resistance.

Sheet resistance of thin films is usually measured with a 4-point probe measurement method. The schematic of the 4-point probe measurement set up is shown in Figure 1.8. In this method, 4 inline probes touch the films with same spacing ( $s$ ), the two outer probes are used to apply a current which induces a voltage ( $V$ ) across the two inner probes. By measuring the induced voltage, the resistivity and sheet resistance of the films can be calculated using the following equations:

$$\rho = 2\pi s \frac{V}{I} [\Omega \cdot cm]$$

$$R_s = \frac{\pi}{\ln 2} \frac{V}{I} = 4.53 \frac{V}{I} \left[ \frac{\Omega}{sq} \right]$$

The 4-point method is suitable for uniform films which enables evaluating electrical properties independent of their thickness. However, for nanowire network films this method is not ideal since this film is not uniform. Measuring sheet resistance of the random network at a localized area does not show the electrical properties of the entire film. Particularly, because the nanowires are randomly distributed over the substrate, the number of nanowires in contact with the probe will

vary depending on where exactly the probe is located. One solution to determine the average sheet resistance of the nanowire film is to probe different areas and take the average of the measured values. Another method to evaluate the average sheet resistance of the film is to use regular 2-point probe measurement using a multimeter. In this case metal contacts at two edges of a sample are connected to a multimeter to measure the resistance of the film. Then the sheet resistance can be calculated by multiplying the resistance by the ratio of width to the length of the sample ( $W/L$ ). The resistance of the tape is 0.005 which is 3 orders of magnitude lower than the resistance of the nanowire film, and thus the 2-probe method is a good approximation. Indeed, results showed that the numbers from two-point measurement method is close to the average of 4-point probe numbers. Therefore, the 2-point probe measurement can be used to determine the sheet resistance of the nanowire networks where average sheet resistance of the film is desired.

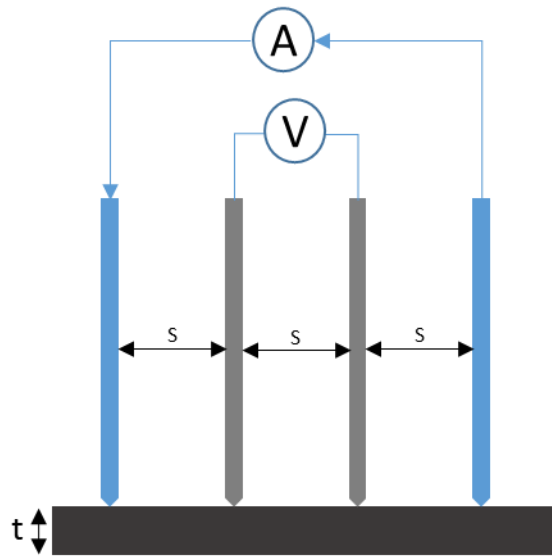


Figure 1.8 schematic of 4-point probe measurement set up.

### 1.4.3 Roughness parameters

Atomic force microscopy (AFM) can be used to understand the topographic properties and surface roughness of transparent electrodes. The common surface roughness parameters are average roughness, root-mean-square, and peak-to-valley. Figure 1.9 shows an example of an AFM line scan which shows the sample height along a line on the sample.

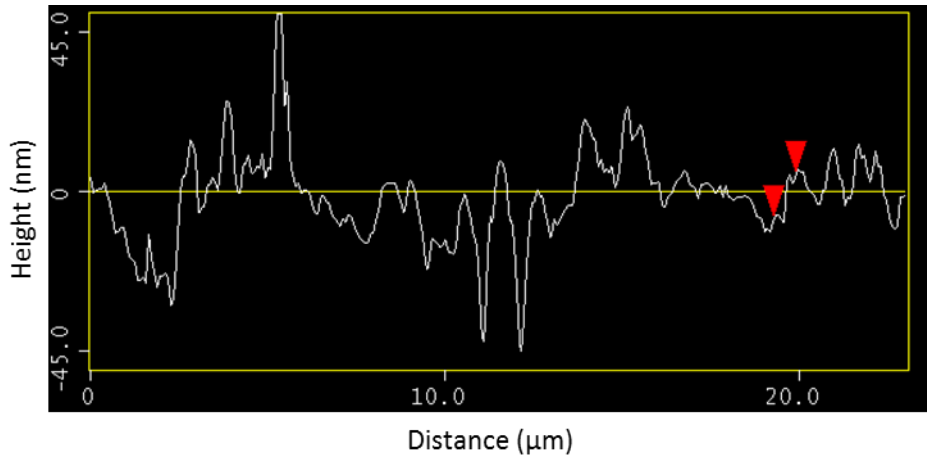


Figure 1.9 Example of an AFM line scan of a silver nanowire electrode.

Average roughness ( $R_a$ ) is the most commonly used parameter to report the surface roughness and is easy to measure. This is defined as the average of the absolute height values (y-axis), with respect to the mean line, and can be shown as<sup>[26]</sup> :

$$R_a = \frac{1}{L} \int_0^L |Y(x)| dx \quad \text{or} \quad R_a = \frac{1}{n} \sum_{i=1}^n |Y_i|$$

Root mean square, known as RMS, is another important parameter that is used to describe the surface roughness. This parameter is more sensitive to large deviations of the heights. In this case the mean line is where the sum of the squares of the height values are equal to zero. The mathematical expression for RMS is<sup>[26]</sup> :

$$RMS = \sqrt{\frac{1}{L} \int_0^L [Y(x)]^2 dx} \quad \text{or} \quad RMS = \sqrt{\frac{1}{n} \sum_{i=1}^n |Y_i|^2}$$

Maximum peak to valley is also an important parameter, especially for electrodes used in thin film devices, which shows the maximum distance between the highest and the lowest point in one scanned line or area<sup>[26]</sup>. In the case of thin film electronics, if the thickness of the layers between the electrodes is smaller than the peak-to-valley value of the electrodes, there is a high chance of creating an electric short across the device which can lead to device failure.

## 1.5 Silver nanowire electrode applications

### Solar cells

Transparent conductive electrodes have many device applications, as mentioned above. Organic solar cells have been the most reported device for which silver nanowire electrodes have been used. Nanowire electrodes have several unique advantages for solar cells: (i) Nanowire films generally forward scatter more light compared to ITO films which results in increased light absorption and leads to higher efficiency<sup>[27]</sup>. (ii) Nanowire films are mechanically flexible whereas ITO is brittle. (iii) Nanowires can be easily deposited on plastic, whereas the deposition parameters for ITO must be modified to meet the low thermal budget of plastics and therefore the properties of ITO are worse on plastic than glass. (iv) The fabrication cost of the nanowire electrodes is lower than that of ITO. (v) Silver nanowire films are transparent in the infrared range of the light spectrum (chapter 2.2), which can be useful for multi-junction solar cells.

### Film heaters

Transparent heater films are another application of transparent electrodes which can be used in applications such as window defrosters, maintaining the required temperature for liquid crystal display operation, goggle defrosters, and various military and medical applications. ITO thin film heaters are commercially available on the market. However, as will be mentioned later, because of

the disadvantages of ITO like high cost and brittleness, researchers are trying to introduce new transparent heaters based on other alternative materials.

## **OLEDs**

Transparent conductive electrodes are also a necessary component in organic light emitting diodes (OLEDs). Some research groups have integrated silver nanowire films into OLEDs and showed improvement in electroluminescence of the OLEDs compared to ITO-based OLEDs [28].

## **Touch panels**

Touch panels need two layers of transparent conductive film. Recently 3M Company has introduced a new generation of conductive films for touch screen applications based on silver nanowire networks [29].

## **Smart windows**

Electronically switchable windows, or “smart windows”, enable alteration of their optical properties (transparency, translucency) with an applied electric field. There are currently three different technologies used to fabricate optoelectronically active components for smart window technology: chromic materials, suspended-particles, and polymer dispersed liquid crystals (PDLC)<sup>[30]</sup>. All of these technologies need to use two films of transparent electrodes. Like most devices, ITO is the most commonly used transparent electrodes in smart windows. Alternative materials that were mentioned above have been explored to replace ITO films in smart windows. For example, carbon nanotube films have been used in electrochromic smart windows. However, these electrodes cannot reach the same transmittance as ITOs at a given sheet resistance<sup>[31]</sup>. Other materials such as conductive polymers (PEDOT:PSS) and Ag grids have also been integrated into electrochromic devices. However, the performance of these device such as their transmittance is lower than that of the ITO based device. In addition, the PEDOT:PSS is known to have low

stability in air<sup>[32]</sup>. Silver nanowire electrodes have been integrated into electrochromic devices and showed acceptable performance for flexible and stretchable devices<sup>[33]</sup>. In this thesis, silver nanowires are integrated into PDLC smart windows for the first time and the results are compared with ITO based devise which is discussed in chapter 5.

## 1.6 Silver nanowire electrode challenges

### 1.6.1 Surface roughness and weak adhesion

In spite of all the advantages of nanowire electrodes, there are certain issues that need to be addressed before their widespread use in devices. One of these most important issues is their surface roughness. Because there are typically junctions on an electrode where 3 or more nanowires are stacked on top of one another, maximum peak-to-valley values can reach 3 times the diameter of the nanowires or more<sup>[34,35]</sup>. 90 nm diameter nanowires are commonly used, and so these electrodes have peak-to-valley values around or exceeding 270 nm. This is problematic for many devices, especially ones that consist of thin layers. In organic electronic devices, for example, the low electron mobility and fast recombination times require organic layers to be less than 100 nm thick (typically 40 – 80 nm depending on the device and materials used)<sup>[35,36]</sup>. Several reports where silver nanowire electrodes have been used in organic solar cells have reported lower efficiencies than equivalent devices built on ITO. The rough surface of the nanowire electrodes causes a lower shunt resistance, which hinders the efficiency of the solar cells<sup>[37–39]</sup>. The roughness also leads researchers to use a thicker layer of poly(3,4-ethylenedioxythiophene) poly(styrenesulfonate) (PEDOT:PSS) than is typically used on ITO-based devices<sup>[38]</sup>. This thicker layer decreases transparency and therefore also reduces efficiency. Other methods to reduce surface roughness include depositing a non-conductive polymer layer over the nanowire film

followed by peel-off to expose the nanowire surfaces, and pressing nanowires on their substrate. More details of the possible methods and the results are discussed in chapter 3.

Weak adhesion of nanowires to the substrate is another important issue. Without any special processing, scratches or shear stresses on the surface can easily wipe the nanowires from the surface [40]. The proposed methods discussed above to reduce the surface roughness can also significantly increase the adhesion of the nanowire to their substrate. For example, adding an additional layer on top of the nanowire film can increase the nanowire's adhesion drastically [41].

As a part of my PhD program, I developed a simple method of minimizing the surface roughness and increase the adhesion of silver nanowire films on plastic substrates. This is reported in chapter 3.

### **1.6.2 Instability of silver nanowire electrodes**

Another major concern of silver nanowire transparent electrodes is their instability in air, at elevated temperatures, and under current flow. Silver nanowires corrode in air by reacting with small amounts of sulfur and creating silver sulfide on the surface [42][43]. In addition, nanowires are not stable structures and at elevated temperatures (above 200 °C) their instability is accelerated and the cylindrical shape of the nanowires change to spheres [44]. The change of the nanowires from cylinder to spheres is called spheroidization. This morphological instability is related to Rayleigh instability or so called capillary instability. Atoms start moving to minimize the surface energy of the nanowire cylinder [45] and a perturbation wave is formed. If this wavelength of this wave increases more than a specific number  $\lambda_0 = 2\pi R_0$ , where  $R_0$  is the initial diameter of the nanowire, the nanowire become unstable [46]. This wave creates a stress in the nanowire and make curvatures that results in formation of the spheres. The wavelength of the perturbation wave is

smaller for smaller diameter nanowires. This means that the spheroidazation in nanowires with smaller diameter happens faster due to higher stress in the nanowires. The effective parameters on the time for spheroidization can be explained by the following equations<sup>[44,46,47]</sup>:

$$\frac{\partial n}{\partial t} = B \frac{\partial^2 K}{\partial s^2}, \quad B = \frac{D_s \gamma \Omega^2 v}{KT}, \quad D_s = D_0 \exp(-\frac{E_a}{KT}) \quad (1)$$

$\frac{\partial n}{\partial t}$  is the motion of the surface with respect to time that represents the surface flux of the atoms.

This depends on the  $\frac{\partial^2 K}{\partial s^2}$ , which is the change in curvature of the surface, and the parameter B, which depends on temperature (T), surface self-diffusion ( $D_s$ ), surface tension ( $\gamma$ ), atomic volume ( $\Omega$ ), number of diffusing species per unit surface area ( $v$ ), and the Boltzmann constant (K). Using this equation, the time for complete spheroidization ( $\tau$ ) was calculated as<sup>[44]</sup>:

$$\tau = \frac{Bt}{(\frac{\pi}{16}r)^4} \quad (2)$$

This equation shows that (i) the spheroidization happens faster for nanowires with smaller diameters (ii) spherodization is accelerated at elevated temperatures (iii) surrounding environment of nanowires such as the substrate and the gaseous around the nanowire affect the speed of nanowire deformation. By changing the environment parameters including the surface self-diffusion, activation energy ( $E_a$ ) will change and affect the spherodization rate. For example, annealing nanowires in air, nitrogen, or hydrogen will lead to different time to spheroidization due to the different self-diffusion and activation energy values. This shows that the stability of the nanowire can be improved by treating the surface of the nanowires. It will be shown in chapter 4 that deposition of a reduced graphene layer on silver nanowire can increase the stability of the nanowires at elevated temperatures.

## **1.7 Outline of this thesis**

This thesis consists of five main parts: First, silver nanowire electrodes are fabricated and characterized (Chapter 2). Second, the hot rolling of nanowire electrodes is presented as a method of reducing the surface roughness of the electrodes (Chapter 3). Third, the instability of the nanowires under current flow and the effects of Joule heating are investigated. In addition, the effects of a passivation layer of reduced graphene oxide (RGO) on the lifetime of the electrodes are discussed (Chapter 4). Fourth, the fabricated nanowire electrodes on PET are integrated into smart windows and 3D thin film solar cells (Chapter 5). Fifth, a simple method of growing silver chloride ( $\text{AgCl}$ ) nanocubes on silver nanowires are proposed for photocatalytic and sensor applications (Chapter 6). Lastly, the results of my research and future plans are summarized in Chapter 7.

# **Chapter 2**

## **Fabrication of nanowire electrodes**

In this chapter, the fabrication process of silver nanowire electrodes is discussed. Silver nanowires are deposited on a substrate using the Mayer rod coating method, and their optical and electrical properties are reported.

### **2.1 Silver nanowire electrode fabrication**

Silver nanowires synthesized by the polyol method (discussed in Ch 1.3) can be dispersed in water or an alcoholic solvent such as isopropyl alcohol (IPA), ethanol or methanol. They can be deposited as films using various solution deposition methods such as spin coating<sup>[48]</sup>, spray coating<sup>[17,49]</sup>, and rod coating<sup>[50–52]</sup>. Spin coating is the most popular deposition method of depositing nanowire films for lab-scale samples due to its simplicity. However, for large-scale fabrication, other methods like spray coating, and Mayer rod coating are more suitable and used more frequently in industry. Since transparent electrodes need to be fabricated on a large-scale eventually, the Mayer rod coating method was selected for nanowire deposition in this work. It is compatible with roll-to-roll techniques and is a standard deposition method used in industry<sup>[53]</sup>. This method is inexpensive and easy to use; just one wire-wound rod is enough for fabrication so there is no need for any complex equipment. Moreover, using this method the solution is distributed uniformly on the substrate. Figure 2.1 shows the schematic deposition process. In this method an ink (silver nanowire solution) is dropped on one side of the samples and then a Mayer rod is rolled over the ink on the substrate and along the rest of the substrate. The thickness of the deposited solution is determined by the diameter of the wire that is wound around the main rod.

The density of the nanowires in the electrode was controlled both by the concentration of the nanowire solution and the number of layers deposited

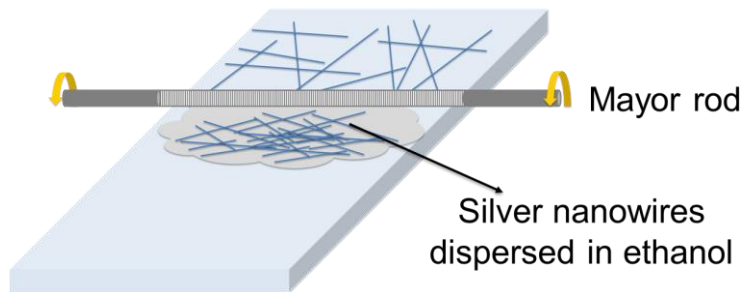


Figure 2.1 Schematic of silver nanowire deposition using the Mayor rod method.

After nanowire deposition, the film was dried in air. Nanowire films on glass substrates were annealed at 200 °C for 30 minutes to get maximum conductivity by sintering the nanowire junctions. However, samples on plastic were annealed at 100 °C for 30 minutes to avoid any deformation of the plastic substrate. Figure 2.2 shows an image of annealed nanowires on a glass substrate.

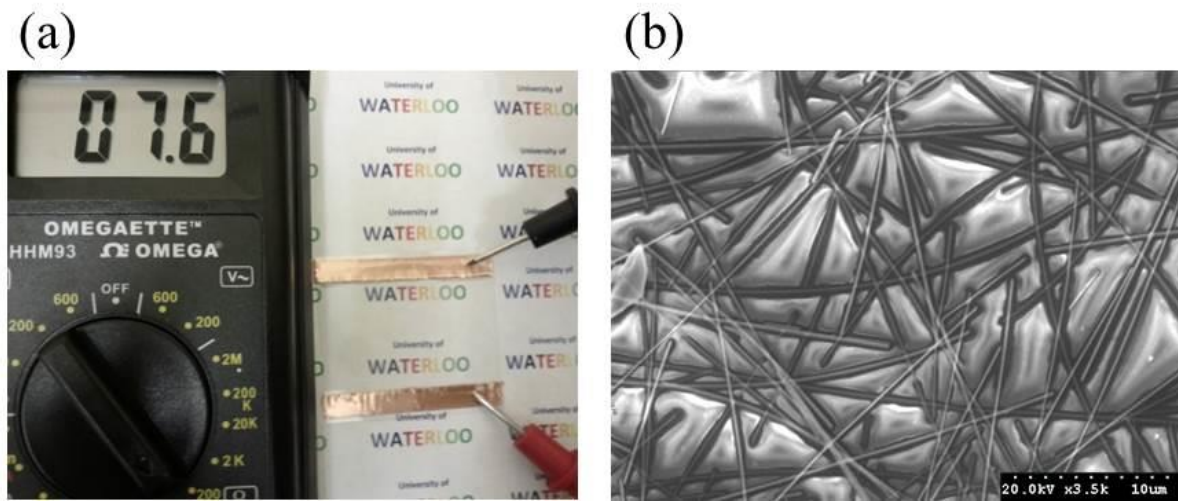


Figure 2.2 (a) Fabricated silver nanowire transparent electrode with a sheet resistance of 12 Ω/sq. (b) SEM image of a film consisting of 90 nm diameter silver nanowires on a glass substrate.

In this work, silver nanowires dispersed in ethanol were purchased from Blue Nano Inc. (Charlotte, NC) with average diameters of 35 and 90 nm and average lengths of 15 μm and 20 μm,

respectively. Both plastic and glass films were used as electrode substrates. Heat stabilized PET film with a thickness of 127 µm was purchased from Dupont Tianjin Inc. and glass slides were purchased from Fisher Scientific Inc. An appropriate size of the nanowire was selected for each study based on their applications. In chapter 3, where surface roughness is critical, nanowire with smaller diameter (35 nm) was used to achieve lower surface roughness (the results for 90 nm diameter nanowire is also reported). For Joule heating and stability purposes in chapter 4, nanowires with 90 nm since they are more stable and morphological changes on the nanowire are more visible on larger nanowires. For device application in chapter 5, nanowires with 35 nm diameters was choose since they result in a more uniform nanowire distribution on the substrate. The smaller distances between nanowires in the film provides a more uniform electric field for smart windows and is more useful in collecting charges in solar cells. In chapter 6, nanowires with various diameters were used to study the effect of nanowire diameter on formation of nanocubes.

## **2.2 Characterizing electrodes**

### **2.2.1 Sheet resistance and transmittance in the visible range**

The most critical characteristics of a transparent electrode are its sheet resistance and transmittance. Sheet resistance was measured with either a 4-point probe machine or a multimeter. In the latter method, sheet resistance is calculated by multiplying the measured resistance by the width to length ratio (W/L), according to the definition of sheet resistance. Both methods were used on several samples and the measured sheet resistances were very similar.

Transmittance of the electrodes was measured with a UV-2501PC Shimadzu spectrophotometer. Two samples with different sheet resistances and transmittances were prepared on glass substrates

by controlling the number of deposited layers, and both their specular and total (diffusive + specular) transmittances were measured for comparison. Figure 2.3 shows the spectra of the samples including the glass substrate. A higher concentration of silver nanowires on the substrate results in lower sheet resistance and transmittance. In addition, as illustrated in Figure 2.3, higher concentration (i.e. lower sheet resistance) results in a higher proportion of the incident light being scattered. In this case, the sample with a sheet resistance of  $65 \Omega/\square$  scatters about 6% of the incident light. However, this amount increases to more than 10% for the sample with a sheet resistance of  $12 \Omega/\square$ .

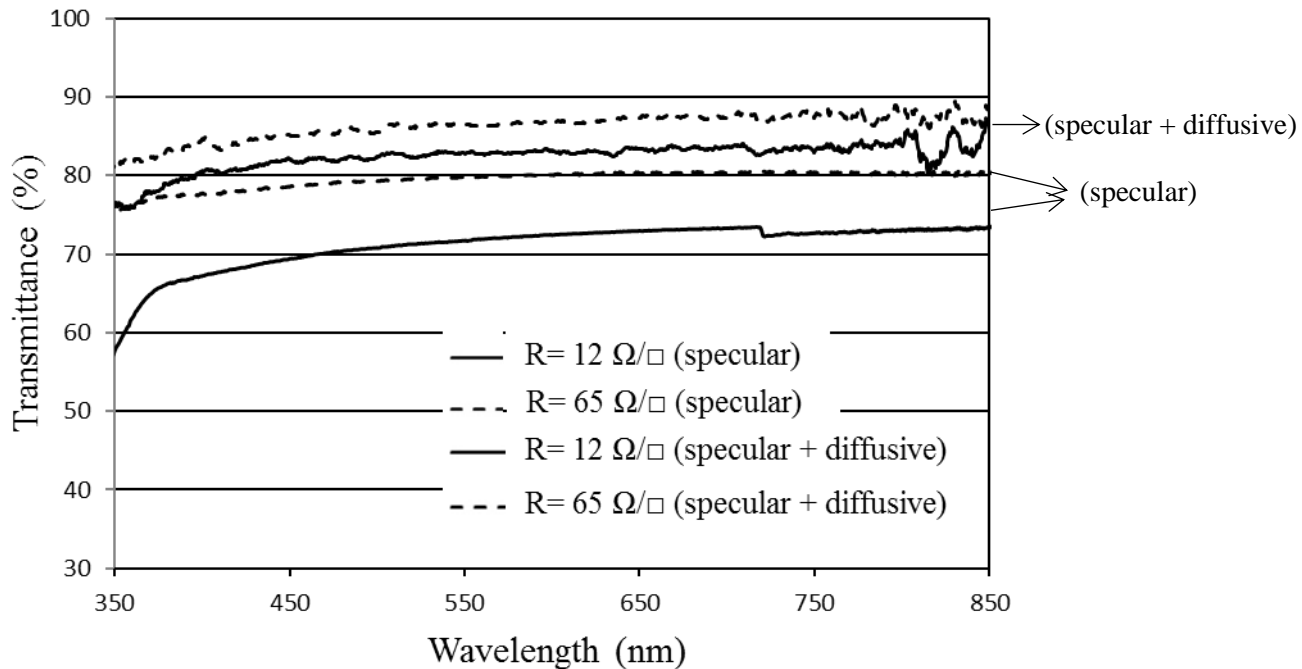


Figure 2.3 Transparency vs. wavelength of two silver nanowire transparent electrodes including the glass substrates (transmittance of the plain glass is 91% at 550 nm).

### 2.2.2 Transmittance in the infrared range

Unlike transparent conductive oxides, in which transparency drops significantly for wavelengths above 1000 nm, silver nanowire films transmit most of the light in the infrared (IR) range.

Figure 2.4 shows the transmittance of a silver nanowire film with a sheet resistance of  $20 \Omega/\text{sq}$  on plastic for wavelengths ranging between 1300 nm to 10,000 nm, taken with a Fourier transform infrared spectroscopy (FTIR) spectrometer. According to the results, the transmittance of the silver does not drop significantly in the infrared range. Transmittance of the same nanowire film in the visible range (at 550 nm) is 87%. Transparency in the IR is desired for some applications such as smart windows where heat modulation is desired. Also in multi-junction solar cells, transparency in the IR range is beneficial for harvesting a larger portion of the sunlight spectrum. It is worth mentioning that the IR transparency plot (Figure 2.4) is a preliminary result to show that the electrode is transparent in the IR range. Most of the oscillations are likely due to noise in the measurement. Similar plots in other reports are not as noisy [50].

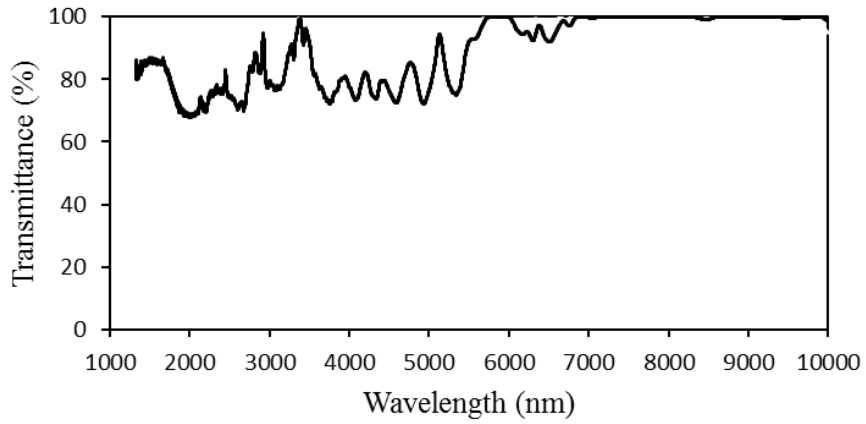


Figure 2.4. Transmittance of the silver nanowire film in the infrared (excluding the substrate).

## 2.3 Cost of nanowire electrodes

The material cost to synthesize silver nanowires in the lab is \$32.58/g [21]. The cost per gram of ITO is much less expensive, at \$2.40/g [54]. However, much smaller amounts of silver are used in a nanowire electrode compared to the amount of ITO used in an ITO electrode. To calculate the

material cost of the silver nanowire electrodes, several SEM images were taken of a silver nanowire electrode with a sheet resistance of  $50 \Omega/\text{sq}$ . The images were analyzed using “ImageJ” software to calculate the surface coverage (Figure 2.5). This is first done by first changing the greyscale image into a black and white binary image. The white pixels for the most part represent the nanowire coverage, and the black pixels represent the background. The ratio of the white pixels to total pixels determines the surface coverage of the nanowires. The mass of silver nanowires in the  $50 \Omega/\text{sq}$  case was calculated to be  $0.02 \text{ g/m}^2$ . This corresponds to a material cost for film formation of  $\$0.70/\text{m}^2$ . The materials cost of a  $50 \Omega/\text{sq}$  ITO electrode, on the other hand, is approximately  $\$1.60/\text{m}^2$ , assuming a required ITO film thickness of 100 nm [55,56] which would require 0.6 g of ITO per square meter [57]. The fabrication cost of ITO is estimated to be  $\$1.10/\text{m}^2$  [58] which needs high temperature and vacuum. Silver nanowire electrodes are deposited using solution deposition methods, do not need vacuum and can be done at room temperature, making its deposition relatively easy compared to the fabrication process of ITO. An estimate of the fabrication cost of nanowire electrodes is not available. Although it is likely cheaper than the fabrication cost of ITO, capital costs of equipment that differ from those used to deposit ITO may need to be taken into consideration.

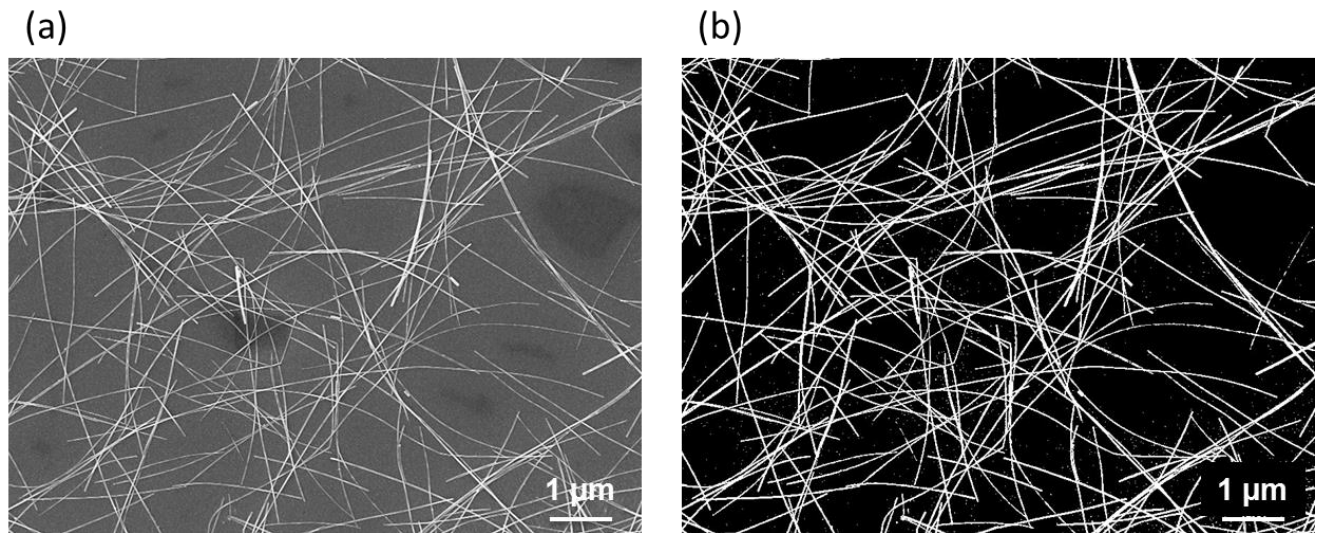


Figure 2.5 (a) SEM image of a silver nanowire network. (b) Binary black and white image made using ImageJ to calculate nanowire surface coverage and therefore cost.

## 2.4 Data comparison

As mentioned, several alternatives have been introduced for ITO replacement. One of the most important properties that an alternative needs to have is compatibility with flexible substrates.

Figure 2.6 and Table 2.1 compare the characteristics, pros and cons of my silver nanowire electrodes on plastic (PET), fabricated with the method described in the next chapter, with the best results that are reported with the alternative materials and commercial ITO-coated PET (excluding their substrate). The ITO-coated PET has higher sheet resistance at a given transparency compared to ITO on glass due to lower deposition temperature for plastic substrate. Because high transparency and low resistance is desired, the closer the data points are to the top left corner, the better. Results indicate that the silver nanowire transparent electrodes have better performance than the competing alternative materials and commercial ITO-coated PET. Although the results of patterned Ag grids look promising, their fabrication method is complicated and not compatible with roll-to-roll processes.

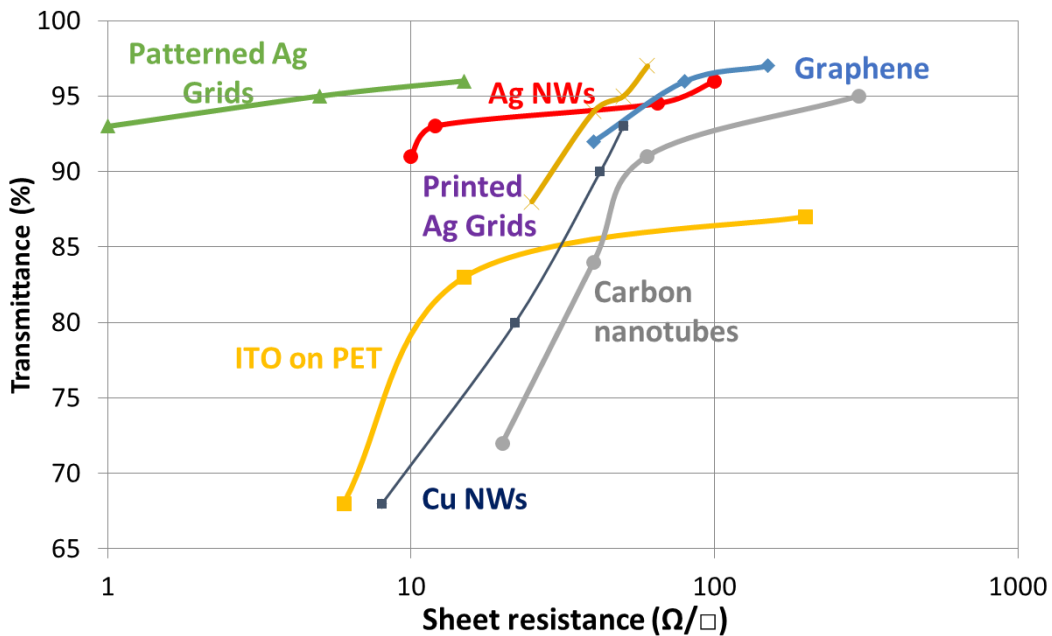


Figure 2.6 Transparency (at 550 nm) versus sheet resistance for several transparent electrode materials. The data for the silver nanowire electrodes are from my own experiments and the remainder of the data in the plot is from [59–61].

Table 2.1 Comparison of alternative transparent electrode material properties.

| Material           | Transmittance range at 550 nm (%) | Sheet resistance range (ohms/sq) | Pros                                                                                                     | Cons                                          |
|--------------------|-----------------------------------|----------------------------------|----------------------------------------------------------------------------------------------------------|-----------------------------------------------|
| Carbon Nanotubes   | 73-95                             | 20-500                           | Easy fabrication, low cost, flexibility                                                                  | Low transmittance and high sheet resistance   |
| Graphene           | 92-97                             | 50-200                           | High transmittance, flexibility                                                                          | High sheet resistance, expensive fabrication  |
| Cu NWs             | 68-93                             | 9-50                             | Low sheet resistance, high transmittance, easy fabrication, low cost                                     | Unstable in air, rough surface, poor adhesion |
| Ag NW              | 92-96                             | 10-100                           | Low sheet resistance, high transmittance, flexibility, easy fabrication, low cost                        | Rough surface, poor adhesion                  |
| Patterned Ag grids | 93-96                             | 2-20                             | Very low sheet resistance, high transmittance                                                            | Complex and expensive fabrication process     |
| Printed Ag grids   | 87-97                             | 30-70                            | Highly controllable process, sufficient transmittance and sheet resistance                               | High cost compared to other alternatives      |
| ITO                | 68-87                             | 8-300                            | Low surface roughness, controllable thickness and uniform film, high transmittance, low sheet resistance | High cost, brittle                            |

# Chapter 3

## Minimizing surface roughness of the electrodes

A simple method of minimizing the surface roughness of the electrodes is presented in this chapter. Hot rollers are used to simultaneously soften plastic substrates with heat and mechanically press the nanowires into the substrate surface, which both decreases the surface roughness and increases the adhesion of the nanowires to the substrate. Much of the results of this chapter were published in the journal “Nanoscale Research Letters” in June 2014 [52].

### 3.1 Introduction

The rough surface of nanowire electrodes is a serious challenge for their integration into thin film electronics where the thickness of the film between the electrodes is less than a few hundred nanometers. In addition, the weak adhesion of the nanowires to their substrate is an issue that makes difficulties in their handling and make them sensitive to scratches, rubbing and shear stresses.

Several papers in the literature have addressed the roughness and adhesion issues of nanowire electrodes. Solutions fall into three general categories. The first involves using a transparent conductive material to fill the spaces between the nanowires [34,38,62–64]. Gaynor *et al.* pressed silver nanowires into a layer of the transparent conductive polymer (PEDOT:PSS) to decrease the root-mean-square (RMS) surface roughness to 12 nm and maximum peak-to-valley values to around 30 nm [63]. Choi *et al.* instead deposited the PEDOT:PSS layer on top of the nanowire film

to achieve an RMS roughness of 52 nm<sup>[34]</sup>. Chung *et al.* alternatively used ITO nanoparticles to fill the spaces between the wires and reduced the RMS roughness to 13 nm and the maximum peak-to-valley to below 30 nm. In the latter paper, polyvinyl alcohol (PVA) was also added to the ITO nanoparticle solution to increase the adhesion of the nanoparticle/ nanowire film to the substrate<sup>[64]</sup>. The downside of all these approaches is that to significantly reduce surface roughness, the required thickness of the conductive material needs to be at least 3 times the diameter of the nanowires. At these thicknesses there is a reduction in the electrode transparency and consequently the efficiency of the devices due to the limited transparency of the conductive materials<sup>[38]</sup>.

The second category to reduce roughness is to deposit a transparent but non-conductive polymer on top of the nanowire film<sup>[41,65–67]</sup>. This allows a material that is more transparent than PEDOT:PSS or ITO to be used. Using an optical adhesive in this manner, Miller *et al.* reduced the RMS roughness of silver nanowire films to 8 nm and there was only a 2% change in sheet resistance after an adhesion test<sup>[41]</sup>. Zeng *et al.* buried silver nanowires in PVA to reduce the surface RMS to below 5 nm and increase adhesion of the nanowires to the substrate<sup>[67]</sup>. However, because the polymers used are not conductive, in all these studies the nanowire/polymer composite must be peeled off the original substrate to expose the conductive nanowire-mesh surface, which adds a complex manufacturing step. Although not reported in the literature (to our knowledge), the nanowire film could instead be pressed into a transparent non-conductive polymer, to avoid the peeling step. This technique however would still be less than ideal as an extra polymer layer would still add manufacturing complexity and some devices may not be compatible with the polymer used.

The third category to reduce nanowire electrode roughness is to avoid using an additional polymer and instead press the nanowires into the plastic substrate itself (usually polyethylene terephthalate, PET)<sup>[18,68]</sup>. Tokuno *et al.* mechanically pressed silver nanowire films on PET at room temperature<sup>[18]</sup>. The resulting RMS surface roughness was 18 nm, which is still quite high. Hauger *et al.* added to this process by applying heat during pressing to soften the PET substrate<sup>[68]</sup>. In this latter paper, silver nanowire films on PET were placed face-down on a 165 °C stainless steel sheet, and then a rod was rolled over the backside of the substrate. This temperature is very high for most fabrication processes and is sensitive to the speed of the rolling. Longer exposure of the nanowires to high temperature can lead to deficiencies in the electrode after rolling. The resulting RMS surface roughness of the rolled electrodes was 27 nm, which is not as smooth as what other methods were able to achieve. After an adhesion test, which was done by applying and then peeling off a piece of scotch tape, the sheet resistance of the electrodes increased more than four times. This level of adhesion is not acceptable for commercial applications. Furthermore, the high temperature used is not compatible with most plastic substrates, and the maximum peak-to-valley values, which are more important than RMS values in regards to electrical shorts or shunting, were not reported.

The above proposed methods are either not cost effective, make the fabrication process more complex, or the final surface roughness is not sufficient for thin film applications. I developed a simple method of minimizing surface roughness of the electrodes which is compatible with roll-to-roll processes and also provides sufficiently low surface roughness. Compared to the similar study<sup>[68]</sup>, the proposed method was done at a lower temperature, which is suitable for industrial processes, and lower surface roughness and higher adhesion was achieved.

### **3.2 Experimental**

Silver nanowires dispersed in ethanol were purchased from Blue Nano Inc., Charlotte, North Carolina, with an average diameter of 35 nm and an average length of 15  $\mu\text{m}$ . Heat stabilized PET film with a thickness of 127  $\mu\text{m}$  was purchased from Dupont Tianjin Inc. The PET film had an RMS roughness of 2 nm. Films of silver nanowires were deposited uniformly on 5 cm x 5 cm PET substrates using the Mayer rod coating technique <sup>[7,15,69]</sup> and then rinsed with acetone to remove the polyvinylpyrrolidone (PVP) layer on the nanowire surfaces which was left over from the nanowire synthesis process. In this method, hot-rollers are used to apply heat and mechanical pressure at the same time on the silver nanowires electrodes on PET. Pressing was done with a hot-rolling press (MSK-HRP-01, MTI Corporation, (Figure 3.1a). Different spacing between the two rollers were tried and 60  $\mu\text{m}$  was found to the highest spacing that make the nanowire adhere to the PET without deforming the substrate. The rolling speed of 5 mm/s allowed enough time for the substrate to heat up and soften during rolling. Figure 3.1b shows the schematic of the hot-rolling process. As reference samples, some electrodes were not pressed but instead annealed in a furnace at 100 °C for 30 minutes, which is a common way of preparing silver nanowire electrodes <sup>[15,39]</sup>. To test the adhesion of silver nanowire before and after the rolling process, a scotch tape test was used which is a common method of evaluating the adhesion of nanowires to their substrate <sup>[15,69,70]</sup>. A scotch tape was applied on the samples and after pressing them on the substrate by hands the tape was peeled off slowly. The resistance across the sample was measured before and after the test using 2-probe multimeter.

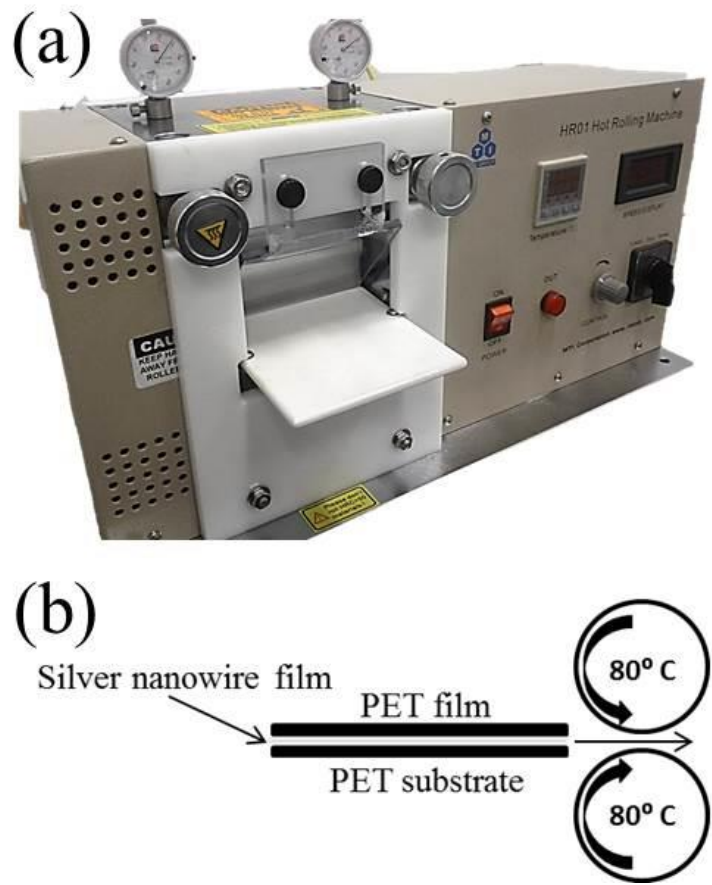


Figure 3.1 (a) Rolling machine (b) schematic of the hot-rolling process

### 3.3 Minimizing surface roughness

#### 3.3.1 Rolling process

To determine the combination of processing steps which lead to the lowest surface roughness, samples post-processed in various ways were prepared. Sheet resistance, surface roughness (RMS), peak-to-valley values and tape test results are tabulated in Table 3.1 for the various samples. The first sample (S1) was annealed at 100 °C for 30 minutes, a common post-deposition treatment for silver nanowire electrodes. Rolling silver nanowire electrodes at room temperature instead (S3) decreased the sheet resistance of the electrodes to the same extent as annealing. In addition, however, rolling the electrodes at room temperature decreased the surface roughness of the samples and increased the silver nanowire adhesion to their substrate drastically. The results

show that the annealing the samples before room temperature rolling did not have significant effect on sheet resistance and surface roughness of the samples (S2). The sample S4 was rolled at 80 °C without any protective PET layer on top of the nanowire film. Because the surfaces of the metal rollers are relatively rough, this leads to an uneven pressure which deforms the substrate and make grooves on it, as shown in Figure 3.2. When a smooth dummy PET film was placed between the nanowire film and the roller as a protective film, most of the nanowires were peeled off the substrate after removing the protective film. To solve this problem, the silver nanowires film was first rolled at room temperature. In this step the applied pressure pushed the overlapping nanowires together and the surface roughness of the electrodes was reduced to 11 nm (RMS). This indicates that the most of the nanowires have been fused together. In addition, the tape test results showed (Table 3.1) that the adhesion of the nanowire to their substrate has been improved drastically and the sheet resistance of the electrodes remained almost unchanged after the test. After stabilizing the nanowire network on their substrate in the next step the electrode was hot rolled at 80 °C with a protective PET film on top (S5). The presence of the smooth protective layer on top helps apply more uniform pressure on the film and prevent unwanted deformations and scratches on the electrodes. The heat results in the softening of the underlying plastic substrate while the mechanical pressure pushes the silver nanowires into the surface of the softened substrate. Therefore, two-step rolling, at room temperature and hot rolling, was selected as the best method to achieve the minimum surface roughness without damaging the substrate and keeping the nanowire film intact.

Table 3.1 Silver nanowire electrodes processed using various combination of methods to decrease surface roughness and improve adhesion

| Sample | Annealed | RT Rolling | Hot Rolling (80°C) | Sheet resistance (ohms/sq) | RMS (nm) | Peak-to-valley (nm) | % Rs change after tape test |
|--------|----------|------------|--------------------|----------------------------|----------|---------------------|-----------------------------|
| S1     | X        | -          | -                  | 22                         | 14       | >90                 | 510                         |
| S2     | X        | X          | -                  | 19                         | 10       | 50                  | 2                           |
| S3     | -        | X          | -                  | 22                         | 11       | 60                  | 2                           |
| S4     | -        | -          | X                  | 20                         | 10       | >100                | 20                          |
| S5     | -        | X          | X                  | 14                         | 7        | <30                 | >1                          |

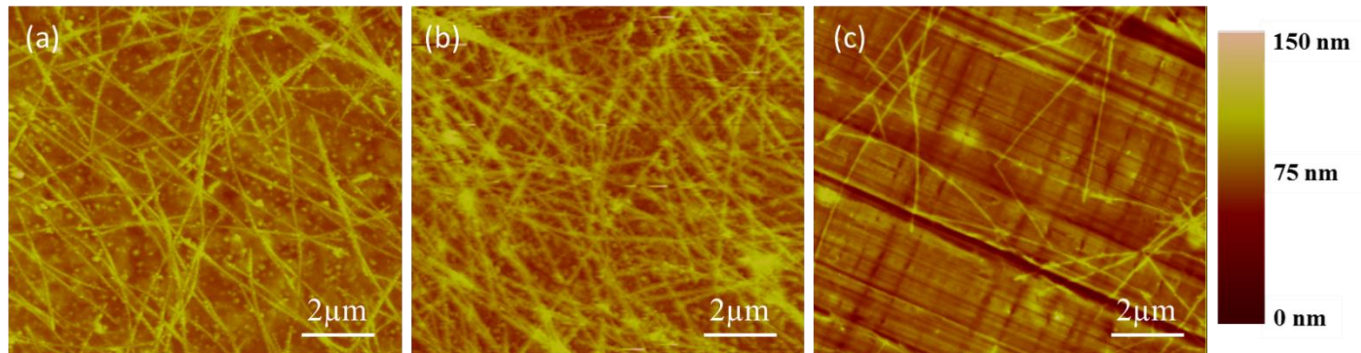


Figure 3.2 AFM images of the silver nanowire electrode (a) annealed and then rolled at room temperature (S2), (b) rolled only at room temperature (S4), and (c) hot rolled at 80 °C (S4).

### 3.3.2 Rolling temperature

Nanowire electrodes were rolled at room temperature only, and then at 60, 80, and 100 °C after a first room temperature press to find the optimum rolling temperature. The rolling temperature needs to be high enough to soften the plastic substrate so that the nanowires can be embedded into the surface of the PET. As shown in Table 3.2, rolling at 60 °C led to similar surface roughness

compared to room temperature rolling only. The rolling temperature of 80 °C was the optimum temperature that led to minimum surface roughness which is near the glass transition temperature of the PET films (75-80 °C). At this temperature the tensile modulus of the PET drops and the film become softer. Increasing the temperature above the glass transition temperature made the substrate too soft and led to permanent deformation. The surface roughness of the hot-rolled samples at 100 °C increased compared to rolling at 80 °C, since the substrate was deformed. These results show that hot-rolling plastic substrates around their glass transition temperature is the most effective temperature for embedding nanowires, and should be able to be applied to other plastic substrates.

Table 3.2 Rolling silver nanowire electrodes at different temperatures. The rms roughness of these samples was 14 nm before rolling.

| <b>Rolling temperature</b> | <b>RMS (nm)</b> |
|----------------------------|-----------------|
| <b>RT</b>                  | 9               |
| <b>60°C</b>                | 8.5             |
| <b>80°C</b>                | 7               |
| <b>100°C</b>               | 10              |

### **3.3.3 Hot rolling vs annealing results**

Figure 3.3 shows SEM images of an unpressed, annealed reference sample and a hot-rolled electrode. It can be seen that the hot-rolled nanowires are pushed into the substrate with the nanowires remaining at the surface so that they can contact a device layer above it. The annealed electrode had a sheet resistance of 22 Ω/sq with a specular transparency of 93% at 550 nm, while

the hot-rolled electrode with the same density of nanowires had a sheet resistance of  $14 \Omega/\text{sq}$ , with 91% transmittance. Figure 3.3b indicates that hot-rolling fuses overlapping wires into each other; it appears that the nanowire junctions in the image have been flattened and the AFM results (Fig 3.4d) confirms that the height of a junction of five nanowires has been reduced to the height of a single nanowire. This process lowers the resistance of the nanowire junctions and explains the 35% lower sheet resistance of the hot-rolled electrodes. In contrast, the junctions on the annealed sample are not completely welded; an annealing temperature higher than  $100^\circ\text{C}$  cannot be used because of the plastic substrate. The hot-rolling process did not have a significant effect on the mechanical properties of the film and the orientation of the nanowires stayed the same after the process. The transparency of the hot-rolled electrode was slightly lower than that of the annealed one, which may be due to the slight flattening of the nanowires. However, the embedded nanowires in the substrate are not expected to change the optical properties of the film significantly. The sheet resistance and transparency of the hot-rolled electrodes match those of ITO electrodes on glass substrates<sup>[71]</sup> and are superior to ITO-coated plastic<sup>[72–74]</sup>.

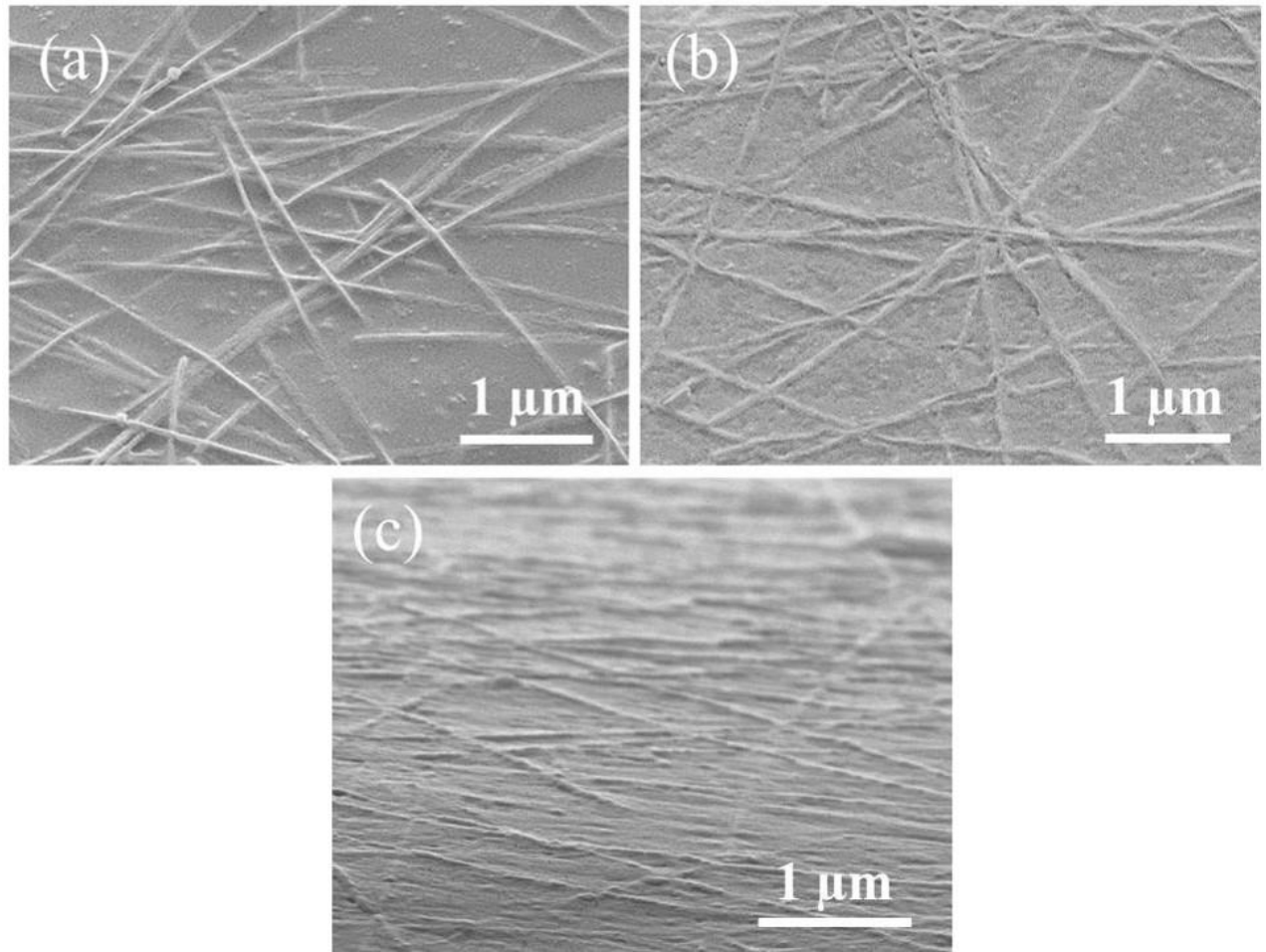


Figure 3.3 SEM images of tilted ( $45^0$ ) silver nanowire films on PET after (a) annealing and (b) hot-rolling. (c) SEM image of a tilted ( $85^0$ ) hot-rolled electrode, which shows that the nanowires are embedded in the substrate surface.

Atomic force microscopy (AFM) was used to measure surface roughness and peak-to-valley values were extracted from line scan data collected by Gwiddion software. Figure 3.3 shows the AFM images of an annealed electrode and a hot-rolled electrode, with representative line scans underneath. The surface roughness of the hot-rolled electrodes dropped 50 percent compared to that of the annealed sample to 7 nm, and the maximum peak-to-valley height was reduced to less than 30 nm. In addition, the line scan results show (Fig 3.4d) that the height of a single nanowire was reduced to 8-16 nm which shows that the nanowires have been embedded more than half of

their diameter into their substrate. In general, it can be concluded that the hot-rolling process can embed the nanowire into their substrate down to three quarters of their diameter. Furthermore, the glass transition temperature is the highest rolling temperature that the substrate can tolerate without major deformation and the lowest surface roughness was achieved at this point. Therefore, the glass transition temperature is considered as the highest temperature that this process can be done.

These roughness values are lowest among electrodes which do not use additional material to fill the spaces between the nanowires, and comparable to those that do. Furthermore, for a given sheet resistance, the hot-rolled electrodes are more transparent than electrodes that use additional material [63,65]. The maximum peak-to-valley value of the hot-rolled electrodes is lower than the typical layer thicknesses in organic electronic devices.

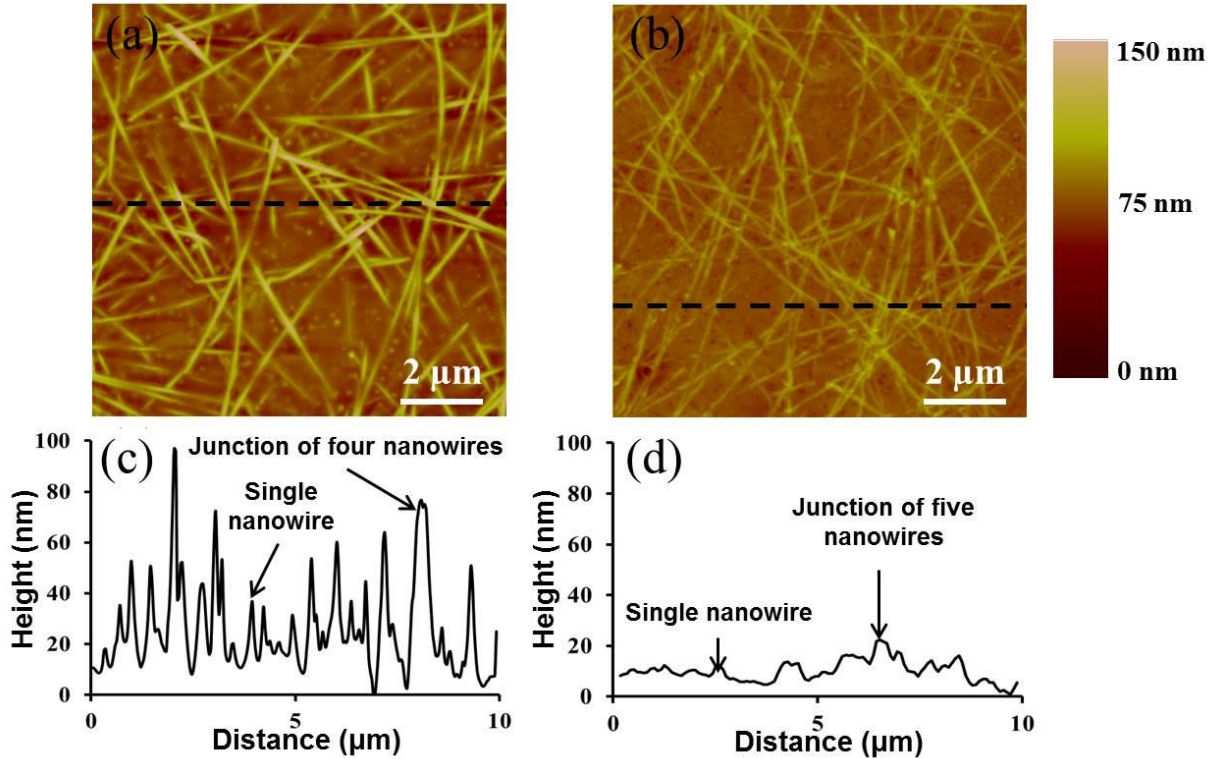


Figure 3.4 AFM images of silver nanowire electrodes on PET after (a) annealing (S1) and (b) hot-rolling (S5). (c), (d) Line scan data corresponding to the black dashed lines in (a) and (b), respectively.

Because different groups use different nanowire diameters for their electrodes, samples were also fabricated from 90 nm diameter silver nanowires for comparison. The RMS roughness of the annealed 90 nm diameter nanowire electrodes was 40 nm, and was 10 nm in the hot-rolled samples. The maximum peak-to-valley height values were 150 nm and 50 nm for the annealed and hot-rolled electrodes, respectively.

To determine the level of adhesion, a piece of scotch tape was applied on the silver nanowire film, pressed with a finger, and then peeled off, with the sheet resistance of the electrode being measured before and after. The results of the scotch tape test are tabulated in Table 3.1. The data indicate that, unlike as-deposited and annealed substrates, the nanowires in the hot-rolled electrode adhere to the substrate very well. The sheet resistance of the hot-rolled electrode was 14.0  $\Omega/\text{sq}$  and 14.1  $\Omega/\text{sq}$  before and after applying and removing the tape. This level of nanowire adhesion greatly

exceeds other nanowire electrodes that were mechanically pressed [15,68]. One of the advantage of the rolling process is that the surfaces of the nanowires are not covered. Therefore, the nanowires can be subjected to surface treatments such as plasma and UV-ozone for functionalizing the surface. Other treatments such as etching can remove the nanowires from the substrate which could be useful for patterning purposes.

While the nanowire electrode was bent around a 5 mm radius rod by hand, the sheet resistance of hot-rolled electrodes increased by less than 1%. The resistance changes were measured during the test by a 2-probe multimeter. When bent one hundred times and then returned flat, the resistance was unchanged. In comparison, the sheet resistance of annealed electrodes increased by 3% when bent, and 2% after one hundred bending cycles. Thus, the hot-rolled electrodes had slightly better flexibility, perhaps due to the better attachment of the nanowires to the substrate.

### **3.4 Conclusion**

In summary, this study demonstrates a hot-rolling process to achieve silver nanowire transparent electrodes with a smooth surface topology and excellent nanowire adhesion to the substrate. An RMS surface roughness of 7 nm was achieved, with a maximum peak-to-valley height of 30 nm. These values meet the smoothness requirements needed for most organic devices. The silver nanowires were successfully embedded in the substrate such that their sheet resistance changed less than 1% after the tape test. The results of this project show that the surface roughness issue for nanowire electrodes can be easily addressed in a roll-to-roll compatible process without using any additional materials.

# **Chapter 4**

## **The Joule heating problem in silver nanowire electrodes**

Silver nanowire transparent electrodes have shown considerable potential to replace conventional transparent conductive materials, especially in flexible electronics. However, nanowire electrodes have a unique Joule heating problem. Unlike in a continuous film, the temperature profile is very non-uniform, with some individual nanowires reaching temperatures higher than 250 °C at the current densities incurred in organic solar cells. These hotspots accelerate nanowire degradation and lead to electrode failure. Passivating the nanowire network with a layer of reduced graphene oxide extends electrode lifetimes by slowing nanowire degradation and creating a more uniform surface temperature. However, the graphene layer does not significantly reduce the current flowing through the nanowires and so Joule heating is not prevented. The high temperatures that some individual nanowires reach ultimately melt the substrate and create electrical discontinuities. In this chapter, surface temperature mapping, lifetime testing under current flow, imaging after electrode failure, and modelling illuminate the behavior of nanowires under extended current flow and leads to recommendations to manage Joule heating.

This study was done in collaboration with three research groups from the University of Waterloo and University of Bordeaux. Luzhu Xu (from Prof. Michael Pope's research group at the University of Waterloo) participated in design of this study, and deposited and characterized the graphene oxide layer. Alireza Khosropour (from Prof. Andrei Sazonov's research group at the University of Waterloo) helped to develop nanowires' network model. Alexandra Madeira (jointly

supervised by Prof. Goldthorpe and Profs. Mona Tréguer-Delapierre and Laurent Servant at the University of Bordeaux) along with Marta Romano and Christophe Pradére at the University of Bordeaux collected the IR images and helped analyzed this data. I participated in the design of this study, fabricated the silver nanowire electrodes, tested and characterized the electrodes, analyzed the results, and extracted the current distribution in nanowire networks.

## 4.1 Introduction

Silver nanowire transparent electrodes have emerged as an alternative material to conventional transparent conductive oxides. They can exhibit similar conductivity and transparency as indium tin oxide (ITO) films,<sup>[75]</sup> the most common transparent conductive material, while being lower in cost. Furthermore, nanowire electrodes have the advantages of being deposited on substrates using low temperature solution deposition methods and are able to maintain their conductivity after repeated bending. These aspects make them particularly desirable for use on plastic substrates for flexible electronics, for which ITO is inappropriate.

Silver nanowire (AgNW) transparent electrodes are already being used in commercial touchscreen applications. These touchscreens work by creating and changing an electric field between the nanowire electrode and a parallel electrode, with a material in between that responds to the field. A current flows across the nanowire electrode only for a short time to change its potential during switching, with minimal current flowing otherwise. This is also true for other capacitive-type devices such as smart windows.<sup>[76]</sup> However, for devices such as solar cells, organic light emitting diodes (OLEDs), and transparent heaters, there are long periods of time when current continuously flows across the transparent electrode during device operation, resulting in Joule heating. Although not typically problematic for ITO electrodes, we have previously shown that the Joule heating

created at the current levels typically encountered in organic solar cells causes nanowire electrodes to fail in a matter of days. The nanowires breakup and electrical discontinuities form.<sup>[77]</sup>

Multiple mechanisms can lead to silver nanowire degradation. Silver nanowires corrode in air, specifically due to the presence of trace amounts of sulfur<sup>[78]</sup>, and this corrosion is accelerated by increasing temperature<sup>[79]</sup>. Additionally, silver nanowires are not morphologically stable owing, in part, to their high surface-area-to-volume ratio. They tend to break into small segments, a behavior usually as attributed to the Rayleigh instability<sup>[80–82]</sup>. Like corrosion, this instability of metal nanowires is also worsened at higher temperatures<sup>[82]</sup>. To slow nanowires degradation and thus increase the lifetime of AgNW electrodes, various passivation strategies have been developed that use an outer layer to protect the silver nanowires from corrosion and other side reactions with the environment. The passivation layer must be optically transparent and electrically conductive if it stands, for example, between the nanowire film and the active part of a solar cell. Passivation materials such as zinc oxide (ZnO), titanium oxide (TiO<sub>2</sub>), and graphene have been used<sup>[83–86]</sup>. Reduced graphene oxide (RGO), in particular, is attractive since it can block both moisture and the gases in air<sup>[87]</sup>. Furthermore, it can be deposited in thinner layers than ZnO and TiO<sub>2</sub> which allows it to be more transparent, and like AgNW films, it can be deposited in solution and is mechanically flexible. Several studies have shown its utility as a passivation layer<sup>[49,85,88–90]</sup>. For instance, whereas the sheet resistance of an unpassivated AgNW electrode more than tripled in less than a week at 70 °C in air, the resistance of a nanowire electrode passivated with a solution-deposited reduced graphene layer increased by less than 50% over the same time<sup>[91]</sup>. If the layer of graphene is instead deposited using chemical vapor deposition (CVD), it can more effectively stabilize the silver nanowires. A recent experiment showed only a 10% increase of sheet resistance after one month at 70 °C<sup>[92]</sup>. However, at this time this latter method is not economical for

commercial manufacturing, especially since the graphene layer cannot be directly synthesized on the nanowires but rather needs to be deposited elsewhere and then transferred.

In the above studies, degradation of a silver nanowire electrode was evaluated either at room temperature or when the electrode was annealed in an oven (or on a hotplate) to achieve an elevated temperature. In all cases, the temperature was the same at all points on the electrode. However, the surface temperature profile across a nanowire electrode is not uniform when it is used in a solar cell or OLED. Unlike in a continuous conducting film like ITO where current flows throughout the entire area of the film, in nanowire electrodes current only flows through the thin metal pathways. Furthermore, there are variations in the nanowire density across the film and thus the current density flowing in some nanowire pathways is higher than in others. These factors together result in a non-uniform temperature distribution with the temperature of some individual nanowires being significantly higher than the average surface temperature of the electrode. In this work we investigate bare AgNW electrodes and RGO-passivated AgNW electrodes under current flow. Compared to annealing, this is a more realistic situation for studying the performance and lifetime of the electrodes when they are operated in a solar cell or OLED. As other reports have shown, we confirm an RGO passivation layer does increase lifetimes by slowing nanowire degradation during an anneal, but RGO does not prevent Joule heating. It is shown that the Joule heating in RGO-passivated electrodes results in melting and deformation of the plastic substrate leading ultimately to electrode failure. These results indicate that Joule heating is a problem that cannot be overlooked and needs to be effectively addressed and managed if nanowire electrodes are to be used in devices such as solar cells, OLEDs, and transparent heaters.

## **4.2 Experimental**

### **4.2.1 Nanowire electrode fabrication**

Silver nanowires dispersed in ethanol were purchased from Blue Nano Inc. (Charlotte, NC) with an average diameter and length of 90 nm and 25  $\mu\text{m}$ , respectively. Polyethylene terephthalate (PET) films (127  $\mu\text{m}$  thick from Dupont Tianjin Inc.) were cleaned in a sonication bath of acetone, isopropanol alcohol, and distilled water each for 1 minute, then dried with nitrogen gas. The nanowires were deposited on the PET films using the Mayer rod coating technique to obtain a random network of silver nanowires. The active area of the AgNW film was 2 cm x 2 cm with two strips of 0.5 cm wide copper tape beyond the two ends as current collectors. The concentration of the nanowires in ethanol and the number of coating layers were designed to obtain AgNW electrodes with a sheet resistance of  $60 \pm 10\%$  ohms/sq ( $\Omega/\square$ ). The deposited films were dried in air for 5 minutes and mechanically pressed by rollers at room temperature to reduce the nanowire junction resistances<sup>[52]</sup>. The rolling was done to reduce the resistance of the nanowire films at the nanowire junctions by fusing them together. This step also increased the adhesion of the nanowires to the substrate which was required for the RGO deposition process. The hot rolling process was not used for this study (described in chapter 3) to avoid any possible deformation in the nanowire structure. This also enables better observation of changes in nanowire structure before and after the Joule heating experiments since nanowires are not embedded into their substrate. For comparison purposes, ITO film on PET with a sheet resistance of 60 ohms/sq was purchased from Sigma Aldrich.

### **4.2.2 Determining current flow value**

Figure 4.1a shows the structure of an organic solar cell that is commonly used in large-scale modules. The current density assumed in this study was 20 mA/cm<sup>2</sup>, which is the operating current

of the best performing organic solar cells in the literature [93,94]. Current densities in OLEDs can also reach as high as  $20 \text{ mA/cm}^2$  [95]. Figure 4.1b schematically shows charge carrier flow in the nanowire electrode when the device is operating. The current density in the transparent electrode is lowest at the right end, but increases towards the left as more generated carriers are collected. The maximum current is incurred near the left current collector bar. In common designs of organic solar cell modules, the length of the active layer is around 1 cm [96–98]. Therefore, with a current density of  $20 \text{ mA/cm}^2$ , the current at the current collector bar will reach  $20 \text{ mA}$  per centimeter length ( $\text{mA/cm}$ ) of metal bar. As this is the typical maximum current incurred in the transparent electrode, we will focus on this value in our experiments.

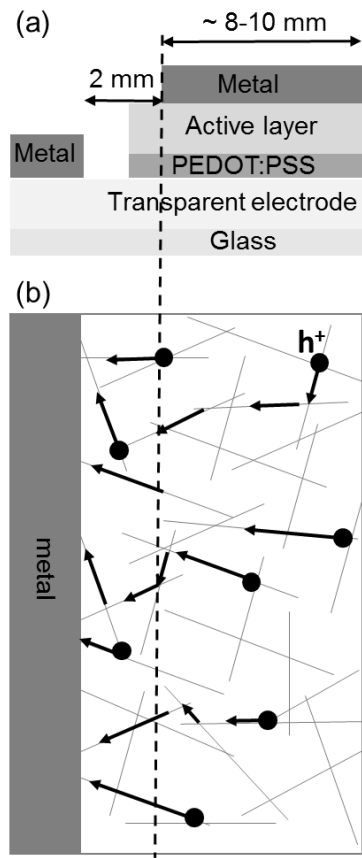


Figure 4.1 (a) Schematic of a typical organic solar cell module. (b) Planar view of the transparent electrode.

#### 4.2.3 Reduced graphene oxide passivation layer fabrication

##### 4.2.3.1 Graphene oxide synthesis

Graphene oxide (GO) was prepared using the Tour method<sup>[99]</sup>. In a typical reaction, 3 g of graphite, 360 mL of H<sub>2</sub>SO<sub>4</sub>, and 40 mL of H<sub>3</sub>PO<sub>4</sub> were first stirred together in a flask. Then, 18 g KMnO<sub>4</sub> was slowly added. The temperature of the mixture was maintained at 40 °C. After stirring for 16 h, the mixture was cooled to room temperature. Finally, the mixture was transferred into a large beaker filled with 400 g of ice, followed by the slow addition of 3 mL of 30% H<sub>2</sub>O<sub>2</sub>. The color of the solution turned from dark brown to gold. The resulting mixture was separated from the residual acids by centrifugation. The pellet was redispersed with 30% HCl and centrifuged

again. This process was repeated once more, followed by four washes with ethanol to remove the HCl. The resulting GO slurry was stored in ethanol.

#### **4.2.3.2 Graphene oxide monolayer formation**

A glass trough with Teflon coated walls and barriers was used to carry out monolayer fabrication by a modified Langmuir-Blodgett (LB) trough technique [100]. The trough was first cleaned with 1,2-dichloroethane (DCE), rinsed with deionized water (Milli-Q) and then filled with water until the water surface emerged just passed the trough walls. The cleanliness of the trough was verified by using a paper Wilhelmy plate and balance which was used to measure the surface tension of water as 72 mN/m. The as-prepared AgNW film coated PET samples were placed beneath the water prior to GO deposition. The GO dispersion in ethanol was mixed with DCE to make a final GO concentration of 0.025 mg/ml with a volume ratio of ethanol/DCE of 1:13. This GO suspension was dripped onto the air-water interface until the solvent could no longer spread. We have recently shown that this method results in continuous, densely tiled, monolayer films of GO over the entire trough surface and removes the need to compress the film with the floating barriers of a typical LB trough. The floating GO film was deposited onto PET samples by the horizontal precipitation method which involves slowly draining out the water from the trough, such that the film is lowered onto the substrate. In addition to coating PET samples, mica and highly oriented pyrolytic graphite (HOPG) substrates were coated at the same time to verify film morphology and coverage by atomic force microscopy (AFM) and scanning electron microscopy (SEM).

#### **4.2.3.3 Chemical reduction of graphene oxide monolayers**

The as-prepared GO monolayer-coated PET samples were dried in a vacuum oven at 60 °C for 1 h to remove adsorbed water. A 50 mM solution of NaBH<sub>4</sub> in water (pH adjusted to 10 using NaOH)

was heated to 50 °C [101]. Coated samples were immersed in this solution for 15 min, followed by rinsing with DI water. The resulting chemically reduced films were dried in vacuum oven at 60 °C for 1 h.

#### **4.2.4 Characterization**

Contact mode AFM was carried out on GO films deposited on atomically flat muscovite mica (SPI) substrates using NP-STT10 tips (Bruker) and a Nanoscope MultiMode AFM (Veeco). AFM images were analyzed using Gwyddion software to extract height profiles between the atomically smooth substrate and the GO sheets, and a custom MATLAB code was used to estimate sheet thicknesses from the steps in the height profiles.

The sheet resistance of the electrodes with and without the RGO layer was measured by either a multimeter or a 4-point probe measurement system. UV-Vis photospectroscopy with an integrating sphere was used to measure the transparency of the electrodes. Scanning electron microscopy (SEM) images were taken before and after failure of the electrodes

A DC power supply was connected to the current collectors to apply a constant current of 20 mA/cm across the bare electrodes. A multimeter and a flat leaf-style thermocouple were used to continuously monitor the voltage across the electrode and its average surface temperature, respectively, during extended time experiments and PC link software was used to record the data. In a separate measurement, an infrared (IR) camera was used to map the spatial temperature distribution over the electrode area while the electrode was conducting 20 mA/cm of current. The IR camera (FLIR SC7000) had an indium-antimony detector composed of a focal plane array featuring 81,920 pixels (matrix 320 x 256), and a simultaneous measurement at all 81,920 spots can be performed using the snapshot mode. The camera was equipped with an IR lens with a focal

length of 25 mm. The resulting spatial resolution per pixel is around 250  $\mu\text{m}$ . A calibration method was used to retrieve the absolute temperature from the raw intensity profiles given by the infrared camera by using a method previously reported <sup>[102,103]</sup>. For this purpose, a thin layer of black paint was deposited over the electrodes in order to avoid reflections

#### 4.2.5 Modelling

Random networks of silver nanowires were modelled in MATLAB. The nanowires were modelled as cylinders having the same average diameter and length as the nanowires used in our experiment (90 nm and 25  $\mu\text{m}$ , respectively). The resistivity of the nanowires in the model was 27  $\text{n}\Omega\cdot\text{m}$ , which is the average resistivity reported for 90 nm silver nanowires <sup>[104–106]</sup>. The nanowires were randomly distributed over a 300  $\mu\text{m} \times 300 \mu\text{m}$  area (Figure 4.7a). The nanowires in the network were treated as resistors and the circuit was analyzed using Kirchhoff's law to determine characteristics of each nanowire, which was done using HSPICE software. An HSPICE netlist was constructed for this random nanowire network to calculate the sheet resistance of the modelled network and extract the current in individual nanowires. The density of nanowires was chosen to generate nanowire networks with sheet resistances of  $60 \pm 15\%$  ohms/sq. It should be noted that junction resistances were neglected. Our rolling process during electrode fabrication welded overlapping nanowires and greatly reduced junction resistances. It has been shown by others that in cases where steps are taken to reduce junction resistances in nanowire electrodes, junction resistance may no longer be a significant factor <sup>[107]</sup>. We found that neglecting junction resistances was an appropriate approximation since for a given density of nanowires, the sheet resistances of our modelled networks fell within  $\pm 10\%$  of our experimental samples.

The current values were subsequently used to model Joule heating in individual nanowires using COMSOL Multiphysics software. The Joule heating module in COMSOL was used to find the

local temperature of a nanowire on a PET substrate at different current densities. The Joule heating and resulting temperature of nanowires under the range of current densities on a plastic substrate (PET) with and without a RGO passivation layer was simulated. The graphene sheets are much larger than the diameter of the nanowires and cover their surface and the surrounding substrate conformably, as shown by others [108]. In the COMSOL model the conformal contact has been simplified to square shape. This shape has three points of contact with the nanowire with small gaps between the nanowire and the RGO layer which is expected to be similar to the real structure. The area of the substrate was selected according to the experimental nanowire density by dividing the area of the substrate by the number of nanowires. Heat convection was considered at the top and bottom of the PET sample and all surfaces of the nanowires and the RGO layer as the boundary condition. The steady state temperature was calculated using the Poisson heat transfer equation:

$$Q = n \cdot K \nabla T = h \Delta T$$

Where  $h$  is the heat transfer coefficient,  $K$  is the thermal conductivity of the object and  $n$  is the outward normal with a unit value of one. In the COMSOL model, the heat transfer coefficient ( $h$ ) was taken to 5 W/(m<sup>2</sup>·K) which is the recommended value for the heat transfer coefficient of air by COMSOL. For determining electric potential, one end of each nanowire was grounded and the other end considered as the current terminal. In the heat transfer model, the values of the heat transfer coefficient and the thermal conductivity do not significantly affect the final average steady state temperature. However, the thermal conductivity value has a significant role in the heat distribution profile on the samples. It will be shown later that presence of a graphene layer with high thermal conductivity can lead to more uniform distribution of heat on the surface of the samples. The exposed area of the PET affects the steady state temperature due to the change in the available area for heat transfer.

## **4.3 Results and Discussion**

### **4.3.1 Characterization of electrodes**

Our first goal was to create a transparent barrier film of RGO to protect the Ag nanowires as illustrated schematically in Figure 4.2a. The morphology and coverage of the GO film are shown in the SEM and AFM images in Figures 4.2b and 4.2c, respectively. The contrast in the SEM image (Figure 4.2b) shows the GO film (bright) and underlying HOPG substrate (dark) and indicates that film is composed of densely tiled and partially overlapping (even brighter contrast regions) sheets. The film coverage, estimated by pixel counting, is over 95%. The AFM images of films deposited on mica (Figure 4.2c) show the same coverage. A histogram generated by analyzing AFM thickness profiles of over 200 sheets is shown in Figure 4.2d and indicates that the tiled sheets have a narrow distribution of thicknesses with an average around 0.7 nm. This indicates that the film is composed almost entirely of single layers. It was challenging to verify the film morphology and coverage on PET directly because the substrate roughness is larger than the expected film thickness and the secondary electron contrast difference between PET and RGO is poor. However, the fact that we could achieve similar morphologies on both hydrophilic (mica) and hydrophobic (HOPG) substrates suggests that our film coverage and thickness should be very similar on PET.

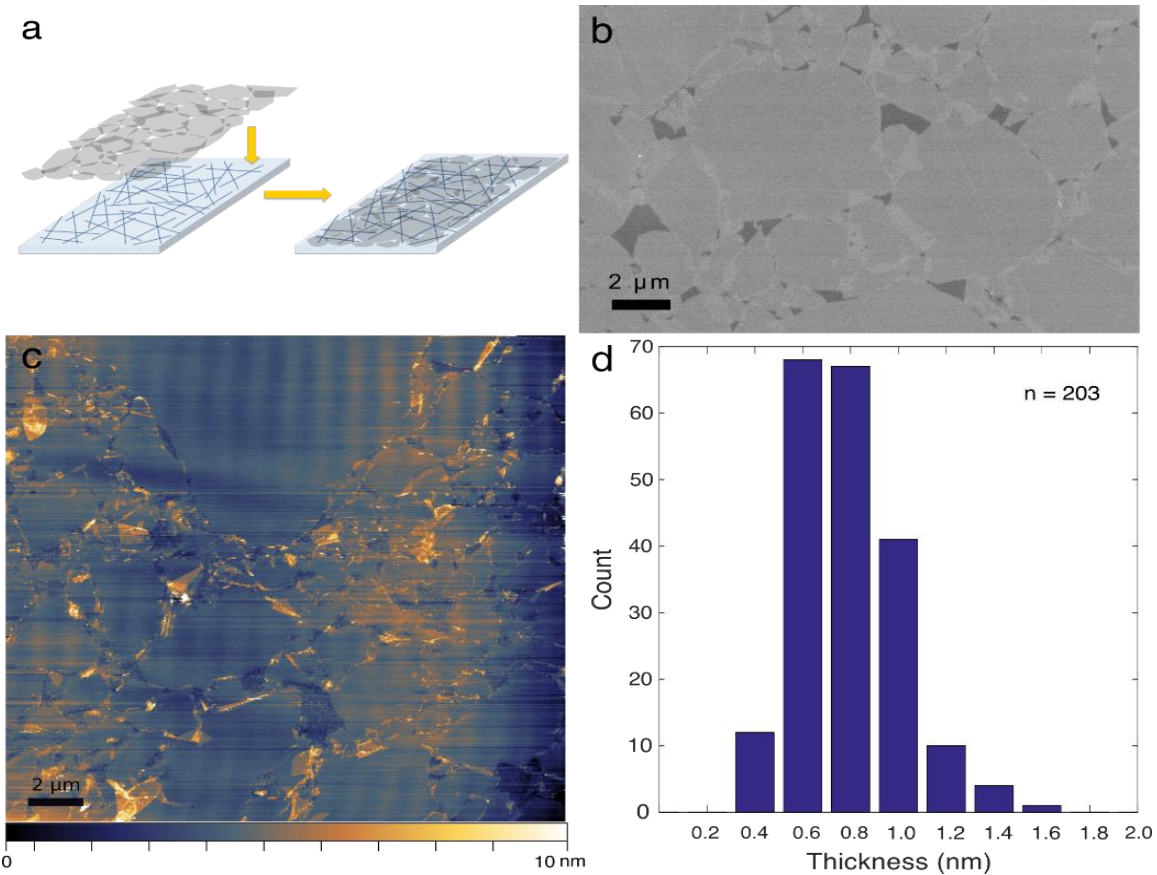


Figure 4.2 Graphene oxide blocking layers. (a) Schematic illustrating GO monolayer deposition on AgNW/PET film. (b) Secondary electron SEM image showing contrast between GO film (light) and some pinholes exposing the hydrophobic (HOPG) substrate (dark). (c) Contact-mode AFM image of GO film on mica. (d) Histogram of sheet thickness estimated from AFM imaging as in (c).

The transparency of the 60 ohms/sq AgNW films (i.e. not including the PET substrate) at a wavelength of 550 nm were 94%. The transmittance of the AgNW electrode dropped from 94% to 91% after the deposition of the reduced graphene oxide layer. The 3% decrease in transparency is consistent with the transparency of a single layer of graphene in the visible range which is in direct agreement with our AFM and SEM analysis of the graphene film discussed above [109]. The RGO sheets are electrically conductive. However, their conductivity is significantly less than the conductivity of the nanowires [110], and the contact resistance between two overlapping sheets is high. Therefore, the majority of the current flows through the NW network instead of the RGO

film. The overall sheet resistance of the electrode did not decrease significantly after adding the RGO layer (only by 0-10%).

#### **4.3.2 Annealing study**

We first confirmed prior studies of the literature showing the effectiveness of reduced graphene oxide in protecting the nanowire films against degradation when annealed in a furnace. Both the AgNW and AgNW-RGO electrodes were annealed at 70 °C in air for 14 days. After six days, the sheet resistance of the AgNW electrode increased by 180 times compared to the initial sheet resistance ( $R_0$ ), as shown in Figure 4.3, whereas the sheet resistance of the AgNW-RGO electrode increased by only by a factor of 1.5 after 14 days. This indicates that the RGO is quite successful in slowing silver nanowire degradation under annealing conditions, as concluded by many others. The main mechanisms by which the RGO increases the stability of the nanowires are (i) the RGO layer blocks gas molecules which results in protecting silver nanowires against corrosion, (ii) presence of the RGO layer changes the surrounding environment of the nanowire and changes the surface self-diffusion and activation energy values, as described in chapter 1, and (iii) the melting of nanowires start from their surfaces and when the RGO, which has higher melting point than silver nanowires, is in contact with the surface of the nanowire the melting of nanowire doesn't occur until higher temperatures [86]. Although RGO looks very promising in increasing the stability of the nanowires, testing its effectiveness under current flow is essential to mimic the stress on the electrode during use in solar cell or OLED.

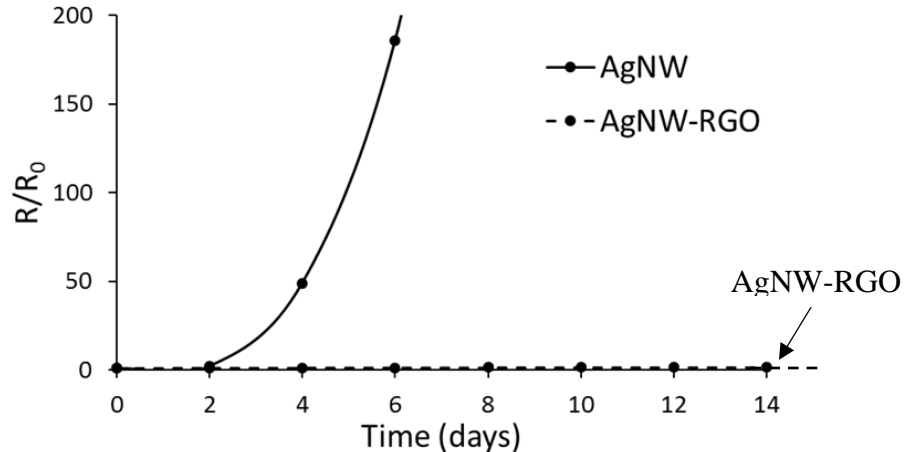


Figure 4.3 Sheet resistance changes of the nanowire and nanowire-RGO electrodes at 70 °C in air.

#### 4.3.3 Surface temperature distribution under current flow

Figure 4.4 shows the evolution of surface temperature profiles of the ITO, AgNW, and AgNW-RGO films when 20 mA/cm of DC current is passed across the electrodes. Profiles are shown after 10 s of current flow and after the temperature has stabilized (60 s). The current collectors are located at the top and bottom of the images and the current flows from top to bottom, as indicated schematically in Figure 4.4a. As can be seen, the temperature is uniform over the ITO electrode. However, temperature variations greater than 20 °C is evidenced across the AgNW electrode (Figure 4.4d-e). The presence of such hot spots in nanowire electrodes has also been reported by others [111,112]. A non-uniform density distribution of the nanowires across the electrode can be the culprit. In bottleneck regions where there is a sparser nanowire concentration, individual nanowires must sustain high current densities, and thus local Joule heating will be significantly higher than in denser nanowire regions. The hotspots observed in the unpassivated nanowire electrode exist along a line across the electrode parallel to the current collectors. We hypothesize that there are regions of sparse nanowires along this line and thus much of the current cannot re-route through denser locations. Thus Joule heating, equal to  $I^2R$  where  $I$  is current and  $R$  is

resistance, is high along this line. The existence of hot spots accelerates both corrosion and Rayleigh instability in these regions leading to nanowire breakdown. When nanowires break down, more current is forced through other available pathways, causing those regions to then increase in temperature. This situation can be observed in Figures 4.4d-f. A hotspot present after 10 s, which Figure 4.4f indicates is at the highest temperature on the electrode, no longer exists after 60 s. This suggests that some nanowires failed rapidly after current was applied due to this high temperature. As can be observed, it cooled down once no current could no longer flow through that pathway, but consequently, the regions around the failed nanowires became hotter. This in turn accelerates nanowire degradation at these points until ultimately, as we observed when higher currents were applied to accelerate failure times, an open circuit exists in a line extending across the electrode.

It is important to note that the smallest detected area (pixel resolution) of the thermal imaging camera is  $200\text{ }\mu\text{m} \times 200\text{ }\mu\text{m}$  which corresponds to an area with more than one hundred nanowires. Thus, the temperature of individual nanowires is not detectable. Modelling presented later indicates that temperature variations on the nanoscale are far higher than ones observed on the microscale in thermal maps such as these.

In Figures 4.4g-i, we can see that the graphene passivation layer smooths out the temperature variation of the NW film such that the uniformity is comparable to the ITO electrode. This is likely because of the high thermal conductivity of the RGO (above  $1000\text{ W/(m}\cdot\text{K)}$ ) compared to air ( $0.024\text{ W/(m}\cdot\text{K)}$ ) and the plastic substrate ( $0.23\text{ W/(m}\cdot\text{K)}$ ). The RGO layer not only distributes heat more evenly across the surface heat. It, but it also provides a larger surface area from which the heat can dissipate, thereby lowering the average surface temperature of the electrode.<sup>[113]</sup> The absence of hot spots is one of the reasons why we will later see that graphene extends the lifetime of AgNW electrodes under current flow.

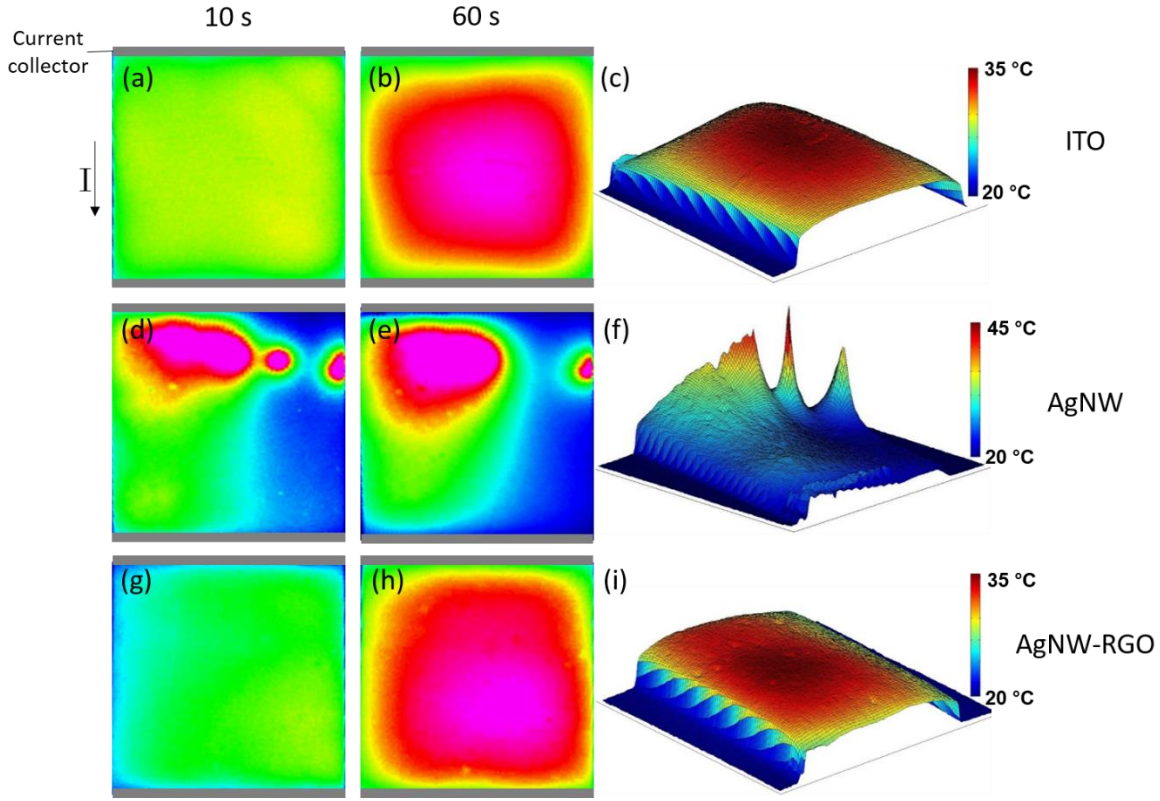


Figure 4.4 Temperature profiles of electrodes, measured using a thermal imaging camera, when 20 mA/cm of current is flowed in the direction of top to bottom. (a,b) Surface temperature of ITO, (c) 3D temperature profile of ITO after 60 s. (d,e) Surface temperature of the AgNW electrode, (f) 3D temperature profile of the AgNW electrode after 10s. (g,h) Surface temperature of the AgNW-RGO electrode, (i) 3D temperature profile of the AgNW-RGO electrode after 60 s.

#### 4.3.4 Electrode failure under current flow

Figure 4.5a shows the average surface temperature (measured with a thermocouple that was attached to the bottom of the substrate) and sheet resistance evolution for an unpassivated AgNW electrode under 20 mA/cm current density. The electrode failed after 120 h (5 days), where failure is defined as when the sheet resistance exceeded 1500 ohms/sq. SEM images of nanowires after electrode failure are shown in Figures 4.5b and c, illustrating the two different types of nanowire breakdown that was observed. In Figure 4.5b, the presence of nanoparticles on the nanowires indicate nanowire corrosion [77] which eventually lead to electrical discontinuities. Other nanowires (Figure 4.5c) are completely melted in addition to damaging the plastic substrate

underneath, implying a very high localized temperature. We postulate that these latter nanowires were subjected to very high levels of current and thus heated up and failed quickly, like those associated with the disappearing hotspot in Figures 4.4d-e, whereas the corroded nanowires were subject to lower current densities over a longer time period. These issues will be further discussed when the modelling of current levels and temperatures of individual nanowires is presented.

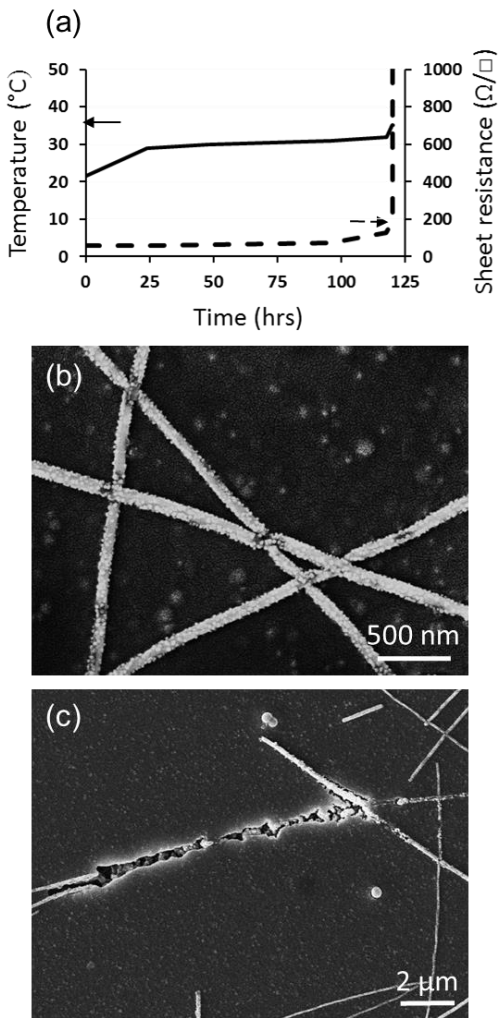


Figure 4.5 (a) Temperature and sheet resistance of a AgNW electrode over time under a current density of 20 mA/cm. (b), (c) SEM images of nanowires after electrode failure.

Figure 4.6a shows the average temperature and sheet resistance of the AgNW-RGO electrodes under a linear current of 20 mA/cm. The RGO passivation layer extended the lifetime of the AgNW

electrode to 285 hours (~12 days). There are three possible mechanisms by which RGO passivates the electrodes: (1) nanowire corrosion is slowed since the RGO impedes air from reaching the nanowires; (2) the RGO prevents hotspots (as discussed above) where the fastest degradation occurs; and (3) the RGO increases the morphological stability of the nanowires and thus increases the temperature at which the nanowires break-up [44]. Indeed, SEM images taken after electrode failure show that the RGO-passivated electrodes do not fail due to NW melting or corrosion, like in the case of unpassivated electrodes (Figure 4.6b). Rather, the electrode instead breaks down due to deformation and melting of the PET substrate on a microscale (Figure 4.6 c and d). The substrate deformation causes breakage in the nanowires and thus electrical discontinuities.

A melted substrate indicates that the local temperature of the nanowires exceeds the melting point of PET (~250 °C) during current flow. The silver nanowires, normally unstable at this temperature [37], can sustain these high temperatures due to the RGO passivation. Although the thermal imaging data indicated the RGO-passivated electrodes had an average surface temperature of 32 °C under this same current flow (Figure 4.4i), the local temperature of some nanowires are much higher. These results demonstrate the inadequacy of annealing a nanowire electrode to assess stability and lifetimes, which is the method used by many others and done above in Figure 4.3. The Joule heating that would occur in the electrode during solar cell operation, which causes very high localized temperatures, is not incurred. As measured in Figure 4.3, the resistance of the RGO-passivated electrode annealed in a furnace at 70 °C only increased by 1.5 times after 12 days, whereas under a current flow causing an average surface temperature of 32 °C, the resistance increased by more than 25 times.

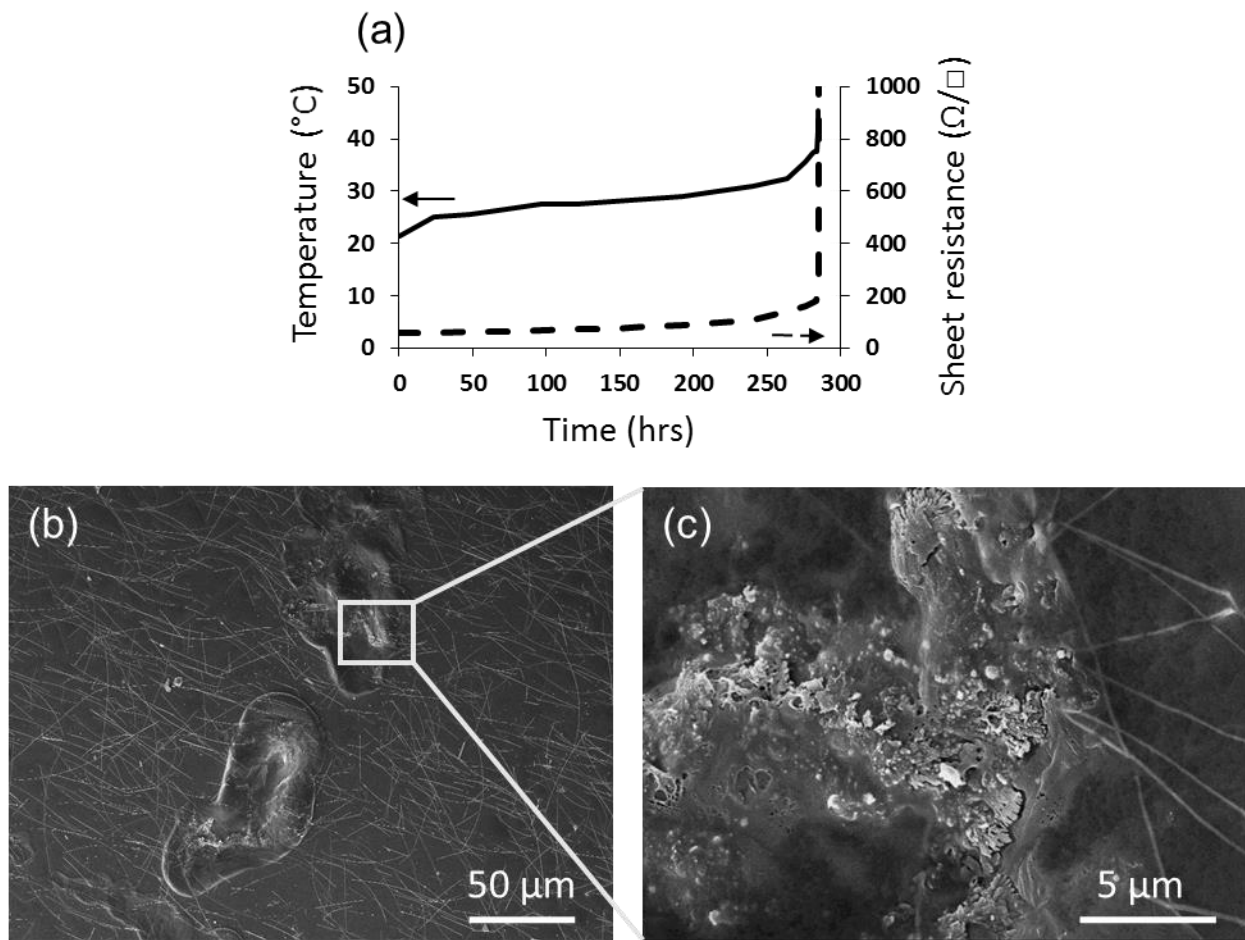


Figure 4.6 (a) Temperature and sheet resistance vs. time of a AgNW-RGO electrode under a current density of 20 mA/cm. (b), (c) SEM images of the electrode after failure indicating melting of the plastic substrate.

#### 4.3.5 Modeling of current in a nanowire network

As evidenced by SEM imaging, electrode failure occurs at the level of individual nanowires. However, measuring the temperature and the levels of current flowing through individual nanowires in an electrode is experimentally prohibitive. Therefore, modelling was employed to better understand the extent of Joule heating and the mechanisms of failure.

As described above, the silver nanowire network was modelled in MATLAB and the modelled network is shown in Figure 4.7a. The current flowing through individual nanowires in the

modelled network was analyzed using HSPICE. Figure 4.7b tabulates the current density through individual nanowire segments (segments span between two red dots in Figure 4.7a, where red dots are the locations of nanowire junctions and nanowire endpoints) when 20 mA/cm is applied across the metal end bars. This level of current does not lead to problematic current densities in continuous films, however, nanowire electrodes are not continuous and the current is instead forced through 90 nm-thick nanowire pathways, leading to very high current densities. The average current density in the nanowires is calculated to be  $1.2 \pm 0.1 \times 10^5$  A/cm<sup>2</sup>. As a comparison, for a 130 nm thick film of ITO, the approximate thickness of a 60 ohms/sq ITO film, the current density would be  $1.5 \times 10^3$  A/cm<sup>2</sup>, two orders of magnitude less.  $0.5 \pm 0.1$  % (error based on running the simulation with a different random network 5 times) of the nanowires in the electrode carry a current density of more than  $5.5 \times 10^5$  A/cm<sup>2</sup> which are expected to break down relatively fast due to Joule heating (to be discussed in the subsequent section).

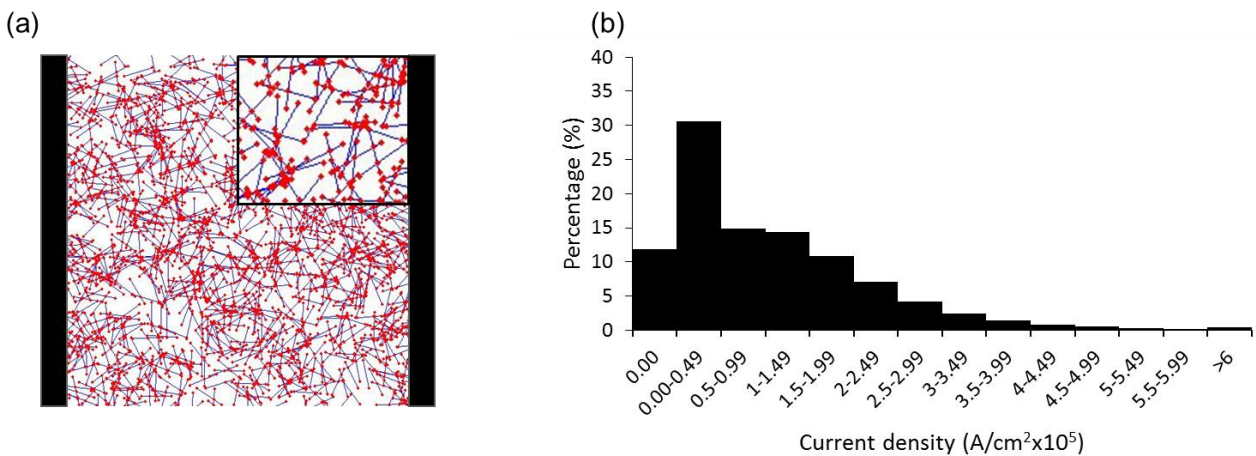


Figure 4.7 (a) Silver nanowire electrode model with a sheet resistance of 60 ohms/sq (red dots show nanowire junctions and endpoints) (b) The distribution of current densities in individual nanowire segments (i.e. between two red dots) of the nanowire electrode.

#### **4.3.6 Joule heating modelling of nanowire electrodes**

The Joule heating in a single nanowire on PET was modeled in COMSOL as described above. Figure 4.8 shows the results of the simulation and the steady state temperature for a single AgNW, AgNW-RGO and ITO samples on PET substrates. A single AgNW, with a diameter of 90 nm, carrying the average current density calculated in the section above ( $1.2 \times 10^5 \text{ A/cm}^2$ ) reached  $33^\circ\text{C}$  (Figure 4.8a) and a RGO-passivated AgNW reached  $30^\circ\text{C}$  (Figure 4.8b). The RGO helps spread out the heat due to its higher thermal conductivity compared to PET and reduces the surface temperature by 8-10 %. Our simulated results match closely to experiment: the calculated average surface temperature of the AgNW electrode under  $20 \text{ mA/cm}$  of current, recorded by the IR camera, was  $33 \pm 2^\circ\text{C}$ , and the measured temperature of the AgNW-RGO (Figure 4.4i) was  $32 \pm 2^\circ\text{C}$ . And when Joule heating was simulated in a  $60 \text{ Ohm/sq}$   $130 \text{ nm}$  thick film of ITO on PET under the calculated average current density of  $1.5 \times 10^3 \text{ A/cm}^2$  (Figure 4.8c), the steady state temperature was  $32^\circ\text{C}$ , also close to the  $34 \pm 2^\circ\text{C}$  recorded by the IR camera (Figure 4.4c).

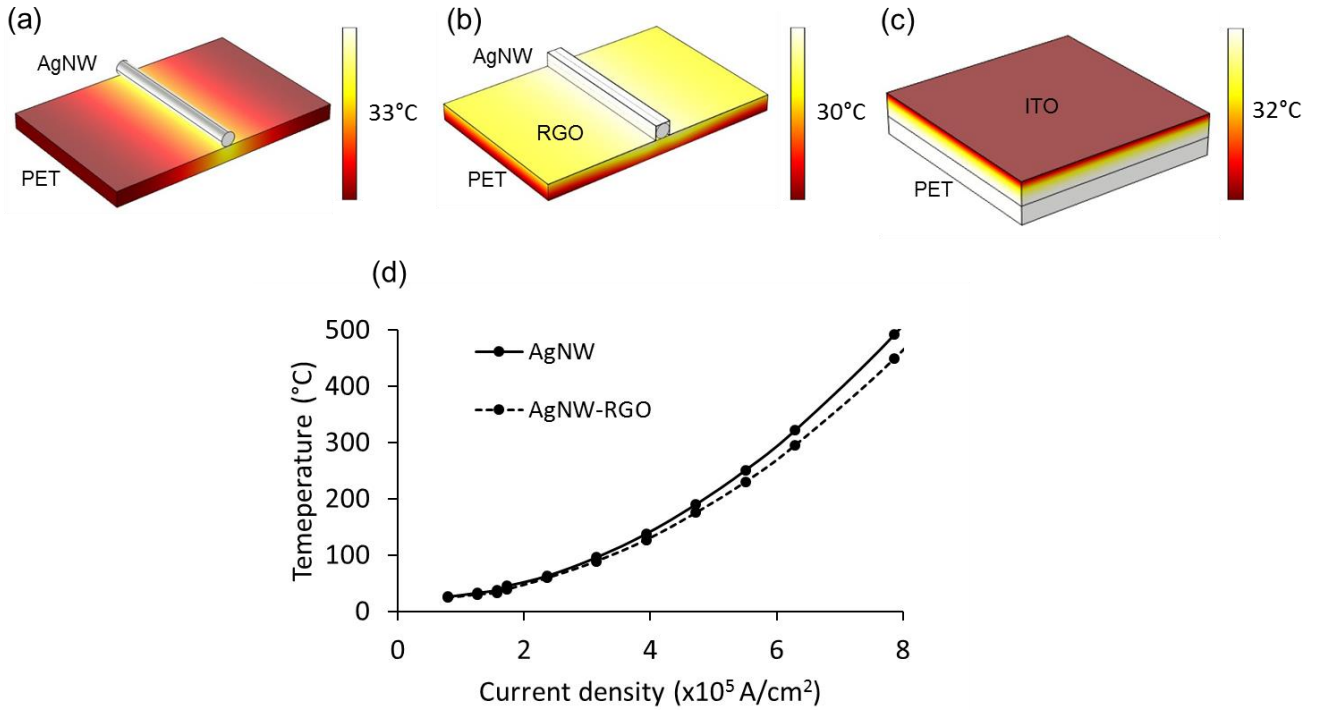


Figure 4.8 Steady state thermal profile of a (a) AgNW and (b) RGO-passivated AgNW under a current density of  $1.6 \times 10^5$  A/cm $^2$ . (c) Simulated thermal profile of ITO film on PET under the same current (d) Calculated steady state temperature of individual unpassivated and passivated silver nanowires on PET substrates under different current densities.

Although the temperature of a nanowire conducting the average current density is 33 °C, there are individual nanowire segments that become much hotter. Figure 4.8d shows the simulated temperature of silver nanowires on PET at different current densities. As calculated in the section above, 0.5 % of the nanowire segments in a 60 ohm/sq AgNW electrode under 20 mA/cm current flow are carrying a current density higher than  $5.5 \times 10^5$  A/cm $^2$ . We see in Figure 4.8d that the temperature of unpassivated NWs carrying these levels of current exceeds 250 °C, above the melting point of PET. And at this temperature, unpassivated 90 nm AgNWs are not thermally stable either [37]. Such nanowires would fail quickly after the current is applied. These nanowire segments are hotter than the hottest spot in the IR images because, as mentioned above, the camera only measures an average temperature of several hundred nanowires. However, the existence of these very hot nanowires still corroborates with our experimental results. The IR data in

Figure 4.4d and e insinuate that there is a rapid failure of some nanowires, and the SEM image in Figure 4.5c indicates melting of both the nanowire and a localized portion of the substrate. Once these high current carrying nanowires break and are no longer conductive, the current is redistributed amongst the other nanowires.

The existence of localized nanoscale hotspots of high temperatures is in stark contrast to ITO, where the current is distributed evenly throughout the film. In a film of ITO carrying the same current density as the nanowire electrode, all points on the surface would be close to 32 °C. The existence of a non-uniform temperature distribution and localized hotspots reaching 250 °C is a unique problem for nanowire electrodes.

Because RGO is not nearly as conductive as the nanowire network, it does not lower the current densities in the nanowires and therefore Joule heating still occurs. Although it avoids larger microscale hotspots and slightly lowers the average surface temperature, we can see in Figure 4.8d that the temperatures of individual nanowires in the AgNW-RGO case can still be very high. And because a single layer of RGO does not prevent nanowire degradation completely, as evidenced by the slight resistance increase during annealing (1.5 times after 14 days) and by the observation of some nanowire corrosion in the SEM after extended current flow, the current densities in the nanowires increase over time. This leads to more and more Joule heating until ultimately the substrate melts over microscale areas, causing the nanowire networks to distort and fail.

In addition to concerns about electrode failure, our models show that the temperature of  $5.5 \pm 0.5$  % of the unpassivated nanowires, and  $5.0 \pm 0.5$  % of the RGO-passivated nanowires, exceed 100 °C, which could also adversely affect other materials in a device. Because organic materials are not stable at high temperatures, the maximum operating temperature for organic solar cells and LEDs is commonly below 100 °C [114–117]. This is lower than the melting point of PET and is thus a more

stringent thermal budget. This is another reason why Joule heating in nanowire electrodes is a major concern that needs to be addressed.

#### 4.3.7 Managing Joule heating

Our results show that a passivation layer alone is not sufficient to manage the Joule heating problem in silver nanowire transparent electrodes. To reduce Joule heating, the current density in individual nanowires needs to be reduced. One way to achieve this is to increase the density of the nanowires in the electrode so that there are more current pathways. A 20 Ohm/sq AgNW electrode was modelled (Figure 4.9a) and the current density distribution in the nanowire segments when 20 mA/cm is applied across the electrodes is plotted in Figure 4.9b. The average current density in the nanowire segments is  $0.6 \pm 0.1 \times 10^5$  A/cm<sup>2</sup>, which is half of the average current density in 60 Ohm/sq AgNW electrode.

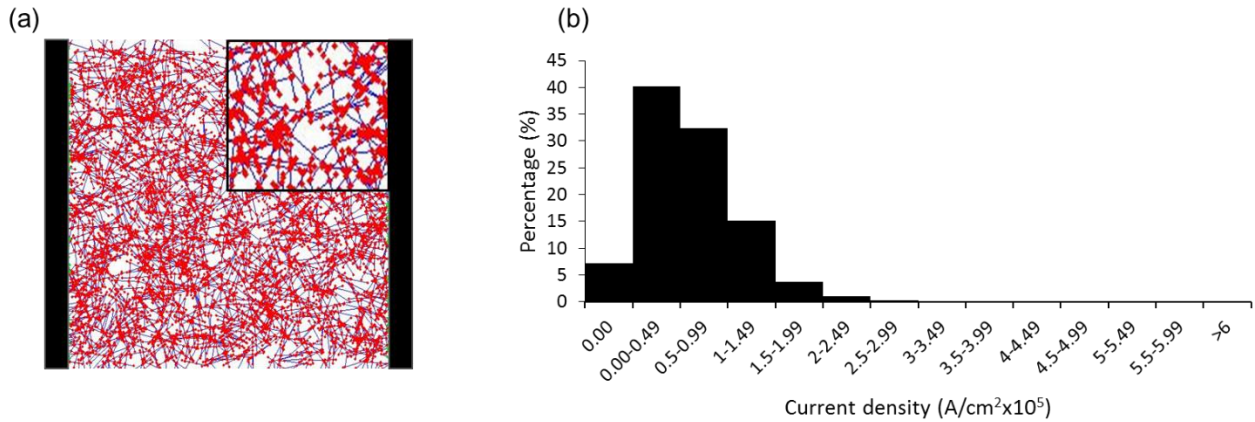


Figure 4.9 (a) Silver nanowire electrode model with a sheet resistance of 20 ohms/sq (red dots show nanowire junctions and endpoints). (b) The distribution of current densities in individual nanowire segments (i.e. between two red dots) of the 20 ohms/sq nanowire electrode.

The simulation results of Joule heating in the 20 ohms/sq electrodes are shown in Figure 4.10. The steady state temperature of the AgNW and AgNW-RGO samples under the average current density reached to 27 °C and 25 °C, respectively (Figure 4.10 a and b), which is 6 and 5 degrees lower than in the 60 ohm/sq case. In the AgNW and AgNW-RGO electrodes, less than  $0.006 \pm 0.003$  %

and  $0.002 \pm 0.001$  % of the nanowires, respectively, carry a current that results in a temperature above  $250$  °C. In addition, only  $0.45 \pm 0.15\%$  and  $0.15 \pm 0.1\%$  of the nanowires get hotter than  $100$  °C in the AgNW and AgNW-RGO electrodes, respectively. Overall, Joule heating is significantly reduced in NW electrodes with lower sheet resistance. Increasing the nanowire density in the electrodes has drawbacks however; the electrode transparency would decrease and the material cost will increase.

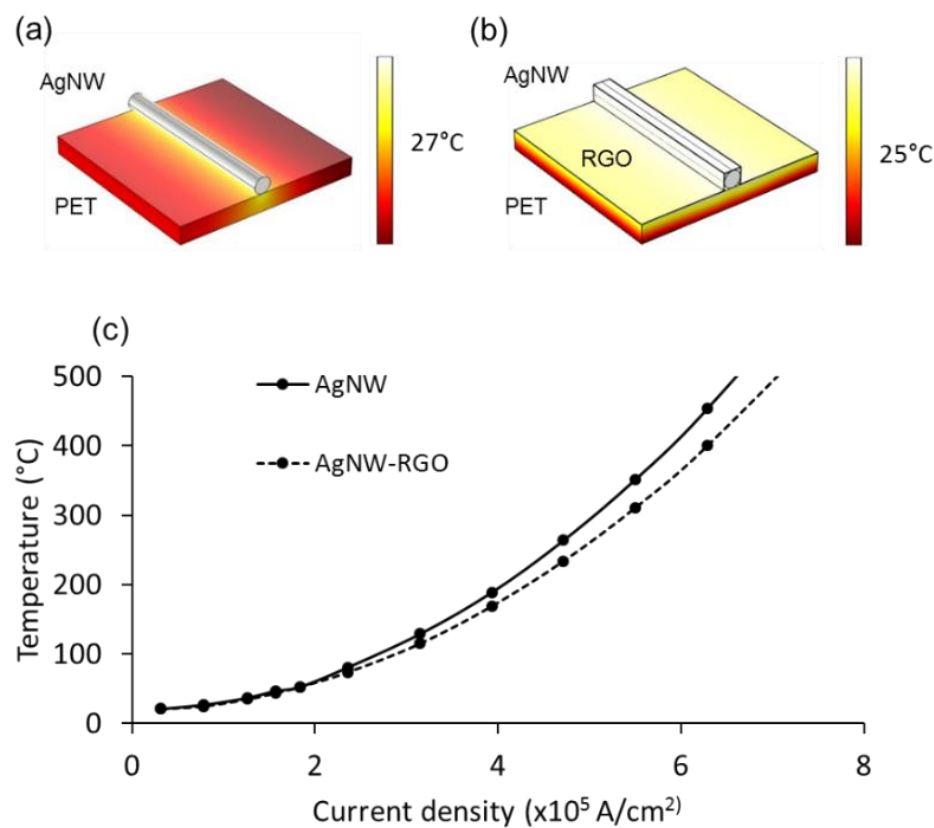


Figure 4.10 Modelling results for a  $20$  ohms/sq electrode (rather than a  $60$  ohm/sq electrode). Steady state thermal profile of a (a) AgNW and (b) RGO-passivated AgNW under a current density of  $0.7 \times 10^5$  A/cm $^2$ . (c) Calculated steady state temperature of individual unpassivated and passivated silver nanowires on PET substrates under different current densities.

A second way to reduce the current density in individual nanowires is to, of course, have less current flowing across the electrode. In a solar cell this is achieved by making the active area smaller, or in other words, making the metal bars closer together, to lower the maximum current

levels which occur near the metal bar. This, however, reduces the efficiency of the solar cells by increasing the surface area covered by the metals bars.

If the temperature of a AgNW electrode needs to remain below a certain value during operation for a given device (eg. an organic device which cannot tolerate temperatures above 100°C), our model and simulations can calculate the maximum linear current density that can be conducted. Figure 4.11 shows the temperature of the hottest silver nanowire in 300 μm x 300 μm electrodes with sheet resistances of 20 and 60 ohms/sq. If the thermal budget of a device is 100 °C, for example, the maximum linear current density that should be conducted across the 60 ohms/sq electrode is 5.5 mA/cm. This number increases to 9.5 mA/cm for an electrode with a sheet resistance of 20 ohms/sq.

#### **4.4 Conclusion**

This study demonstrates that the Joule heating that occurs in silver nanowire electrodes when they continuously conduct current is a much more serious problem than in conventional transparent conductive materials like ITO. When a 60 ohms/sq AgNW electrode conducts current at the levels incurred near the metal contacts of organic solar cells, the resulting Joule heating leads to electrode failure in 5 days. An RGO passivation layer extends the electrode lifetime, but only to 12 days since it cannot prevent the Joule heating that ultimately leads to failure due to localized melting of the plastic substrate. Modelling showed that the temperature of some individual nanowires under current flow reach much higher temperatures than the average measured surface temperature. This explains the observation of substrate melting and the faster failure times compared to electrodes whose lifetimes are assessed by annealing rather than current flow. If silver nanowire electrodes are used in solar cells, OLEDs, or transparent heaters, steps must be taken to reduce the Joule heating problem to extend both the lifetime of the electrode and the rest of the device as well.

Lowering the electrode sheet resistance or lowering the current flowed across the electrode would both be effective strategies.

# **Chapter 5**

## **Integration of silver nanowire electrodes into devices**

Silver nanowire electrodes are a promising option to replace ITO because of their low sheet resistance, high transmittance, and high mechanical flexibility. In this chapter, the results of our collaboration with two research groups on integrating silver nanowire electrodes into devices are presented. In the first project a polymer dispersed liquid crystal (PDLC) smart window using silver nanowire electrodes is demonstrated for the first time, which is the result of a collaborative project with Prof. Nasser Abukhdeir's group in the Chemical Engineering Department at the University of Waterloo. Kelvin Liew (from Prof. Abukhdeir's group) participated in the design of the study, prepared the PDLC material, and fabricated the smart windows. I participated in the design of this study, prepared the silver nanowire electrodes, and tested the devices' performance. It is shown that the nanowire electrodes have superior performance characteristics compared to traditional ITO electrodes while being lower in cost. The results of this study have been published in the journal "Solar Energy Materials and Solar Cells" in September 2014 [76]. In the second collaborative project, with Prof. William Wong's research group in Electrical and Computer Engineering department of the University of Waterloo, silver nanowires in conjunction with Al-doped ZnO (AZO) were developed as a conformal and transparent electrode to improve the efficiency of 3D solar cells. Minoli K. Pathirane (form Prof.Wong's group) participated in the design of the study, fabricated of 3D solar cells, tested the devices' performance. I participated in the design of this study, and fabricated and optimized the properties of the silver nanowire electrodes as the top electrode for the 3D solar cells.

## **5.1 Integration of silver nanowire electrode into smart windows**

### **5.1.1 Introduction**

PDLC smart windows are used in the architectural and automotive industries due to their relatively simple fabrication process, durability, fast switching speed, and low transmittance in the “off” or translucent state [118]. These windows can be used as switchable privacy glass or as energy saving windows through the modulation of solar heat gain [30,119,120]. The operating principle behind PDLC-based smart windows involves the use of an electric field to actuate an optoelectronically active PDLC film sandwiched between two parallel transparent electrodes. An alternating voltage potential is applied across the two electrodes to “switch” the film between a translucent “off” state and a transparent “on” state. The cost of these transparent electrodes is a significant issue for increased adoption of PDLC smart windows [30]. Candidate transparent electrodes require a balance of high transparency, low sheet resistance, and low-cost. While the benefits of increased transparency and low-cost are obvious, low sheet resistance is beneficial in minimizing the voltage drop across the electrode [121,122] and to ensure fast switching times [123],[124]. Most commonly, the transparent electrode type used in the manufacture of PDLC smart windows and other optoelectronic devices is indium tin oxide (ITO). These ITO transparent electrodes are relatively high-cost due to the cost of indium metal and its processing into ITO. This cost is exacerbated by the fact that PDLC-based smart window deployments involve surface areas on the order of ~1 m<sup>2</sup>, compared to other applications of ITO electrodes such as LCDs where surface areas are on the order of ~0.1 m<sup>2</sup>. Furthermore, the fabrication of smart windows on plastic substrates instead of glass is often desired because plastic substrates are lightweight, flexible, and can be laminated onto existing windows. However, the temperatures typically used for ITO deposition are not compatible

with plastic substrates, so lower than ideal deposition temperatures must be used which results in higher sheet resistances.

This study presents the first results using nanowire electrodes integrated into PDLC-based smart windows. These electrodes provide significant promise compared to other ITO alternatives due to their low cost, high conductivity, and high transmittance.

### **5.1.2 Device fabrication**

#### **5.1.2.1 Silver nanowire electrode**

In this work, silver nanowires dispersed in ethanol with an average diameter of 35 nm and an average length of 15  $\mu\text{m}$  were supplied by Blue Nano Inc. Using the Mayer rod coating method, which is described in the previous chapter, films of nanowires were uniformly deposited on 5 x 5 cm PET substrates of 125  $\mu\text{m}$  thickness and then rolled at room temperature using a rolling press (MSK-HRP-01, MTI Corporation). The electrodes were rolled at room temperature since the roughness of the electrodes is not critical for smart window applications. The rolling process was done to increase the adhesion of the nanowires to their substrate which facilitates handling and fabrication of the devices. The nanowire density was selected so that a sheet resistance of 50  $\Omega/\text{sq}$  was obtained. ITO films with a sheet resistance of 50  $\Omega/\text{sq}$  on 5 x 5 cm PET substrate were purchased from Sigma Aldrich Inc.

#### **5.1.2.2 Polymer dispersed liquid crystal layer and device**

A cross-sectional schematic of the PDLC smart window fabricated in this work is shown in Figure 5.1. A PDLC layer is sandwiched between two transparent electrodes; the PDLC layer is composed of a nematic liquid crystal (E7) guest phase domains dispersed in a polymer matrix (NOA-65) host phase. In the absence of an electric field (the “off” state), the liquid crystal droplets are randomly

oriented. In this state, incident light is scattered due to both the birefringence of the LC domains and mismatch refractive index of the LC/polymer<sup>[125]</sup> which results in a translucent film. When a voltage potential is applied across the two electrodes the electric field aligns the liquid crystal droplets parallel to the electric field, correlating the optical axes of each droplet. In this state, incident light is no longer scattered given that the indices of refraction of the guest and host phases are commensurate and results in a transparent state (the “on” state). Details about the fabrication of the LC layer and the full PDLC device are described in the journal paper<sup>[76]</sup>.

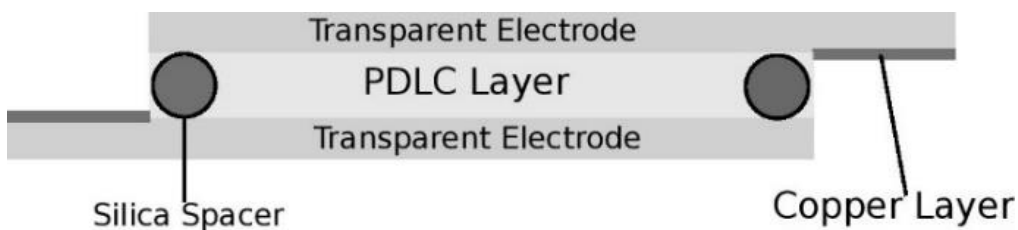


Figure 5.1 Schematic of the cross-section of the PDLC smart window.

### 5.1.3 Performance of the fabricated smart windows

Figure 5.2a shows the specular transmittances (unscattered transmitted light) of the silver nanowire and ITO electrodes. The nanowire electrode is slightly more transparent than ITO. At 550 nm, the transparency of the nanowire and ITO electrodes are 92.4% and 89.6%, respectively. An SEM image of the nanowire electrode is shown in Figure 5.2b.

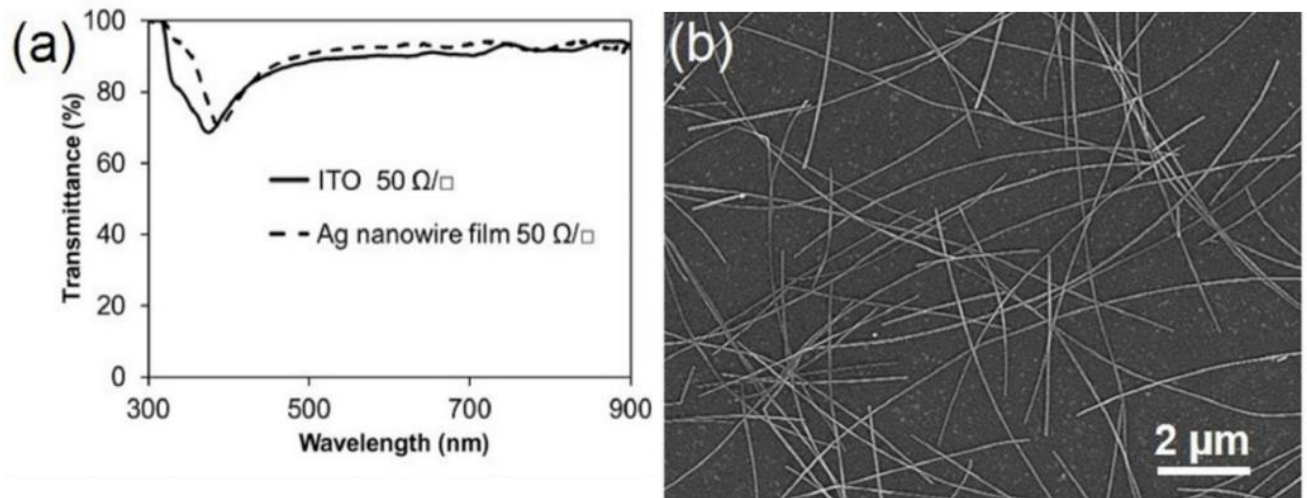


Figure 5.2 (a) Transparency spectra of silver nanowire and ITO films of the same sheet resistance. (b) SEM image of the silver nanowire electrode.

Nanowire electrodes are structured as two-dimensional networks on a micro scale, in contrast to ITO electrodes which are uniform films. For a  $50 \Omega/\text{sq}$  nanowire electrode, the characteristic length scale between nanowires is approximately  $2 \mu\text{m}$  (Figure 5.2b). The resulting electric field between the two types of substrates can thus be different. In the case of ITO electrodes, the field is essentially one-dimensional. For nanowire electrodes, this is not the case for low surface coverages which are desired from a cost and transparency perspective. Given that the electrooptically active domains in the PDLC film are on the order of  $1 \mu\text{m}$ , there is the possibility of non-uniform electric field effects on the transparent “on” state. However, from the images in Figure 5.3a and b which show the PLDC-based smart window using nanowire electrodes, it can be seen that the window is uniform in both on and off states for the surface coverages used in this work. This indicates that the electric field between the nanowire electrodes is sufficiently uniform.

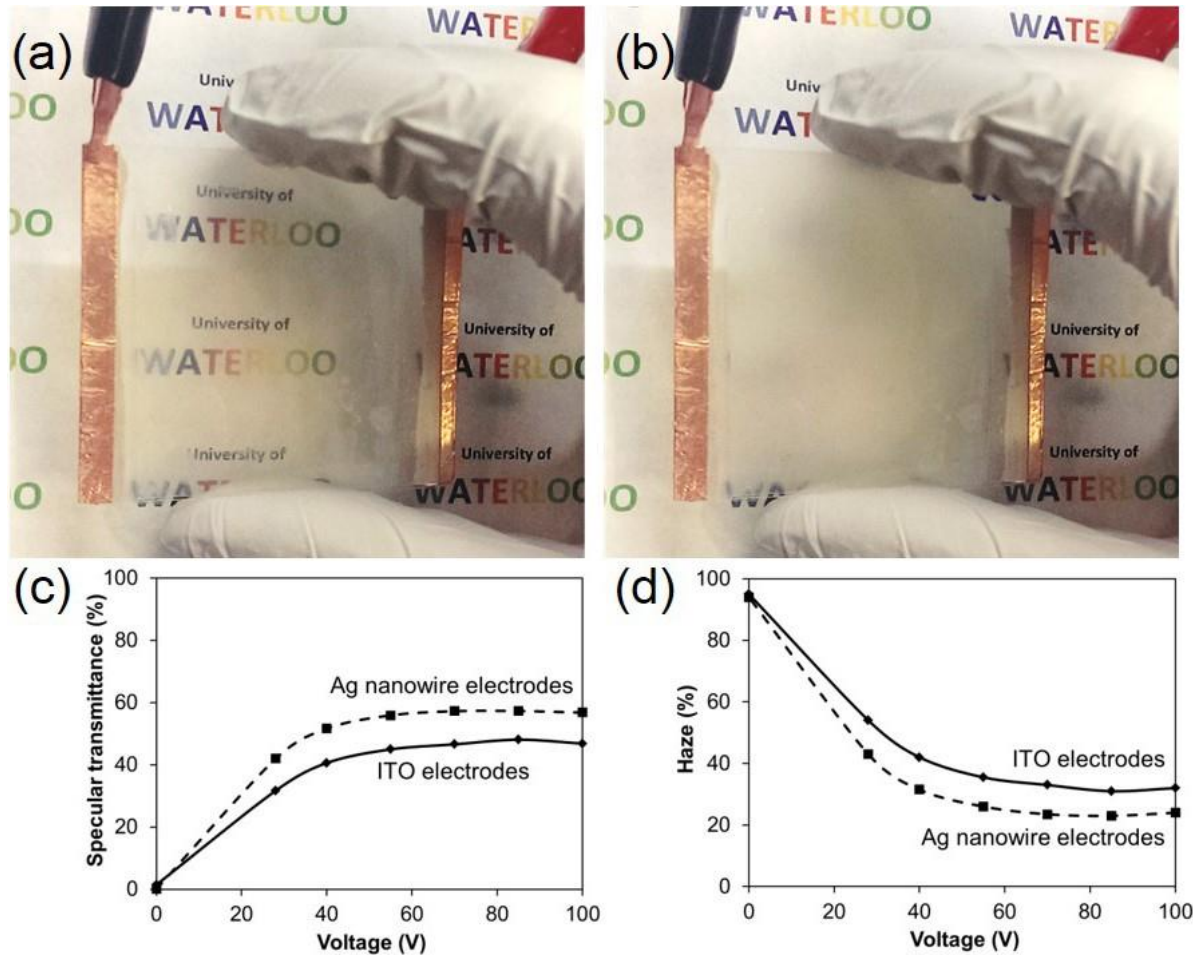


Figure 5.3 Example of a nanowire electrode-based PDLC smart window with (a) 85 V (on state) which corresponds to an electric field of 3.4 V/ $\mu$ m and (b) 0 V (off state) applied across the two electrodes. The effect of voltage on the (c) specular transmittance and (d) haze of the nanowire-based and ITO-based PDLC window at a wavelength of 550 nm.

The variation of specular transmittance (light transmitted through the device without scattering) and haze (transmitted light that is scattered) on the applied voltage for both the nanowire-based and ITO-based window devices are shown in Figure 5.3c and d. In the off state (0 V), almost all the incident light in both devices is forward scattered. As the voltage potential increases, more of the incident light is transmitted through the device without scattering and saturates above a critical voltage. As can be seen in Figure 5.3c, the nanowire-based device reaches its maximum specular

transmittance of 58.5% at 50 V while the ITO-based device reaches its maximum transmittance of 50.5% at 85 V. Thus, the nanowire-based device is not only more transparent in the on state, but it can also be operated at a lower voltage which results in lower energy consumption. Referring to Figure 5.3d, the haze of the nanowire-based device in the on-state is also superior to the ITO-based device, being 8% less.

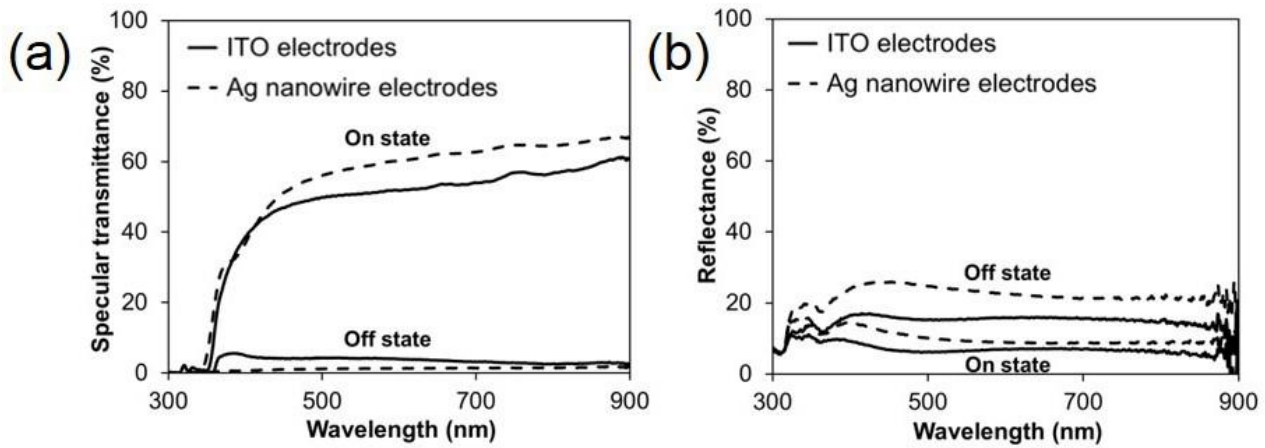


Figure 5.4 (a) Specular transmittance and (b) reflectance of the silver nanowire and ITO PDLC windows in the “on” and ‘off’ states.

Figure 5.4a shows the specular transmittance versus wavelength for both devices in the on and off states. 85 V was selected as the on state voltage as according to Figure 5.3c the transmittance of both devices is saturated at this voltage. The transparency difference at 550 nm between the on and off states for the nanowire-based device,  $\Delta T_{\text{on-off}}$ , is 57.3% (58.5% in the on state and 1.2 % in the off state).  $\Delta T_{\text{on-off}}$  for the ITO-based device is 46.4% (50.5% in the on state and 4.1% in the off state). The higher transmittance in the on-state and the lower specular transmittance in the off-state of the nanowire-based device are desirable attributes for use as smart windows.

The 8% higher transmittance of the nanowire-based device in the on-state cannot solely be explained by the higher transparency of the two nanowire electrodes alone, as each nanowire

electrode has only a 2.5% higher transparency than ITO. The higher transmittance is likely also due to less light being scattered at each nanowire electrode compared to the ITO case. ITO has an index of refraction of 1.9<sup>[4]</sup>. Because this is higher than the refractive index of PET ( $n = 1.6$ <sup>[126]</sup>) and the PDLC layer ( $n = 1.5$ <sup>[127,128]</sup>) some light will reflect at each of the two PET/ITO and ITO/PDLC interfaces. The nanowire film, on the other hand, only covers 10% of the PET surface and thus it is expected that less light would reflect and refract at the PET/nanowire-film and nanowire-film/PDLC layer interface. To confirm this hypothesis, the effective refractive index of the ITO/PET/air layer was calculated using transmission line theory relations:

$$\frac{\eta_0}{n_{total}} = \eta_2 = Z_{ITO} \frac{\eta_1 + jZ_{ITO} \tan(\beta_{ITO} l_{ITO})}{Z_{ITO} + j\eta_1 \tan(\beta_{ITO} l_{ITO})}$$

Where  $n_{total}$  is the effective refractive index,  $\eta_0$  is impedance of free space,  $\eta_1$  is the calculated impedance of the PET film with 125  $\mu\text{m}$  thickness,  $\eta_2$  is the relative impedance of the multiple layer of ITO/PET/air,  $l_{ITO}$  is thickness of ITO film (130 nm), and  $Z_{ITO}$  is the impedance of ITO with a value of 198 ohms. The results of the calculation at the wavelength of 550 nm showed that the  $n_{total} = 1.75$  for ITO/PET/air film. However, this value for PET/air film is 1.59.

The slightly higher transmittance of the ITO-based device in the off-state may be because some of the light backscattered by the PDLC is internally reflected at the first ITO/polymer interface and gets transmitted forward.

Figure 5.4b shows the light incident on the two types of devices that is reflected backwards toward the light source. The difference of reflectivity in the off and on states for the nanowire-based device is 14.3% (23.6% in the off-state and 9.3% in the on-state), while for the ITO device it is 9% (15.5% in the off-state and 6.5% in the on-state). A higher modulation range is advantageous for solar gain applications. The higher reflection of the nanowire-device is likely because metals are reflective

and do not absorb much visible light. ITO on the other hand will absorb up to half of the untransmitted light in the visible range [129].

By decreasing the density of the nanowires on the electrode, a higher transparency is obtained with a trade-off of a higher sheet resistance. PDLC smart windows fabricated using silver nanowire electrodes with a sheet resistance of  $100 \Omega/\text{sq}$  were also tested. These devices worked successfully with on and off transmittances of 63.5% and 1.1%, respectively ( $\Delta T_{\text{on-off}}=62.4\%$ ). If a lower sheet resistance is required to minimize the voltage drop across the electrode, a higher density of nanowires can be used.

The PDLC device fabricated using nanowire electrodes operated successfully when the device was bent to a radius of curvature of 20 mm, and thus these devices can be formed onto curved geometries. Although the silver nanowire electrodes themselves can be bent to lower radii of curvature without degradation, and maintain their sheet resistances after repeated bends the flexibility of the PDLC device is limited by the PDLC layer. The PLDC layer delaminates from the electrodes at low bending radii or after repeated bends.

#### **5.1.4 Conclusions**

In summary, silver nanowire electrodes are a viable alternative to ITO for use in PDLC smart windows. The material and fabrication costs of silver nanowire films are lower than ITO and enable superior optical transparency performance. The transparency of nanowire PDLC smart windows can be modulated over a larger range, with  $\Delta T_{\text{on-off}}= 57\%$  versus  $\Delta T_{\text{on-off}}= 46\%$  for the ITO-based devices. A lower voltage supply is required to operate the nanowire-based device since its on-state can be reached 15 V lower than the ITO-based device. The presented results support the use of nanowire electrodes to both increase performance and lower the cost of PDLC-based

smart windows. Furthermore, these results support the use of nanowire-based electrodes for a range of other liquid crystal and smart window technologies.

## **5.2 Conformal and Transparent AZO/Ag Nanowire Composite Electrodes for Flexible 3-Dimensional Nanowire Solar Cells**

3-Dimensional nanowire solar cells are interesting structures that achieve a high power-conversion efficiency (PCE) by enabling short minority carrier extraction distances and higher optical absorption. In this study, disordered ZnO nanowires were grown on glass and plastic substrate and then a multiple layer of p-i-n doped a-Si:H and Al-doped ZnO (AZO) were deposited on the ZnO nanowires using plasma-enhanced chemical vapour deposition (PECVD) and sputter-coating to fabricate 3-D nanowire solar cells. This structure was supposed to have enhanced performance compare to the planar structure. However, the poor contact of the AZO to the Si layers prevented a significant improvement of performance. This is due to the fact that with the PVD deposition method, disordered nanowires shadow materials deposition, and therefore most side walls of the nanowires could not be coated with AZO. To solve this contact problem in a collaborative study, a film of silver nanowires was deposited after the AZO deposition to enable a conformal contact structure for the top electrodes while maintaining high optical transmission. The schematic of the nanowire solar structure is illustrated in Figure 5.5a.

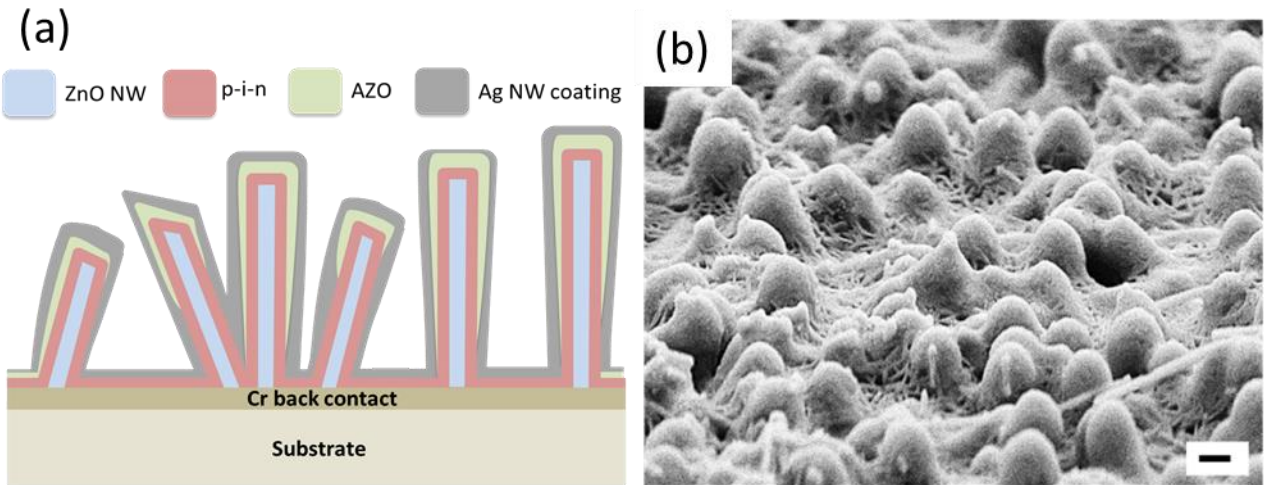


Figure 5.5. (a) Schematic of the nanowire solar cell device. (b) SEM image of Ag NWs coated on nanowire solar cells after annealing at 200°C. Scale bar is 1  $\mu$ m. SEM image courtesy of Minoli K. Pathirane.

The efficacy of the Ag NW contact was found to be a function of the annealing temperature. An annealing temperature of 200°C was found to be optimal to conformably coat the 3-D structures (as shown in Figure 5.5b) and minimize the NW sheet resistance,  $R_{sheet}$ . The composite top electrode in the nanowire solar cells fabricated on glass substrates helped improve the total PCE to 6.3% compared to 3.9% from the nanowire solar cells that only used AZO electrodes. The 3-D devices on polyethylene naphthalate (PEN) substrates showed a PCE improvement to 5.5% with the top composite film compared to 4.0% with only AZO electrodes. The increased PCE values achieved is attributed to the increased absorption that occurred by enhanced light scattering from the Ag NWs and more efficient carrier collection by the composite electrode. This is another example of the application of silver nanowire transparent network in devices that can be used to enhance the performance of the existing devices. More detail about this study can be found in detail in Minoli Pathirane's thesis published recently,<sup>[130]</sup> and our paper<sup>[131]</sup>.

# **Chapter 6**

## **Growth of nanocubes on silver nanowires**

During the annealing process of silver nanowires during fabrication and for stability studies, we observed the formation of nanocubes with sharp edges that attracted our attention. We studied the growth of these nanostructures further to find the composition of the nanocubes and the important parameters that affect their size and density. This investigation resulted in developing a method of growing nanocubes on nanowires as a unique hybrid structure. In this chapter, the growth of AgCl nanocubes directly on the sidewalls of Ag nanowires is demonstrated. The nanocubes can be simply obtained through extended low temperature annealing of polyol-synthesized silver nanowires in vacuum. The length of time and temperature of the anneal and the diameter of the nanowire affect the size and density of the nanocubes obtained. It is hypothesized that the AgCl material is supplied from reactants leftover from the silver nanowire synthesis. This novel hybrid nanostructure may have applications in areas such as photovoltaics, surface enhanced Raman spectroscopy, and photocatalysis. The results of this study have been published in the journal “Nanotechnology” in September 2015.

### **6.1 Introduction**

The crux of nanotechnology is exploiting the unique properties that arise when material feature sizes are on the order of or smaller than ~100 nm. The size, shape, and composition of nanostructures can all significantly affect their characteristics<sup>[132–141]</sup>. For example, the size of a nanostructure can lead to changes in surface energy, electronic band structure, thermal conductivity, among many other properties<sup>[142–147]</sup>. Because of this, a multitude of nanostructures

such as spheres, wires, cubes, plates, and polyhedral of varying sizes have been synthesized and studied over the past couple of decades [132–134].

Integrating more than one shape, feature size, and/or material into one hybrid nanostructure can impart increased functionality [148–154]. In this work, nanocubes are grown on the surface of nanowires. Nanowires, unlike nanocubes and nanoparticles, have one long dimension. This long axis can be used to transport electrical current and heat, it makes nanowires easier to contact for use in devices, and it allows for a connected network to be achieved at a far lower particle density, the latter which is useful for applications such as transparent electrodes. By adding nanocubes on nanowire sidewalls, the advantages of nanocubes can be combined with nanowires such as their larger surface-area-to-volume ratio and surface plasmon resonance at different wavelengths than the nanowire. Furthermore, if the nanocubes and nanowires are different materials, the properties of each material can be exploited and combined in a useful way. Nanowires with nanoparticles on their surface have been used in applications such as sensors, catalysts, and photovoltaics [149–151]. There exist several methods of decorating the surface of nanowires with nanoparticles or nanocubes. The nanowire is first synthesized and nanoparticles are then grown or attached on their sidewalls through methods such as chemical vapour deposition or solution synthesis [155,156]. For example, for surface enhanced Raman spectroscopy (SERS) applications, silver nanocubes were attached onto silver nanowires by mixing pre-synthesized individual nanocubes and nanowires together in solution [157]. However, the spatial orientation of the nanocubes with respect to the nanowire sidewalls was not controllable. This is not ideal since the maximum surface plasmon resonance happens when the face of a nanocube is flat against the sidewall of the nanowire [157]. In another report, silver phosphate cubes were grown around silver nanowires in solution. The

average edge length of the cubes however was 500 nm, 10 times larger than the diameter of the nanowire and too big to be used in nanoscale applications [158].

In this chapter we show for the first time that nanocubes can be synthesized directly on the sidewalls of a metallic nanowire through a simple anneal in vacuum. This is also the first report of AgCl nanocube/Ag nanowire hybrid structures. The size and density of the nanocubes are controlled through the annealing temperature and time. The cubes lie flat against the nanowire facets and are likely epitaxial. These structures have many potential applications. Firstly, the nanocubes increase the surface area of the nanowire which is beneficial for catalytic, sensing, and antibacterial applications [159,160]. Secondly, films of silver nanowires have been used as substrates for SERS applications to increase signal intensity [161]. The addition of nanocubes on their surfaces can further enhance the SERS signal [162], which improves sensitivity of detection. Thirdly, films of silver nanowires are a promising transparent electrode for use in photovoltaic devices [40]. Having nanocubes on the nanowire surfaces may increase light absorption in a thin-film solar cell due to increased light scattering, as has been shown to be the case when nanoparticles are added to the transparent electrode of solar cells [163–165]. Fourthly, the nanocubes are silver chloride which is a visible-light driven photocatalyst useful for water splitting and the decomposition of organic pollutants<sup>[166,167]</sup>. Their attachment to a silver nanowire can enhance their photocatalytic performance since the silver can promote charge separation and transport generated electrons [160,168,169]. In addition to these potential applications, this communication helps to explain why many groups observe nanoparticles on silver nanowires in transparent electrodes [170,171].

## 6.2 Experiment setup

Poly(vinylpyrrollidone) (PVP) directed polyol synthesis is a solution-based method that can be used to synthesize crystalline silver nanostructures of various well-controlled shapes. In this

method, a mixture of AgNO<sub>3</sub> and ethylene glycol (EG) is gradually added to a solution containing EG with PVP and NaCl and is heated to 170 °C. Depending on the concentration of AgNO<sub>3</sub> and the molar ratio of AgNO<sub>3</sub> and PVP, various shapes such as nanocubes, nanowires, spheres, and triangular plates can be obtained. For silver nanowire synthesis, the resulting nanowires have a pentagonal cross-section, with 5 {100} sidewalls [22,172].

In this study, two different sizes of polyol-synthesized silver nanowires dispersed in ethanol were commercially obtained; ones with an average diameter and length of 90 nm and 15 μm, respectively (Blue Nano Inc., Charlotte, NC), and 200 nm and 25 μm, respectively (ACS Materials Inc., Medford, MA). Silicon wafer chips were cleaned in a sonication bath with ethanol, acetone and distilled water, each for one minute. The as-received nanowires were diluted with ethanol and drop cast onto the Si. They were then annealed in low vacuum for various lengths of time, ranging for 3 to 14 days, and at temperatures ranging between 100 °C to 150 °C. Scanning electron microscopy (SEM) images were taken of the samples before and after annealing. The average density and size of the nanocubes were calculated from these SEM images by measuring a minimum of 100 nanocubes for each experimental condition. Transmission electron microscopy (TEM) samples were prepared by mechanically rubbing the silver nanowires from the silicon wafer onto TEM grids. Energy dispersive X-ray spectroscopy (EDS) spectra were collected to determine the chemical composition of the nanocubes and nanowires.

### 6.3 Results and discussion

An SEM image of the 90 nm silver nanowires before annealing is shown in Figure 6.1(a). The sidewalls of the nanowires are smooth. After annealing for 3 days at 100 °C (Figure 6.1(b)), nanocubes of various sizes are observed on the surface of the nanowires. All cubes appear to have smooth facets and sharp corners. Almost all are oriented such that a cube face lays flat against the

nanowire sidewall, and with cube edges aligned parallel to the nanowire axis. Their edge lengths range from 20–120 nm. After annealing for 7 days (Figure 6.1(c)), the nanocubes are larger, with edge lengths ranging from 40–200 nm, but are less dense than with the 3 day anneal. In general, as shown in Table 6.1, as the nanowires are annealed for longer times the obtained nanocubes are larger and less dense, likely because of the increased time for Oswald ripening to occur.

The nanowire diameter also affects the size and density of the nanocubes. An image of 200 nm diameter nanowires annealed for 7 days at 100 °C is shown in Figure 6.1(d). In general (Table 6.1), nanocubes obtained on the larger diameter nanowires are larger and less dense compared to those on thinner nanowires.

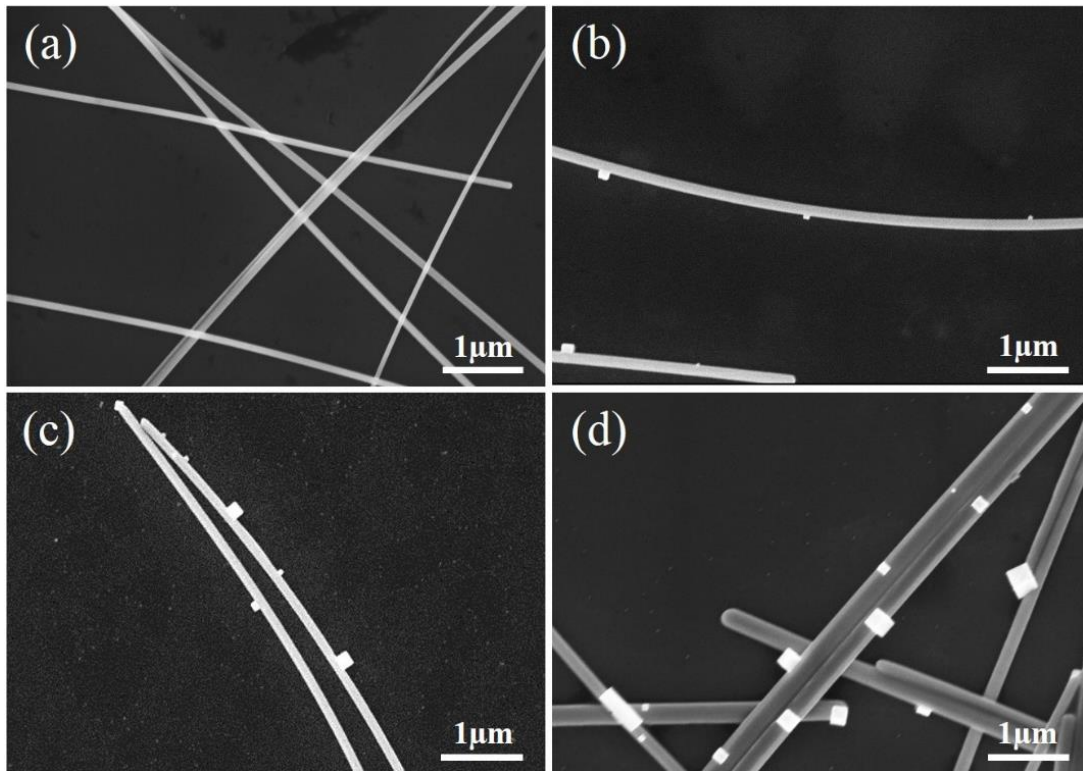


Figure 6.1 90 nm diameter silver nanowires before (a) and after annealing at 100 °C for 3 days (b) and 7 days (c). (d) 200 nm diameter nanowires after annealing at 100 °C for 7 days

Table 6.1. Density and average size of the nanocubes on nanowires after annealing at 100 °C.

|                           | <b>3 days</b>   | <b>7 days</b>   | <b>14 days</b>  |
|---------------------------|-----------------|-----------------|-----------------|
| <b>90nm</b>               |                 |                 |                 |
| Density of nanocubes      | 1.1 NC/ $\mu$ m | 0.7 NC/ $\mu$ m | 0.3 NC/ $\mu$ m |
| Average size of nanocubes | 60 nm           | 80 nm           | 100 nm          |
| <b>200 nm</b>             |                 |                 |                 |
| Density of nanocubes      | 1 NC/ $\mu$ m   | 0.3 NC/ $\mu$ m | 0.2 NC/ $\mu$ m |
| Average size of nanocubes | 80 nm           | 300 nm          | 350 nm          |

The nanowires were also annealed at temperatures of 125 °C and 150 °C. Similar to increasing annealing time or nanowire diameter, higher temperatures also led to larger and less dense nanocubes. However, even at 125 °C the nanocubes had average edge lengths of more than 500 nm after 3 days. This large size is not as attractive for nanoscale applications and thus 100 °C is a more preferable annealing temperature.

EDS spectra of 90 nm nanowires annealed for 7 days at 100 °C in vacuum are displayed in Figure 6.2. In Figure 6.2(a), the electron probe was focused on a section of a nanowire away from a nanocube. Other than carbon, only silver was detected. When the probe was focused on a nanocube (Figure 6.2(b)), the spectrum contained an additional peak corresponding to chlorine. This suggests that the nanocubes are AgCl, since AgCl is the only compound occurring in the silver-chlorine system. Moreover, it is known that AgCl nanocubes form in the presence of Ag<sup>+</sup>, Cl<sup>-</sup>, and PVP (more discussion on this later). Attempts at TEM imaging and the collection of diffraction patterns to characterize the morphology, lattice structure, and the epitaxial relationship of the nanocubes to the nanowires were made. However, the nanocubes quickly decomposed upon

exposure to the electron beam preventing such characterization. This decomposition and the inability to image AgCl nanocubes in the TEM has been reported by others [173,174]..

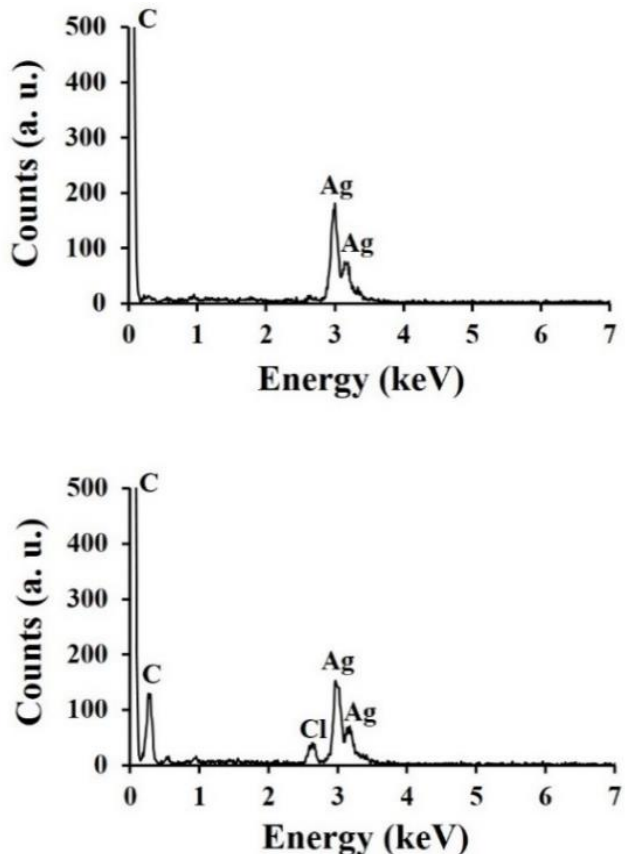


Figure 6.2 Energy-dispersed X-ray spectroscopy (EDS) spectrum from (a) a portion of a silver nanowire away from a nanocube and (b) a nanocube on a nanowire.

In the polyol synthesis of silver nanowires, silver ions ( $\text{Ag}^+$ ) bond with chlorine ions (provided by NaCl) and form  $\text{AgCl}$  nanocrystals to control the growth rate of the silver nanostructures [177]. Some  $\text{AgCl}$  nanocrystals remain in the solution after the synthesis of the nanowires is terminated. When the nanowires are deposited on the Si substrate, the solvent evaporates and the  $\text{AgCl}$  nanocrystals remain on the surface of the nanowires and the substrate. It is worth noting that EDS spectra taken from localized points on unannealed silver nanowires do not show a Cl peak [78,175,176], which gives some evidence that the Cl is held in nanocrystals rather than existing

as a residue everywhere on the nanowire. Elevated temperatures facilitate the diffusion of these nanoparticles. We hypothesize that the nanocubes form because of Oswald ripening of these particles, and the cubic shape is due to the presence of PVP which selectively binds and stabilizes the {100} surfaces of AgCl<sup>[160]</sup>. It has been shown that when AgCl particles are synthesized in solution by mixing AgNO<sub>3</sub>, NaCl, and PVP and heating the solution to 80 °C, AgCl nanocubes with {100} sidewalls are obtained<sup>[160]</sup>. As mentioned above and can be seen more clearly in Figure 6.3, the nanocubes have sharp edges and their spatial orientation is not random, but rather lie flat on the {100} nanowire sidewalls with the cube walls parallel to the nanowire axes. Thus it is likely that the nanocubes are epitaxially related to the nanowire. If the cube faces are {100}, as is the case for all AgCl nanocubes in the literature<sup>[160,178,179]</sup>, the cube edges are thus along the <100> directions. The axes of polyol synthesized Ag nanowires are <110><sup>[180]</sup>. The {100} planes of the AgCl and Ag are thus rotated in-plane 45 degrees with respect to one another and in this orientation, there is only a 4% lattice mismatch.

Further investigation is required to determine the mechanism of nanocube formation. Nanocubes were only observed on the nanowires and not on the Si substrate. This may be because the Ag nanowires promote nanocube growth in some manner, or merely because silver has a higher surface energy than the SiO<sub>2</sub> surface on the silicon substrate and growth and diffusion are easier on higher energy surfaces<sup>[181]</sup>. The nanowire sidewalls being {100} may be particularly favorable, because not only are they not the lowest energy plane of an FCC material like Ag, but also because AgCl(100) has a much larger lattice mismatch with Ag(110) and Ag(111) planes making epitaxy on these planes unlikely.

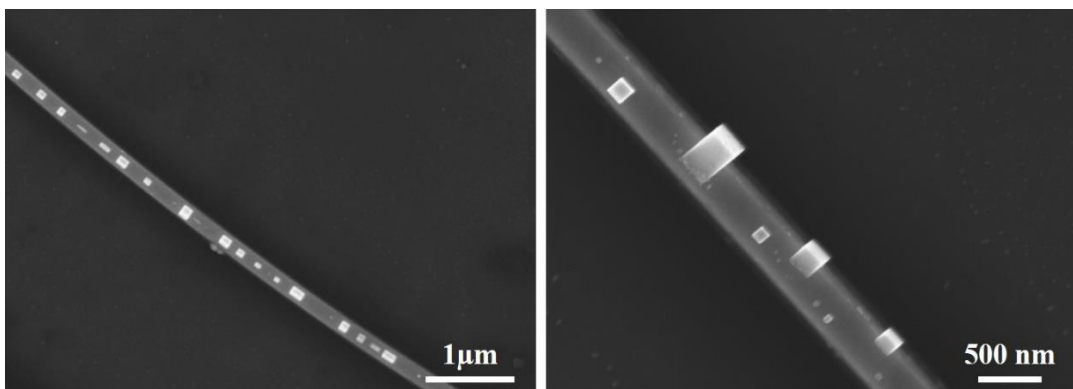


Figure 6.3 Nanocubes with sharp edges lie flat on the surface of silver nanowires, with sidewalls parallel to the nanowire axis. These nanocubes were obtained by annealing 200 nm diameter nanowires at 100 °C for 3 days.

To investigate the effect of leftover components from the nanowire synthesis solution, some nanowire samples were washed with acetone before annealing. Annealing the washed nanowires at 100 °C for 7 days did not result in any nanocube formation which is likely due to the absence of any AgCl nanocrystals. Unwashed silver nanowires were also annealed in air rather than in vacuum. Annealing at 100 °C in air for 3 days resulted in the formation of irregularly shaped nanoparticles on the nanowire sidewalls as well as a few long rectangular prisms with edge lengths of up to 1  $\mu$ m. The irregular shapes may be due to the absence of PVP for shape control, as PVP decomposes in air below 200°C in less than one hour, and would be expected to decompose at lower temperatures at longer annealing times [182]. The irregular shapes may also or instead be due to the reaction of silver with oxygen and sulfur atoms in the air [42].

#### 6.4 Conclusions

This study shows that AgCl nanocubes can be synthesized on the sidewalls of silver nanowires with a simple annealing process in vacuum. The size and density of the nanocubes are dependent on the temperature and length of the anneal, as well as the diameter of the nanowires. The presence of nanocubes on the nanowires could add extra functionality and future work will involve testing them for applications.

# **Chapter 7**

## **Summary and Future work**

### **7.1 Summary**

The main theme of this theses is the development of silver nanowire transparent electrodes for device applications including flexible devices. Silver nanowire electrodes were fabricated and shown to have superior electrical and optical properties than ITO-coated PET, in addition to being lower cost and more mechanically flexible. Major concerns associated with the use of silver nanowire in device applications were studied. In chapter 3, high surface roughness and weak adhesion of silver nanowires to their substrate are addressed by a simple hot rolling method. This method not only decreases the surface roughness of the nanowire electrodes but also increases the adhesion of silver nanowire to plastic substrate. The surface roughness and peak-to-valley values of the hot rolled electrodes were 7 nm (RMS) and 30 nm, respectively, compared to 14 nm and 90 nm for an annealed sample. In chapter 4, the Joule heating problem in silver nanowire electrodes is studied as an overlooked problem in nanowire networks when they are operated under continuous flow of current. It was found both experimentally and through models that when conducting current at levels encountered in good quality organic solar cells, some nanowires in the network conduct such a high level of current that they heat up above 250 °C, leading to melting of the nanowire and the plastic substrate underneath. Coating the silver nanowire electrodes with a passivation layer of reduced graphene oxide (RGO) increased the stability of silver nanowire under current flow and increased their lifetime. However, the RGO layer could not mitigate the Joule heating problem significantly. It was demonstrated that increasing the density of nanowires

or reducing the distance between metal bars to reduce current density should be two effective ways of managing the Joule heating problem.

In chapter 5, silver nanowire electrodes were integrated into two devices. In the first project, silver nanowire electrodes were integrated into working polymer-dispersed liquid crystal (PDLC) smart windows as an alternative to ITO. Not only were the materials and fabrication costs of silver nanowire electrodes less than that of ITO, they also showed superior electro-optical characteristics. The transmittance of the nanowire electrode-based PDLC smart windows was both higher in the on-state and lower in the off-state compared to an equivalent device fabricated using ITO electrodes. Furthermore, a lower voltage supply is required to operate the nanowire-based device since its on-state can be reached 15 V lower than the ITO-based device. In the second project, silver nanowires along with sputter-coated Al-doped ZnO (AZO) thin-films were used as a composite transparent and conformal electrode for 3-D hybrid ZnO nanowire/a-Si:H p-i-n thin-film solar cells. These cells achieved a short-circuit current density of  $13.9 \text{ mA/cm}^2$  with a fill factor of 69% on glass substrates, and a short-circuit current density of  $13.0 \text{ mA/cm}^2$  and fill factor of 62% on flexible plastic substrates. The power conversion efficiency of the 3-dimensional solar cells improved by up to 62% compared to using AZO electrodes alone due to the decreased contact resistance and improved coverage of the top electrode.

In chapter 6, a method to grow AgCl nanocubes on silver nanowires through simple annealing is presented, with an investigation of the effect of annealing parameters on the size and density of the nanocubes. This novel hybrid structure can have potential applications in sensing and photocatalysis.

## **7.2 Future work**

### **7.2.1 Extend the stability of silver nanowires under current flow**

In chapter 4, it is shown that Joule heating can be a serious concern in silver nanowire electrodes used in organic solar cells and OLEDs. Mitigating this problem by increasing the nanowire density or decreasing the distance between metal contacts both would have a negative effect on the solar cell performance. An RGO passivation layer was used in this study, but it was not highly conductive due to the incompatibility of reducing agents of graphene oxide with silver nanowires. A more conductive passivation layer would help reduce both maximum current densities in individual nanowires and better spread out heat. One way of using a more conductive RGO layer is to put an additional layer of RGO directly on top of the PET so that the nanowires are sandwiched between two RGO layers. Because the bottom graphene oxide layer is deposited before the nanowires, it could be reduced with more efficient agents to achieve a conductive layer. In addition to lowering current densities, it would assist with heat dissipation from the surface of plastic substrate, which might prevent substrate melting and thus increase electrode lifetime.

### **7.2.2 Integrating smooth silver nanowire electrodes into OLEDs**

A study is currently underway to integrate our low surface roughness electrodes into solution-processed flexible OLEDs. This is a collaborative project with Dr. Alexander Colsmann and Min Zhang from the Karlsruhe Institute of Technology (KIT). Specifically, the impact of low surface roughness on the performance of the OLED will be compared to OLEDs using rougher electrodes (i.e. electrodes prepared in the usual method of annealing). Figure 7.1a shows the schematic structure of the OLED with silver nanowires used in the top and bottom electrodes. Figure 7.1b shows preliminary results of the OLED working under 15 volts, which shows that the surface roughness of the electrode is in an acceptable range and does not cause short circuit between two

electrodes. The effect of surface roughness on performance will be characterized, and the fabrication process will be optimized to achieve an OLED with high luminescence and low working voltage.

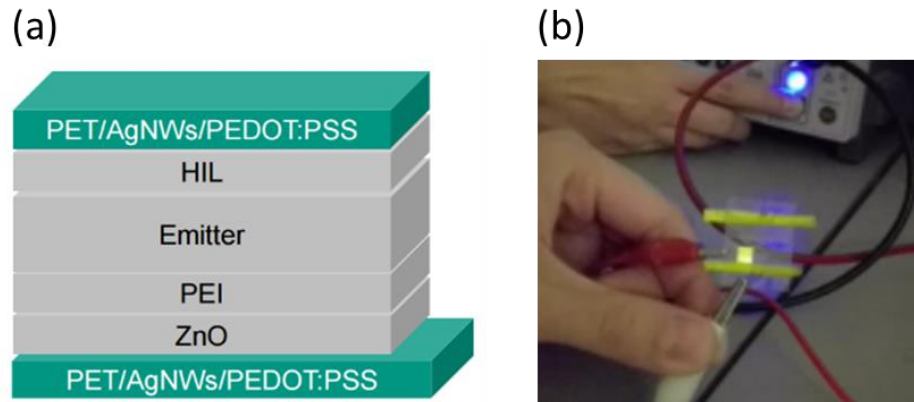


Figure 7.1 (a) Schematic of the flexible transparent OLED using nanowire electrodes. (b) Working OLED under an applied voltage of 15 V.

### 7.2.3 Applications of nanocube/nanowire structures

In chapter 6, the simple growth of AgCl nanocubes on silver nanowires is shown. This unique structure can be developed further by finding ways of growing a higher density of nanocubes with controlled sizes and density. For example, adding a chloride salt during the growth process might help to increase the number of nanocubes. In addition, studies need to be done to test these structures in applications such as sensing and photocatalysis.

# References

- [1] D. Ginley, H. Hosono, D. C. Paine, *Handbook of Transparent Conductors*; Springer Science & Business Media, 2010.
- [2] [http://www.ssi.shimadzu.com/products/literature/Spectroscopy/UV-Vis\\_Accessories.pdf](http://www.ssi.shimadzu.com/products/literature/Spectroscopy/UV-Vis_Accessories.pdf).
- [3] D. R. Cairns, D. K. Sparacin, D. C. Paine, G. P. Crawford, *SID Symp. Dig. Tech. Pap.* **2000**, *31*, 274.
- [4] D. S. Hecht, L. Hu, G. Irvin, *Adv. Mater.* **2011**, *23*, 1482.
- [5] S. Iijima, T. Ichihashi, *Nature* **1993**, *363*, 603.
- [6] M. S. Fuhrer, J. Nygård, L. Shih, M. Forero, Y.-G. Yoon, M. S. C. Mazzoni, H. J. Choi, J. Ihm, S. G. Louie, A. Zettl, P. L. McEuen, *Science* **2000**, *288*, 494.
- [7] B. Dan, G. C. Irvin, M. Pasquali, *ACS Nano* **2009**, *3*, 835.
- [8] H. C. Schniepp, K. N. Kudin, J.-L. Li, R. K. Prud'homme, R. Car, D. A. Saville, I. A. Aksay, *ACS Nano* **2008**, *2*, 2577.
- [9] A. N. Obraztsov, *Nat. Nanotechnol.* **2009**, *4*, 212.
- [10] <http://www.holoeast.com/machines/coating/WIRE-WOUND-ROD.png>
- [11] W. Hong, Y. Xu, G. Lu, C. Li, G. Shi, *Electrochem. Commun.* **2008**, *10*, 1555.
- [12] J. Zou, H.-L. Yip, S. K. Hau, A. K.-Y. Jen, *Appl. Phys. Lett.* **2010**, *96*, 203301.
- [13] D. S. Ghosh, L. Martinez, S. Giurgola, P. Vergani, V. Pruneri, *Opt. Lett.* **2009**, *34*, 325.
- [14] J. van de Groep, P. Spinelli, A. Polman, *Nano Lett.* **2012**, *12*, 3138.
- [15] L. Hu, H. S. Kim, J.-Y. Lee, P. Peumans, Y. Cui, *ACS Nano* **2010**, *4*, 2955.
- [16] D. Kowalska, B. Krajnik, M. Olejnik, M. Twardowska, N. Czechowski, E. Hofmann, S. Mackowski, *Sci. World J.* **2013**, *2013*, e670412.

- [17] V. Scardaci, R. Coull, P. E. Lyons, D. Rickard, J. N. Coleman, *Small* **2011**, *7*, 2621.
- [18] T. Tokuno, M. Nogi, M. Karakawa, J. Jiu, T. T. Nge, Y. Aso, K. Suganuma, *Nano Res.* **2011**, *4*, 1215.
- [19] S. De, J. N. Coleman, *MRS Bull.* **2011**, *36*, 774.
- [20] A. R. Rathmell, B. J. Wiley, *Adv. Mater.* **2011**, *23*, 4798.
- [21] A. R. Rathmell, S. M. Bergin, Y.-L. Hua, Z.-Y. Li, B. J. Wiley, *Adv. Mater.* **2010**, *22*, 3558.
- [22] S. Coskun, B. Aksoy, H. E. Unalan, *Cryst. Growth Des.* **2011**, *11*, 4963.
- [23] Y. Sun, B. Mayers, T. Herricks, Y. Xia, *Nano Lett.* **2003**, *3*, 955.
- [24] <http://www.fujitsu.com/downloads/EDG/binary/pdf/find/26-1e/11.pdf>,” organic conducting polymers.
- [25] C. Preston, Y. Xu, X. Han, J. N. Munday, L. Hu, *Nano Res.* **2013**, *6*, 461.
- [26] E. S. Gadelmawla, M. M. Koura, T. M. A. Maksoud, I. M. Elewa, H. H. Soliman, *J. Mater. Process. Technol.* **2002**, *123*, 133.
- [27] T. Chih-Hung, H. Sui-Ying, H. Tsung-Wei, T. Yu-Tang, C. Yan-Fang, Y. H. Jhang, L. Hsieh, W. Chung-Chih, C. Yen-Shan, C. Chieh-Wei, L. Chung-Chun, *Org. Electron.* **2011**, *12*, 2003.
- [28] W. Gaynor, S. Hofmann, M. G. Christoforo, C. Sachse, S. Mehra, A. Salleo, M. D. McGehee, M. C. Gather, B. Lüssem, L. Müller-Meskamp, P. Peumans, K. Leo, *Adv. Mater.* **2013**, *25*, 4060.
- [29] <http://phys.org/news/2013-12-3m-teams-cambrios-silver-nanowire.html>
- [30] R. Baetens, B. P. Jelle, A. Gustavsen, *Sol. Energy Mater. Sol. Cells* **2010**, *94*, 87.
- [31] R. Baetens, B. P. Jelle, A. Gustavsen, *Sol. Energy Mater. Sol. Cells* **2010**, *94*, 87.
- [32] E. Vitoratos, S. Sakkopoulos, N. Paliatsas, K. Emmanouil, S. A. Choulis, *Open J. Org. Polym. Mater.* **2012**, *02*, 7.

- [33] C. Yan, W. Kang, J. Wang, M. Cui, X. Wang, C. Y. Foo, K. J. Chee, P. S. Lee, *ACS Nano* **2014**, 8, 316.
- [34] D. Y. Choi, H. W. Kang, H. J. Sung, S. S. Kim, *Nanoscale* **2013**, 5, 977.
- [35] L. A. A. Pettersson, *Synth. Met.* **1999**, 102, 1107.
- [36] G. Li, V. Shrotriya, Y. Yao, Y. Yang, *J. Appl. Phys.* **2005**, 98, 043704.
- [37] J.-Y. Lee, S. T. Connor, Y. Cui, P. Peumans, *Nano Lett.* **2008**, 8, 689.
- [38] D.-S. Leem, A. Edwards, M. Faist, J. Nelson, D. D. C. Bradley, J. C. de Mello, *Adv. Mater.* **2011**, 23, 4371.
- [39] J. Krantz, M. Richter, S. Spallek, E. Spiecker, C. J. Brabec, *Adv. Funct. Mater.* **2011**, 21, 4784.
- [40] D. Langley, G. Giusti, C. Mayousse, C. Celle, D. Bellet, J.-P. Simonato, *Nanotechnology* **2013**, 24, 452001.
- [41] M. S. Miller, J. C. O’Kane, A. Niec, R. S. Carmichael, T. B. Carmichael, *ACS Appl. Mater. Interfaces* **2013**, 5, 10165.
- [42] H. H. Khaligh, I. A. Goldthorpe, *Nanoscale Res. Lett.* **2013**, 8, 235.
- [43] J. L. Elechiguerra, L. Larios-Lopez, C. Liu, D. Garcia-Gutierrez, A. Camacho-Bragado, M. J. Yacaman, *Chem. Mater.* **2005**, 17, 6042.
- [44] Y. C. G. Kwan, Q. L. Le, C. H. A. Huan, *Sol. Energy Mater. Sol. Cells* **2016**, 144, 102.
- [45] C. Li, L. Zhao, Y. Mao, W. Wu, J. Xu, *Sci. Rep.* **2015**, 5.
- [46] F. A. Nichols, *J. Mater. Sci.* **1976**, 11, 1077.
- [47] F. A. Nichols, W. W. Mullins, *J. Appl. Phys.* **1965**, 36, 1826.
- [48] Y. Chen, *76*, 88.
- [49] S.-B. Yang, H. Choi, D. S. Lee, C.-G. Choi, S.-Y. Choi, I.-D. Kim, *Small* **2015**, 11, 1293.
- [50] L. Hu, H. S. Kim, J.-Y. Lee, P. Peumans, Y. Cui, *ACS Nano* **2010**, 4, 2955.

- [51] Z. Yu, Q. Zhang, L. Li, Q. Chen, X. Niu, J. Liu, Q. Pei, *Adv. Mater.* **2011**, *23*, 664.
- [52] H. H. Khaligh, I. A. Goldthorpe, *Nanoscale Res. Lett.* **2014**, *9*, 310.
- [53] Technical Coating International > Capabilities.
- [54] J. Kalowekamo, E. Baker, *Sol. Energy* **2009**, *83*, 1224.
- [55] D.-H. Kim, M.-R. Park, H.-J. Lee, G.-H. Lee, *Appl. Surf. Sci.* **2006**, *253*, 409.
- [56] H. Kim, J. S. Horwitz, G. P. Kushto, Z. H. Kafafi, D. B. Chrisey, *Appl. Phys. Lett.* **2001**, *79*, 284.
- [57] A. R. Schlatmann, D. W. Floet, A. Hilberer, F. Garten, P. J. M. Smulders, T. M. Klapwijk, G. Hadzioannou, *Appl. Phys. Lett.* **1996**, *69*, 1764.
- [58] P. Lippens, U. Muehlfeld, In *Handbook of Visual Display Technology*; Chen, J.; Cranton, W.; Fihn, M., Eds.; Springer Berlin Heidelberg, 2012; pp. 779–794.
- [59] J. Schneider, P. Rohner, D. Thureja, M. Schmid, P. Galliker, D. Poulikakos, *Adv. Funct. Mater.* **2016**, *26*, 833.
- [60] D. S. Hecht, A. M. Heintz, R. Lee, L. Hu, B. Moore, C. Cucksey, S. Risser, *Nanotechnology* **2011**, *22*, 075201.
- [61] S.-Y. Bae, I.-Y. Jeon, J. Yang, N. Park, H. S. Shin, S. Park, R. S. Ruoff, L. Dai, J.-B. Baek, *ACS Nano* **2011**, *5*, 4974.
- [62] Y.-J. Noh, S.-S. Kim, T.-W. Kim, S.-I. Na, *Sol. Energy Mater. Sol. Cells* **2014**, *120, Part A*, 226.
- [63] W. Gaynor, G. F. Burkhard, M. D. McGehee, P. Peumans, *Adv. Mater.* **2011**, *23*, 2905.
- [64] C.-H. Chung, T.-B. Song, B. Bob, R. Zhu, Y. Yang, *Nano Res.* **2012**, *5*, 805.
- [65] Z. Yu, Q. Zhang, L. Li, Q. Chen, X. Niu, J. Liu, Q. Pei, *Adv. Mater.* **2011**, *23*, 664.
- [66] Z. Yu, L. Li, Q. Zhang, W. Hu, Q. Pei, *Adv. Mater.* **2011**, *23*, 4453.
- [67] X.-Y. Zeng, Q.-K. Zhang, R.-M. Yu, C.-Z. Lu, *Adv. Mater.* **2010**, *22*, 4484.
- [68] T. C. Hauger, S. M. I. Al-Rafia, J. M. Buriak, *ACS Appl. Mater. Interfaces* **2013**, *5*, 12663.

- [69] C.-H. Liu, X. Yu, *Nanoscale Res. Lett.* **2011**, *6*, 75.
- [70] W. J. Scheideler, J. Smith, I. Deckman, S. Chung, A. C. Arias, V. Subramanian, *J. Mater. Chem. C* **2016**, *4*, 3248.
- [71] K. Ellmer, *Nat. Photonics* **2012**, *6*, 809.
- [72] N. Al-Dahoudi, M. A. Aegerter, *J. Sol-Gel Sci. Technol.* **2003**, *26*, 693.
- [73] M. S. Weaver, L. A. Michalski, K. Rajan, M. A. Rothman, J. A. Silvernail, J. J. Brown, P. E. Burrows, G. L. Graff, M. E. Gross, P. M. Martin, M. Hall, E. Mast, C. Bonham, W. Bennett, M. Zumhoff, *Appl. Phys. Lett.* **2002**, *81*, 2929.
- [74] Y. Hong, Z. He, N. S. Lennhoff, D. A. Banach, J. Kanicki, *J. Electron. Mater.* **2004**, *33*, 312.
- [75] S. Ye, *Adv. Mater.* **2014**, *26*.
- [76] H. Hosseinzadeh Khaligh, K. Liew, Y. Han, N. M. Abukhdeir, I. A. Goldthorpe, *Sol. Energy Mater. Sol. Cells* **2015**, *132*, 337.
- [77] H. H. Khaligh, I. A. Goldthorpe, *Nanoscale Res. Lett.* **2013**, *8*, 235.
- [78] J. L. Elechiguerra, L. Larios-Lopez, C. Liu, D. Garcia-Gutierrez, A. Camacho-Bragado, M. J. Yacaman, *Chem. Mater.* **2005**, *17*, 6042.
- [79] J. P. Franey, G. W. Kammlott, T. E. Graedel, *Corros. Sci.* **1985**, *25*, 133.
- [80] D. P. Langley, M. Lagrange, G. Giusti, C. Jiménez, Y. Bréchet, N. D. Nguyen, D. Bellet, *Nanoscale* **2014**, *6*, 13535.
- [81] E. C. Garnett, W. Cai, J. J. Cha, F. Mahmood, S. T. Connor, M. Greyson Christoforo, Y. Cui, M. D. McGehee, M. L. Brongersma, *Nat. Mater.* **2012**, *11*, 241.
- [82] S. Karim, M. E. Toimil-Molares, A. G. Balogh, W. Ensinger, T. W. Cornelius, E. U. Khan, R. Neumann, *Nanotechnology* **2006**, *17*, 5954.
- [83] P. Ramasamy, D.-M. Seo, S.-H. Kim, J. Kim, *J. Mater. Chem.* **2012**, *22*, 11651.

- [84] F. S. F. Morgenstern, D. Kabra, S. Massip, T. J. K. Brenner, P. E. Lyons, J. N. Coleman, R. H. Friend, *Appl. Phys. Lett.* **2011**, *99*, 183307.
- [85] B. Deng, P.-C. Hsu, G. Chen, B. N. Chandrashekhar, L. Liao, Z. Ayitimuda, J. Wu, Y. Guo, L. Lin, Y. Zhou, M. Aisijiang, Q. Xie, Y. Cui, Z. Liu, H. Peng, *Nano Lett.* **2015**, *15*, 4206.
- [86] X. Zhang, X. Yan, J. Chen, J. Zhao, *Carbon* **2014**, *69*, 437.
- [87] R. R. Nair, H. A. Wu, P. N. Jayaram, I. V. Grigorieva, A. K. Geim, *Science* **2012**, *335*, 442.
- [88] B.-T. Liu, H.-L. Kuo, *Carbon* **2013**, *63*, 390.
- [89] K. Naito, N. Yoshinaga, E. Tsutsumi, Y. Akasaka, *Synth. Met.* **2013**, *175*, 42.
- [90] R. Chen, S. R. Das, C. Jeong, M. R. Khan, D. B. Janes, M. A. Alam, *Adv. Funct. Mater.* **2013**, *23*, 5150.
- [91] Y. Ahn, Y. Jeong, Y. Lee, *ACS Appl. Mater. Interfaces* **2012**, *4*, 6410.
- [92] D. Lee, H. Lee, Y. Ahn, Y. Lee, *Carbon* **2015**, *81*, 439.
- [93] M. Jørgensen, J. E. Carlé, R. R. Søndergaard, M. Lauritzen, N. A. Dagnæs-Hansen, S. L. Byskov, T. R. Andersen, T. T. Larsen-Olsen, A. P. L. Böttiger, B. Andreasen, L. Fu, L. Zuo, Y. Liu, E. Bundgaard, X. Zhan, H. Chen, F. C. Krebs, *Sol. Energy Mater. Sol. Cells* **2013**, *119*, 84.
- [94] M. A. Green, K. Emery, Y. Hishikawa, W. Warta, E. D. Dunlop, *Prog. Photovolt. Res. Appl.* **2015**, *23*, 1.
- [95] Z. Yu, Q. Zhang, L. Li, Q. Chen, X. Niu, J. Liu, Q. Pei, *Adv. Mater.* **2011**, *23*, 664.
- [96] M. Niggemann, B. Zimmermann, J. Haschke, M. Glatthaar, A. Gombert, *Thin Solid Films* **2008**, *516*, 7181.
- [97] J. Yang, D. Vak, N. Clark, J. Subbiah, W. W. H. Wong, D. J. Jones, S. E. Watkins, G. Wilson, *Sol. Energy Mater. Sol. Cells* **2013**, *109*, 47.
- [98] P.-T. Tsai, K.-C. Yu, C.-J. Chang, S.-F. Horng, H.-F. Meng, *Org. Electron.* **2015**, *22*, 166.

- [99] D. C. Marcano, D. V. Kosynkin, J. M. Berlin, A. Sinitskii, Z. Sun, A. Slesarev, L. B. Alemany, W. Lu, J. M. Tour, *ACS Nano* **2010**, *4*, 4806.
- [100] L. Xu, M. . Pope, *Preperation*.
- [101] H.-J. Shin, K. K. Kim, A. Benayad, S.-M. Yoon, H. K. Park, I.-S. Jung, M. H. Jin, H.-K. Jeong, J. M. Kim, J.-Y. Choi, Y. H. Lee, *Adv. Funct. Mater.* **2009**, *19*, 1987.
- [102] H. Pron, C. Bissieux, *Quant. InfraRed Thermogr. J.* **2004**, *1*, 229.
- [103] M. Romano, C. Pradere, J. Toutain, C. Hany, J. C. Batsale, *Quant. InfraRed Thermogr. J.* **2014**, *11*, 134.
- [104] A. T. Bellew, H. G. Manning, C. Gomes da Rocha, M. S. Ferreira, J. J. Boland, *ACS Nano* **2015**, *9*, 11422.
- [105] A. Bid, A. Bora, A. K. Raychaudhuri, *Phys. Rev. B* **2006**, *74*, 035426.
- [106] Z. Cheng, L. Liu, S. Xu, M. Lu, X. Wang, *Sci. Rep.* **2015**, *5*, 10718.
- [107] A. T. Bellew, H. G. Manning, C. Gomes da Rocha, M. S. Ferreira, J. J. Boland, *ACS Nano* **2015**, *9*, 11422.
- [108] S.-B. Yang, H. Choi, D. S. Lee, C.-G. Choi, S.-Y. Choi, I.-D. Kim, *Small* **2015**, *11*, 1293.
- [109] X. Li, Y. Zhu, W. Cai, M. Borysiak, B. Han, D. Chen, R. D. Piner, L. Colombo, R. S. Ruoff, *Nano Lett.* **2009**, *9*, 4359.
- [110] G. Eda, G. Fanchini, M. Chhowalla, *Nat. Nanotechnol.* **2008**, *3*, 270.
- [111] J. S. Woo, J. T. Han, S. Jung, J. I. Jang, H. Y. Kim, H. J. Jeong, S. Y. Jeong, K.-J. Baeg, G.-W. Lee, *Sci. Rep.* **2014**, *4*, 4804.
- [112] S. Hong, H. Lee, J. Lee, J. Kwon, S. Han, Y. D. Suh, H. Cho, J. Shin, J. Yeo, S. H. Ko, *Adv. Mater.* **2015**, *27*, 4744.
- [113] P. Kumar, F. Shahzad, S. Yu, S. M. Hong, Y.-H. Kim, C. M. Koo, *Carbon* **2015**, *94*, 494.

- [114] I. T. Sachs-Quintana, T. Heumüller, W. R. Mateker, D. E. Orozco, R. Cheacharoen, S. Sweetnam, C. J. Brabec, M. D. McGehee, *Adv. Funct. Mater.* **2014**, *24*, 3978.
- [115] E. A. Katz, D. Faiman, S. M. Tuladhar, J. M. Kroon, M. M. Wienk, T. Fromherz, F. Padinger, C. J. Brabec, N. S. Sariciftci, *J. Appl. Phys.* **2001**, *90*, 5343.
- [116] K. J. Bergemann, R. Krasny, S. R. Forrest, *Org. Electron.* **2012**, *13*, 1565.
- [117] T. T. Thao, T. Q. Trung, V.-V. Truong, N. N. Dinh, T. T. Thao, T. Q. Trung, V.-V. Truong, N. N. Dinh, *J. Nanomater. J. Nanomater.* **2015**, *2015*, 2015, e463565.
- [118] G. Macrelli, *Sol. Energy Mater. Sol. Cells* **1995**, *39*, 123.
- [119] C. M. Lampert, *Sol. Energy Mater. Sol. Cells* **2003**, *76*, 489.
- [120] C. M. Lampert, *IEEE Circuits Devices Mag.* **1992**, *8*, 19.
- [121] Y. Liu, L. Sun, G. Sikha, J. Isidorsson, S. Lim, A. Anders, B. Leo Kwak, J. G. Gordon II, *Sol. Energy Mater. Sol. Cells* **2014**, *120, Part A*, 1.
- [122] J. M. Bell, J. P. Matthews, I. L. Skryabin, *Solid State Ion.* **2002**, *152–153*, 853.
- [123] Y.-M. Lu, C.-P. Hu, *J. Alloys Compd.* **2008**, *449*, 389.
- [124] B. P. Jelle, G. Hagen, *J. Appl. Electrochem.* **1999**, *29*, 1103.
- [125] P. S. Drzaic, *Liquid Crystal Dispersions*; World Scientific, 1995.
- [126] J. F. Elman, J. Greener, C. M. Herzinger, B. Johs, *Thin Solid Films* **1998**, *313–314*, 814.
- [127] J. Li, G. Baird, Y.-H. Lin, H. Ren, S.-T. Wu, *J. Soc. Inf. Disp.* **2005**, *13*, 1017.
- [128] J. Li, C.-H. Wen, S. Gauza, R. Lu, S.-T. Wu, *J. Disp. Technol.* **2005**, *1*, 51.
- [129] H. Kim, C. M. Gilmore, A. Piqué, J. S. Horwitz, H. MattoSSI, H. Murata, Z. H. Kafafi, D. B. Chrisey, *J. Appl. Phys.* **1999**, *86*, 6451.
- [130] M. Pathirane, **2016**.
- [131] M. Pathirane, H. H. Khaligh, I. A. Goldthorpe, W. s. Wong, *To be submitted*.

- [132] S. Alex, A. Tiwari, *J. Nanosci. Nanotechnol.* **2015**, *15*, 1869.
- [133] C. M. Cobley, S. E. Skrabalak, D. J. Campbell, Y. Xia, *Plasmonics* **2009**, *4*, 171.
- [134] B. Wiley, Y. Sun, Y. Xia, *Acc. Chem. Res.* **2007**, *40*, 1067.
- [135] S. Sarkar, S. Saha, S. Pal, P. Sarkar, *RSC Adv.* **2014**, *4*, 14673.
- [136] P. Balaya, *Energy Environ. Sci.* **2008**, *1*, 645.
- [137] Q. Jiang, C. C. Yang, *Curr. Nanosci.* **2008**, *4*, 179.
- [138] C. Q. Sun, *Prog. Solid State Chem.* **2007**, *35*, 1.
- [139] A. Verma, F. Stellacci, *Small* **2010**, *6*, 12.
- [140] P. C. Ray, *Chem. Rev.* **2010**, *110*, 5332.
- [141] A. Albanese, P. S. Tang, W. C. W. Chan, *Annu. Rev. Biomed. Eng.* **2012**, *14*, 1.
- [142] C. T. Campbell, S. C. Parker, D. E. Starr, *Science* **2002**, *298*, 811.
- [143] K. K. Nanda, A. Maisels, F. E. Kruis, H. Fissan, S. Stappert, *Phys. Rev. Lett.* **2003**, *91*, 106102.
- [144] P. Buffat, J.-P. Borel, *Phys. Rev. A* **1976**, *13*, 2287.
- [145] K. Koga, T. Ikeshoji, K. Sugawara, *Phys. Rev. Lett.* **2004**, *92*, 115507.
- [146] L. E. Brus, *J. Chem. Phys.* **1984**, *80*, 4403.
- [147] T. Omata, K. Nose, S. Otsuka-Yao-Matsuo, *J. Appl. Phys.* **2009**, *105*, 073106.
- [148] C. Cheng, B. Yan, S. M. Wong, X. Li, W. Zhou, T. Yu, Z. Shen, H. Yu, H. J. Fan, *ACS Appl. Mater. Interfaces* **2010**, *2*, 1824.
- [149] M.-S. Hu, H.-L. Chen, C.-H. Shen, L.-S. Hong, B.-R. Huang, K.-H. Chen, L.-C. Chen, *Nat. Mater.* **2006**, *5*, 102.
- [150] M. D. Shirsat, M. A. Bangar, M. A. Deshusses, N. V. Myung, A. Mulchandani, *Appl. Phys. Lett.* **2009**, *94*, 083502.
- [151] Y. Tak, H. Kim, D. Lee, K. Yong, *Chem. Commun.* **2008**, 4585.

- [152] C. Guan, J. Liu, C. Cheng, H. Li, X. Li, W. Zhou, H. Zhang, H. J. Fan, *Energy Environ. Sci.* **2011**, *4*, 4496.
- [153] J. Li, X. Lin, *Sens. Actuators B Chem.* **2007**, *126*, 527.
- [154] G. A. Sotiriou, A. M. Hirt, P.-Y. Lozach, A. Teleki, F. Krumeich, S. E. Pratsinis, *Chem. Mater.* **2011**, *23*, 1985.
- [155] J. Hafiz, R. Mukherjee, X. Wang, M. Cullinan, J. V. R. Heberlein, P. H. McMurry, S. L. Girshick, *J. Nanoparticle Res.* **2006**, *8*, 995.
- [156] K. Jiang, A. Eitan, L. S. Schadler, P. M. Ajayan, R. W. Siegel, N. Grobert, M. Mayne, M. Reyes-Reyes, H. Terrones, M. Terrones, *Nano Lett.* **2003**, *3*, 275.
- [157] P. H. C. Camargo, C. M. Cobley, M. Rycenga, Y. Xia, *Nanotechnology* **2009**, *20*, 434020.
- [158] Y. Bi, H. Hu, S. Ouyang, Z. Jiao, G. Lu, J. Ye, *J. Mater. Chem.* **2012**, *22*, 14847.
- [159] M.-L. Zhang, X. Fan, H.-W. Zhou, M.-W. Shao, J. A. Zapien, N.-B. Wong, S.-T. Lee, *J. Phys. Chem. C* **2010**, *114*, 1969.
- [160] D. Chen, S. H. Yoo, Q. Huang, G. Ali, S. O. Cho, *Chem. Weinh. Bergstr. Ger.* **2012**, *18*, 5192.
- [161] A. Tao, F. Kim, C. Hess, J. Goldberger, R. He, Y. Sun, Y. Xia, P. Yang, *Nano Lett.* **2003**, *3*, 1229.
- [162] C. Dong, Z. Yan, J. Kokx, D. B. Chrisey, C. Z. Dinu, *Appl. Surf. Sci.* **2012**, *258*, 9218.
- [163] D. Derkacs, W. V. Chen, P. M. Matheu, S. H. Lim, P. K. L. Yu, E. T. Yu, *Appl. Phys. Lett.* **2008**, *93*, 091107.
- [164] K. Islam, A. Alnuaimi, E. Battal, A. K. Okyay, A. Nayfeh, *Sol. Energy* **2014**, *103*, 263.
- [165] Y. Xiao, J. P. Yang, P. P. Cheng, J. J. Zhu, Z. Q. Xu, Y. H. Deng, S. T. Lee, Y. Q. Li, J. X. Tang, *Appl. Phys. Lett.* **2012**, *100*, 013308.
- [166] D. Schürch, A. Currao, S. Sarkar, G. Hodes, G. Calzaferri, *J. Phys. Chem. B* **2002**, *106*, 12764.

- [167] S. Wu, X. Shen, Z. Ji, G. Zhu, C. Chen, K. Chen, R. Bu, L. Yang, *CrystEngComm* **2015**, *17*, 2517.
- [168] C. An, S. Peng, Y. Sun, *Adv. Mater.* **2010**, *22*, 2570.
- [169] P. Wang, B. Huang, X. Qin, X. Zhang, Y. Dai, J. Wei, M.-H. Whangbo, *Angew. Chem. Int. Ed.* **2008**, *47*, 7931.
- [170] S. Coskun, E. S. Ates, H. E. Unalan, *Nanotechnology* **2013**, *24*, 125202.
- [171] D. P. Langley, G. Giusti, M. Lagrange, R. Collins, C. Jiménez, Y. Bréchet, D. Bellet, *Sol. Energy Mater. Sol. Cells* **2014**, *125*, 318.
- [172] B. Wiley, Y. Sun, B. Mayers, Y. Xia, *Chem. – Eur. J.* **2005**, *11*, 454.
- [173] Z. Yan, G. Compagnini, D. B. Chrisey, *J. Phys. Chem. C* **2010**, *115*, 5058.
- [174] M. Zhu, P. Chen, W. Ma, B. Lei, M. Liu, *ACS Appl. Mater. Interfaces* **2012**, *4*, 6386.
- [175] Y. Cao, W. Liu, J. Sun, Y. Han, J. Zhang, S. Liu, H. Sun, J. Guo, *Nanotechnology* **2006**, *17*, 2378.
- [176] S. H. Im, Y. T. Lee, B. Wiley, Y. Xia, *Angew. Chem.* **2005**, *117*, 2192.
- [177] X. Tang, M. Tsuji, In *Nanowires Science and Technology*; Lupu, N., Ed.; InTech, 2010.
- [178] S. Liu, B. Weng, Z.-R. Tang, Y.-J. Xu, *Nanoscale* **2014**, *7*, 861.
- [179] S.-W. Kim, H.-E. Chung, J.-H. Kwon, H.-G. Yoon, W. Kim, *Bull. Korean Chem. Soc.* **2010**, *31*, 2918.
- [180] Y. Sun, Y. Yin, B. T. Mayers, T. Herricks, Y. Xia, *Chem. Mater.* **2002**, *14*, 4736.
- [181] L. Zhang, X. Fang, C. Ye, *Controlled Growth of Nanomaterials*; World Scientific, 2007.
- [182] S. Nam, M. Song, D.-H. Kim, B. Cho, H. M. Lee, J.-D. Kwon, S.-G. Park, K.-S. Nam, Y. Jeong, S.-H. Kwon, Y. C. Park, S.-H. Jin, J.-W. Kang, S. Jo, C. S. Kim, *Sci. Rep.* **2014**, *4*.